Optimized ion trapping of exotic nuclides for massmeasurements in the N=40 (magic?) region

C. Guénaut

UNIVERSITÉ PARIS-SUD 11

CSNSM

N° d'ordre: 8058

THÈSE
présentée pour obtenir le grade de
DOCTEUR EN SCIENCES DE L'UNIVERSITÉ PARIS XI, ORSAY

par
Céline GUÉNAUT

Optimized ion trapping of exotic nuclides for mass measurements in the *N*=40 (magic?) region

Soutenue le **10 novembre 2005** devant le jury composé de MM.

Laurent TASSAN-GOT	Président
Bertram BLANK	Rapporteur
Nathal SEVERIJNS	Rapporteur
Sophie PERU-DESENFANTS	
Fanny REJMUND	
David LUNNEY	Directeur de thèse

UNIVERSITÉ PARIS-SUD 11

CSNSM

N° d'ordre: 8058

THÈSE
présentée pour obtenir le grade de
DOCTEUR EN SCIENCES DE L'UNIVERSITÉ PARIS XI, ORSAY

par
Céline GUÉNAUT

Un piégeage d'ions optimal pour la mesure de masse de noyaux exotiques dans la région (magique ?) de N=40

Soutenue le **10 novembre 2005** devant le jury composé de MM.

Laurent TASSAN-GOT	Président
Bertram BLANK	Rapporteur
Nathal SEVERIJNS	Rapporteur
Sophie PERU-DESENFANTS	
Fanny REJMUND	
David LUNNEY	Directeur de thèse

Remerciements

Les remerciements sont une partie essentielle d'une thèse, non pas parce que certaines personnes ne lisent que ça mais bien parce qu'une thèse ne se fait pas tout seul. Je tiens donc à remercier sincèrement tous ceux qui ont contribué à rendre ces trois années de thèse fructueuses et vivables. Je m'excuse par avance auprès de tous ceux que je vais forcément oublier dans ces lignes mais qui restent présents dans mon esprit.

Je tiens tout d'abord à remercier le directeur du CSNSM, Hubert Flocard, pour m'avoir accueillie au sein de son laboratoire.

Mes pensées se dirigent ensuite naturellement vers mon directeur de thèse Dave qui m'a "supportée" pendant trois ans. Nos discussions parfois animées ont toujours été très riches. Je le remercie de m'avoir fait collaboré à l'expérience ISOLTRAP. J'espère que nos futures collaborations seront toutes aussi fructueuses.

Je voudrais remercier tous les membres de mon jury de thèse pour avoir accepté l'invitation. Tout particulièrement Laurent Tasssan-Got le président qui a bien voulu se laisser " piéger " par un domaine de recherche qui lui était inconnu. Je remercie vivement mes deux rapporteurs Bertram Blank et Nathal Severinjs pour leur rapidité à lire le manuscrit et la richesse de leurs conseils le concernant. Je tiens également à remercier les deux membres féminins de mon jury : Sophie Peru qui a représenté le coté théorique de cette thèse dans le jury, et Fanny Rejmund, qui, faisant partie de " mon ancienne recherche ", a su faire le lien avec la nouvelle.

Je tiens également à remercier Catherine, notre chef de groupe, toujours présente pour répondre à mes questions diverses et variées. Michel, qui malgré le peu de temps que nous nous sommes côtoyés m'a expliqué les fondements de MISTRAL, Georges pour sa rigueur et ses indispensables explications de la table de masse, Carole pour ses nombreux conseils, Michael pour son soucis de la propreté. Et bien sûr Jean-François, qui a été d'une aide inestimable, ainsi que Geneviève qui a su rendre mon séjour au CERN des plus agréables.

Je voudrais remercier tout particulièrement Jean Libert pour sa patience et sa compréhension, ainsi que pour ses explications théoriques et les nombreux résultats de calculs qu'il a fait pour moi.

I would like to thank all the people from the ISOLTRAP collaboration for the precious work we have done together. Especially Jurgen Kluge who trusted me when he decided to let me analyzed so many data. I have also special thoughts for Klaus Blaum who had confidence in me and let me work alone on the experiment without any doubts, and for his kindness and his friendship.

Je remercie également tous ceux du laboratoire qui ne m'ont pas pris pour une "blonde" et m'ont expliqué divers aspects techniques comme l'utilisation de la perceuse, de la scie électrique,...: Claire, Dominique, Georges, André, Laurent, Tony.

Je remercie tous les autres du laboratoire avec qui j'ai pu déjeuner, prendre un café, faire une réunion de doctorants (avec ou sans pelle) ou tout simplement qui était là pour me dire un petit mot d'encouragement : Claire, Benjamin, Caroline Aurélien, Jérome, Jérome, Sophie, François, Eric, Annie, Claudine, Serge.

Et enfin merci à Helène, Sylvain, Cathy, Gypaos, Pascal, Nico, et surtout Cyril pour leur bonne humeur et leur " précieux enseignements "...

Un grand merci à mes parents qui ont su comprendre mes variations d'humeurs...

Contents

Avant propos

Depuis toujours les nombres magiques fascinent, que ce soit du point de vue théorique ou expérimental. Ne serait-ce que leur nom " magique ", cela dénote une propriété peu commune qui ne peut qu'attirer l'attention. Ces nombres magiques, tout d'abord découverts expérimentalement, furent ensuite expliqués théoriquement. Mais depuis quelques années, d'autres noyaux apparaissent magiques alors qu'ils ne possèdent pas les fameux " nombres magiques ". Et d'autres encore qui auraient dû l'être s'avèrent ne pas être magiques. Tous ces phénomènes rajoutent de la magie à cette propriété des noyaux, mais n'aident pas à leur prédiction.

Ces nombres sont déclarés magiques car ils représentent des fermetures de couche particulièrement stables, cette particularité les place à la base de la structure nucléaire. Une mise en évidence de leur présence est l'étude de leur énergie de liaison et plus particulièrement l'énergie de séparation de deux neutrons, c'est à dire la quantité d'énergie qu'il faut fournir au système pour lui enlever deux neutrons. Par exemple, quand un noyau est magique en neutrons, tous ses neutrons sont très liés, il est difficile de lui en enlever. Au contraire si deux neutrons lui sont ajoutés, ils seront moins liés et donc plus facile à enlever. Des connaissances très précises sur les énergies de liaison sont nécessaires afin de pouvoir détecter des variations de très faible magnitude. On définit une énergie de liaison comme la différence entre la masse d'un noyau et la somme des masses de ses constituants. Par conséquent une mesure de masse très précise permet d'avoir des informations très précises sur les énergies de liaisons.

Ces mesures de masse de haute précision qui sont nécessaires pour étudier la " magicité " le sont plus particulièrement sur les noyaux exotiques, car ce sont ces noyaux qui présentent des écarts à la "magicité classique". Ces noyaux sont des noyaux éloignés de la vallée de stabilité, donc par définition instables et de courtes durées de vie. Le développement des connaissances sur les noyaux exotiques nécessite donc des mesures de masse de haute précision et sur des noyaux de courtes durées de vie.

Parmi les systèmes de mesure de masse de haute précision, il existe deux spectromètres complémentaires MISTRAL et ISOLTRAP, tous les deux situés au CERN à ISOLDE. MISTRAL est un spectromètre de masse en transmission capable de mesurer des noyaux de courte durée de vie. ISOLTRAP est un spectromètre basé sur l'utilisation de pièges, ce qui est, de nos jours, la méthode de mesure de masse la plus précise, mais l'utilisation de pièges empêche la mesure de noyaux de très courtes durées de vie.

Ces deux spectromètres sont complémentaires, mais présentent tous les deux des lim-

ites. La transmission de MISTRAL est très faible : son acceptance est très faible par rapport à l'émittance du faisceau d'ISOLDE. Quant à ISOLTRAP, les champs magnétique et électrique doivent être les plus parfaits possible, afin d'effectuer un contrôle très précis du mouvement des ions. Ceci est nécessaire pour assurer des mesures de très haute précision.

Afin de réduire les limites de ces deux spectromètres j'ai, pendant ma thèse, contribué à l'élaboration d'un système de refroidissement de faisceau COLETTE pour MISTRAL afin de diminuer l'émittance du faisceau d'ISOLDE et de l'adapter à l'acceptance de MISTRAL. J'ai également travaillé sur une procédure d'optimisation des champs électriques et magnétiques présents dans le piège de mesure d'ISOLTRAP. Cette optimisation permet un contrôle très fin des trajectoires des ions et donc une mesure très précise.

La table de masse AME (Atomic-Mass Evaluation table) est basée sur l'évaluation de toutes les mesures de masse. Dans cette table, les noyaux sont liés entre eux de par la définition même de l'unité de masse : $\frac{1}{12}m(^{12}\mathrm{C})$. Par ailleurs, on peut distinguer une trame centrale de noyaux très connus autour de laquelle s'articule la table (appelée " backbone "). Ce backbone aide à la connaissance de tous les autres noyaux grâce aux liens qui existent entre eux.

Des mesures de haute précision ont été effectuées avec ISOLTRAP. Tout d'abord pour élargir le nombre de noyaux connus avec une grande précision contenus dans le " backbone ". D'autre part des mesures sur le chrome ont été effectuées afin d'amener des éléments de réponse à la question de magicité de $N = 32$. Par ailleurs, des mesures sur le nickel, le cuivre et le gallium ont été entreprises pour tenter de répondre à une question qui passionne la communauté scientifique depuis de nombreuses années : " $N = 40$ est-il un nombre magique ? ".

Part I

Mass measurements: Why and How?

Chapter 1

Mass measurements

Mass measurements on exotic nuclides are performed for various reasons which are explained hereafter. To this purpose exotic nuclides need to be produced, and different methods of measurements and tools exist.

1.1 Introduction to mass measurements of exotic nuclides

Since the discovery by Aston in 1920 [1] that the mass of a nuclide is not exactly the mass of all its components, the interest in mass measurements has never ceased. This mass "defect" (as Aston called it) leads to the definition of the nuclear-binding energy B which is the difference between the mass $M(N,Z)$ of a nucleus with N neutrons and Z protons and the sum of the masses of its constituents:

$$B(N,Z) = \big(NM_n + ZM_p - M(N,Z)\big)c^2, \tag{1.1}$$

with M_n and M_p the mass of one neutron and one proton. The Einstein relation $E = mc^2$ demonstrates the importance of the mass value. It is a fundamental property of a nuclide used in different fields: atomic physics, nuclear structure, astrophysics, and for the study of the weak interaction [2].

The nuclear binding energy is based on the use of the nuclear mass, which should not be confused with the atomic mass. The corresponding relation is:

$$M_{at}(N,Z) = M_{nuc}(N,Z) + ZM_e - B_{el}(Z), \tag{1.2}$$

with M_{at} the atomic mass, M_{nuc} the nuclear mass, M_e the mass of the electron, and B_{el} the binding energy of the electrons. An approximation of B_{el} can be found in [2]. Its value may be small for light nuclides like hydrogen for which $B_{el} = 13.6\,\text{eV}$, while for heavy nuclides its value is higher: 115 keV for uranium ($Z = 92$). Most mass measurements are performed on singly-charged ions, so to calculate the atomic mass one has to take into account the mass and the binding energy of only one missing electron.

Since it reflects the net interaction of all forces interacting in the nucleus, the binding energy reveals information about nuclear structure. Derivatives can also be used to examine this structure more closely. For instance the two-neutron separation energy S_{2n} which is the energy required to remove two neutrons, or the two-proton separation energy S_{2p},

the one neutron S_n and one proton S_p separation energy:

$$S_{2n} = B(Z,N) - B(Z,N-2), \qquad S_{2p} = B(Z,N) - B(Z-2,N)$$
$$S_n = B(Z,N) - B(Z,N-1), \qquad S_p = B(Z,N) - B(Z-1,N).$$

An example is shown in figure 1.1. The two-neutron separation energy is decreasing with increasing number of neutrons in the nucleus: the larger the number of neutrons, the smaller the interaction between the nucleons and the new neutrons. A linear trend is expected, a deviation from this linear trend brings indications on nuclear structure. For $N = 50$ there is a break in the linear trend, which indicates a shell closure: it is easier to remove two neutrons added just after a shell closure since they are less bound. This figure also shows strong deformation in the nuclear structure around $N = 60$.

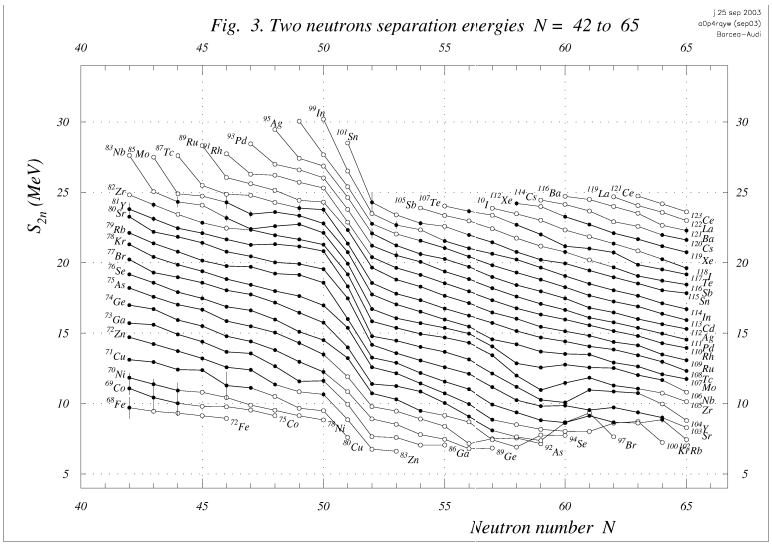

Figure 1.1: *Two-neutron separation energies (S_{2n}) for N=42 to 65 [3]. The shell closure at $N = 50$ is clearly shown.*

The major discontinuities in the nuclear binding energies occur for nucleon numbers 2, 8, 20, 28, 50, 82, and 126. These numbers are the counterpart in nuclear structure to the atomic numbers (Z = 2, 10, 18, 36, 54, and 86) [4] that form the periodic table. As in the atomic case, these numbers correspond to the closing of shells that have an especially large energy separation from the next higher orbital (major shell closings)[1]. These closed-shell numbers are called "magic" numbers. Nowadays, as experiments are going further from stability, these magic numbers are changing [6]: Magic Z and N numbers depend on N and Z, respectively. Shell gaps seem to shrink or disappear[7], and new ones appear

[1]The behaviour can be explained since, going from atom Z to $Z+1$, the charge of the nucleus increases. The ionization energy will thus increase on the average and in a rather smooth way when filling the electron shells. When starting to fill a new electron shell, the last electron occurs in a *less* strongly bound orbit but a screening effect of the central, nuclear charge by a number of filled electron orbits presents an effectively smaller Coulomb potential. So the electron ionization energy reflects strong variations whenever an electron shell is closed [5].

when leaving the valley of stability. Discussion of such disappearance and reappearance is presented in Chapters 7 and 8.

Shown in figure 1.2 is the nuclear chart of known nuclides. The driplines define the limits beyond which nuclides are not bound. The neutron drip line is defined in terms of the minimum value of N for which $S_n < 0$ at each value of Z: $S_n < 0$ means that the last neutron is unbound. The proton drip line, defined in the same way, corresponds to the minimum value of Z for which $S_p < 0$ at each value of N. While most of the proton dripline has been reached by experiments, figure 1.2 shows that this is as yet far from being the case for the neutron dripline.

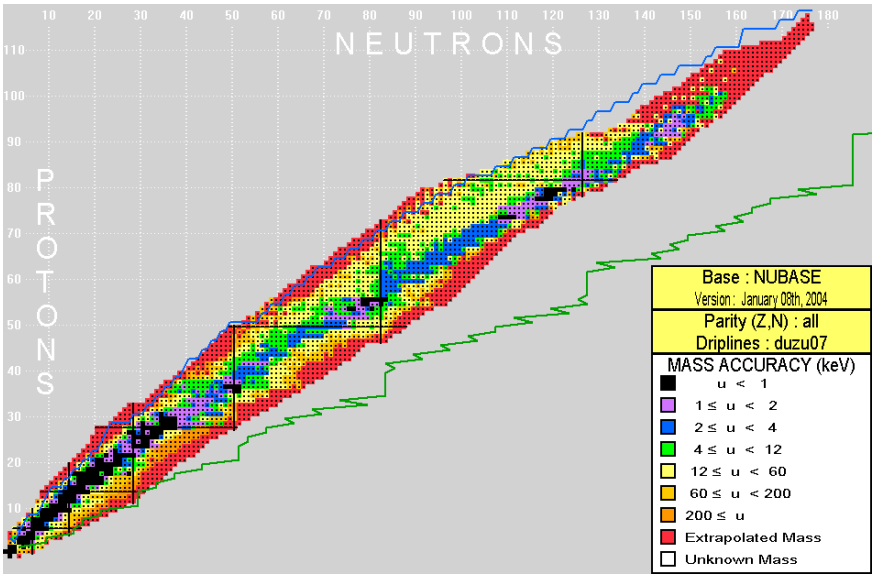

Figure 1.2: *The nuclear chart: number of protons versus number of neutrons, the range of mass accuracy u is indicated [8]. Only the mass of a few number of nucleons is well known. Theoretical driplines from Duflo-Zuker [9] are shown.*

This lack of knowledge shown on this nuclear chart must be solved by mass model predictions. In the nuclear chart, around 3000 nuclides are known, but between 5000 and 8000 are predicted by mass models. For known nuclides, models are in good agreement since most of them are fitted to the known masses. For the unknown ones (see figure 1.3) there is no agreement. Mass measurements far from stability are therefore crucial for better constraining available models. This point is discussed in more details in Chapter 8.

To study more closely the nuclear structure, very accurate measurements are usually needed. Depending on the field of study the required precision is not the same, here is a brief review of the needed accuracy $\delta m/m$ (see [2]):

- In nuclear physics there is still a lot of information to discover especially on binding energies to get shell information: $10^{-5} - 10^{-6}$,
- To constrain nuclear models: $10^{-6} - 10^{-7}$,
- To finely study the nuclear structure from energy differences for nuclear pairing, deformation and shape coexistence: $< 1 \cdot 10^{-7}$,

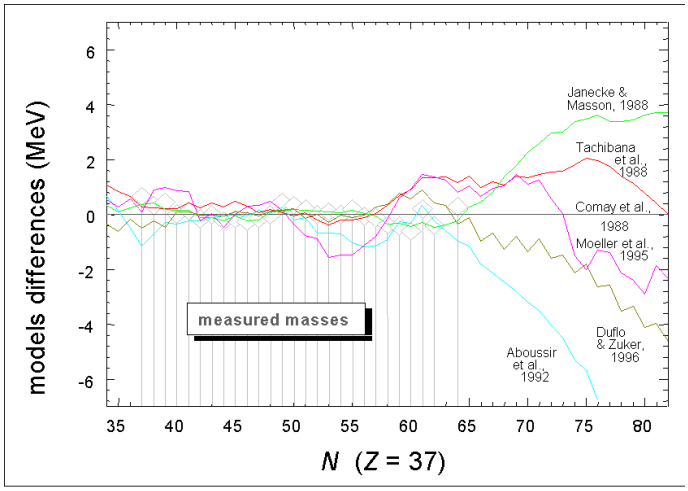

Figure 1.3: *Differences between mass models around $Z = 37$ [2]: far from stability there is no agreement between models.*

- To study the weak interaction by testing symmetries, the CVC (Conserved-Vector-Current) hypothesis,... 10^{-8}.

Hence progress must be made on two fronts: accuracy to uncover nuclear effects and sensitivity to go further from stability to uncover new effects.

1.2 Techniques of production

To measure masses far from stability the nuclides must first be produced. A variety of techniques are used which can roughly be grouped into two categories, which are schematized in figure 1.4.

Heavy ion beam fragmentation and in-flight separation

Fragmentation is based on nuclear reactions induced by the fragmentation of a heavy ion beam by a thin target. It is used for example at GANIL, at GSI, and at RIKEN. The interest of this method is that the fragments have the same energy as the incoming beam ($\sim 50 - 100$MeV/A), and are directly extracted so one gets access to very short-lived nuclides. The problem with this method is the poor optical quality of the beam: there is a large angular and energy dispersion.

ISOL technique

The ISOL (Isotope Separator On Line) technique is based on the reactions (*e.g.* spallation, fission, fragmentation) induced by an ion beam hitting a thick target. Reaction products are created in the target, extracted by thermal diffusion, and are then ionized by different techniques: surface ionization, plasma, resonant laser ionization (RILIS). Afterwards they are accelerated to modest transport energy (*e.g.* 60 keV) and finally mass separated via

an electromagnetic separator. The problem with this kind of production technique is the time-consuming thermal diffusion from the target which is a handicap to produce very short-lived nuclides. On the other hand, this method produces a beam with superior beam optical properties.

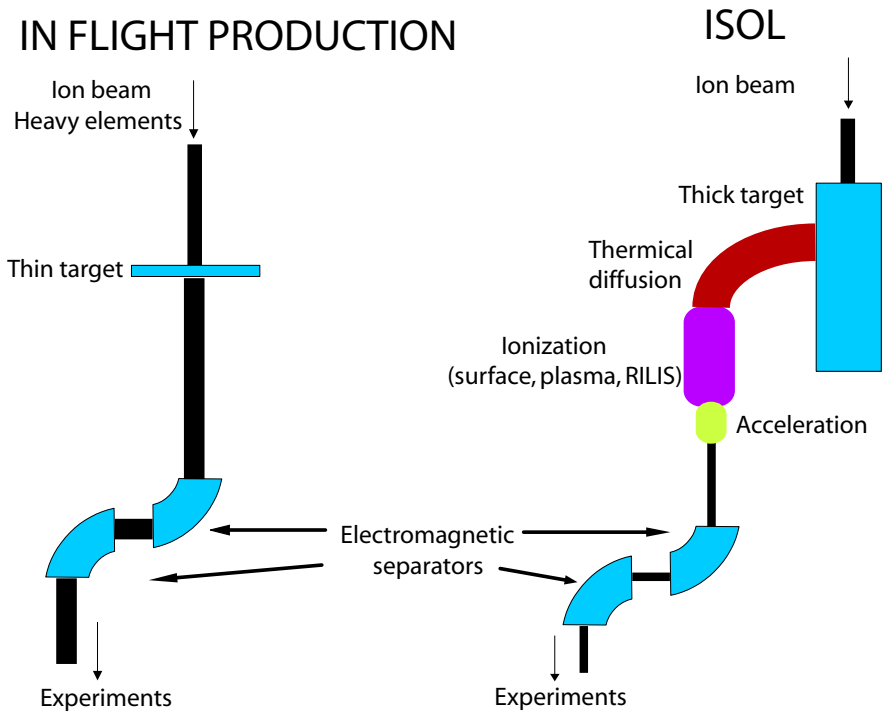

Figure 1.4: *The two principal methods for production of radioactive nuclides: in-flight method and ISOL technique. They mainly differ by the target thickness.*

The pioneering facility using the ISOL technique is the on-line isotope separator ISOLDE [10] facility located at CERN (Geneva/Switzerland). Proton pulses are accelerated by a linac and by the Proton-Synchrotron Booster (PSB), and are sent onto the ISOLDE target with an energy of 1 or 1.4 GeV and an intensity of about 2μA. ISOLDE produces a large variety of radioactive nuclei of more than 60 different elements. They are extracted from the ion source, accelerated to 60 keV and sent to one of the two mass separators: the general purpose separator (GPS) delivers a beam with limited mass resolving power (≤ 1000) while the high resolution separator (HRS) may be used with a mass-resolving power of about $2500 - 5000$. The ion beam is then delivered to the various experiments located in the experimental hall as indicated in figure 1.5, including MISTRAL and ISOLTRAP which are described in the following chapters.

1.3 Mass measurement techniques

Two kinds of mass measurement techniques are distinguished: direct and indirect to refer to inertial or energy measurements.

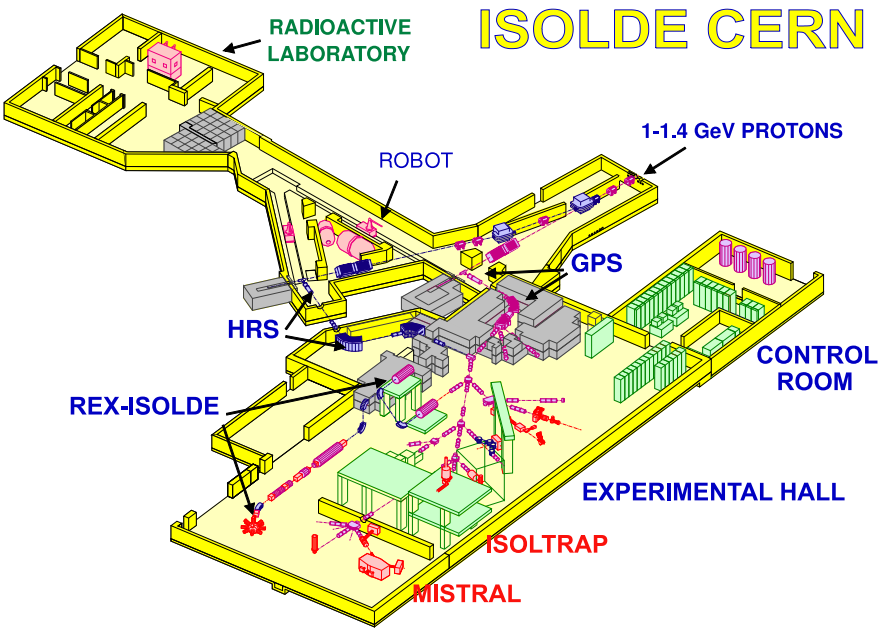

Figure 1.5: *Experimental hall of the ISOLDE facility [10].*

1.3.1 "Indirect", or energy measurements

"Indirect" mass measurements are performed by an energy measurement. During a nuclear reaction A(a,b)B, the conservation of the total energy gives a relation between all the masses involved in the reaction. From the energy Q of the reaction:

$$Q = M_A + M_a - M_b - M_B, \tag{1.3}$$

we can determine the mass of one of the reaction components if the three others are known.

Another kind of indirect measurement is from studies of spectroscopic decays of nuclides. From a decay $B \rightarrow A + b$, the mass of the parent nuclide B may be "measured" if the energy of the decay products b and the mass of the daughter nuclide A are known. This is a good method to measure very short lived nuclides, but the decay scheme should be very well known. Sometimes the unknown mass is far away from the known mass, in which case a mass determination based on only a limited number of decays can lead to a wrong value.

1.3.2 "Direct", or inertial measurements

Time and frequency measurements can be easily performed on reference ions of well-known mass yielding a more direct measurement of the mass.

Time-of-flight measurement

The time-of-flight measurement is based on the measurement of the time ions need to travel a defined distance. This is typically used for nuclides produced by fragmentation and also requires a measurement of rigidity. This method was used by TOFI (Time Of Flight Isochronous) in Los Alamos [11]. They mainly performed measurements from $Z = 20$ to $Z = 32$.

SPEG (Spectromètre à Perte d'EnerGie) at GANIL is also using this technique. It is well suited to measure masses of nuclides far from stability, with a final precision of 10^{-5} [12] and a mass resolution of $3-8\cdot10^{-4}$ [13], limited by the length of the flight path. A new method of measurement using cyclotrons was developed to increase the length of the ions flight path. This is used by S.A.R.A [14] in Grenoble and CSS2 [15] at GANIL. With this method the precision achieved is $10^{-5}-10^{-6}$. In particular this allowed the measurement of the mass of the doubly magic $N = Z$ nuclide ^{100}Sn [16].

Another facility using this time-of-flight method is the ESR (Experimental Storage Ring) at GSI. It is based on the multiple measurement of the time of flight in storage rings. Two different kinds of techniques are used: the ESR-SMS (Schottky Mass Spectrometry) [17] and the ESR-IMS(Isochronous Mass Spectrometry) [18]. In the ESR-SMS the velocity dispersion is reduced by an electron cooler, and a Schottky probe detects ions and measures their revolution frequency. The achieved precision is few 10^{-7}, but the cooling needs around ten seconds, which limits measurement to ions with half-lives higher than this time. With the second technique: ESR-IMS, rings are tuned for isochronous trajectories, so the rotation frequency is not dependent on the ion velocity. Consequently, the electron cooling is not needed and a transmission detection system is used instead of the Schottky probe. The achieved precision is lower: around 10^{-6}, but it can measure ions with half-lives of 1 μs [18].

Cyclotron frequency measurement

A charged particle in a magnetic field $\overrightarrow{B}$ is under a conservative force: the Lorentz force,

$$\overrightarrow{F}_L = q\,\overrightarrow{v} \wedge \overrightarrow{B}, \tag{1.4}$$

with q the charge of the particle and $\overrightarrow{v}$ its velocity. The trajectory is a circle with a radius of curvature r corresponding to the equilibrium of all the forces, *i.e.* the Lorentz force and the centrifugal force $F_{cent} = mv^2/r$, with m the mass of the particle, and v the component of the velocity perpendicular to the magnetic field $\overrightarrow{B}$. This leads to:

$$qB = \frac{mv}{r}, \text{ with } \frac{v}{r} = \omega \text{ the angular velocity, so } \omega = \frac{qB}{m}. \tag{1.5}$$

With $\omega = 2\pi f$, we can define the cyclotron frequency:

$$f_c = \frac{qB}{2\pi m}. \tag{1.6}$$

With a known magnetic field, the mass is thus directly related to the cyclotron frequency. Several experiments are based on this frequency measurement, for instance the mass spectrometer MISTRAL, (explained in Chapter 3), and experiments using Penning

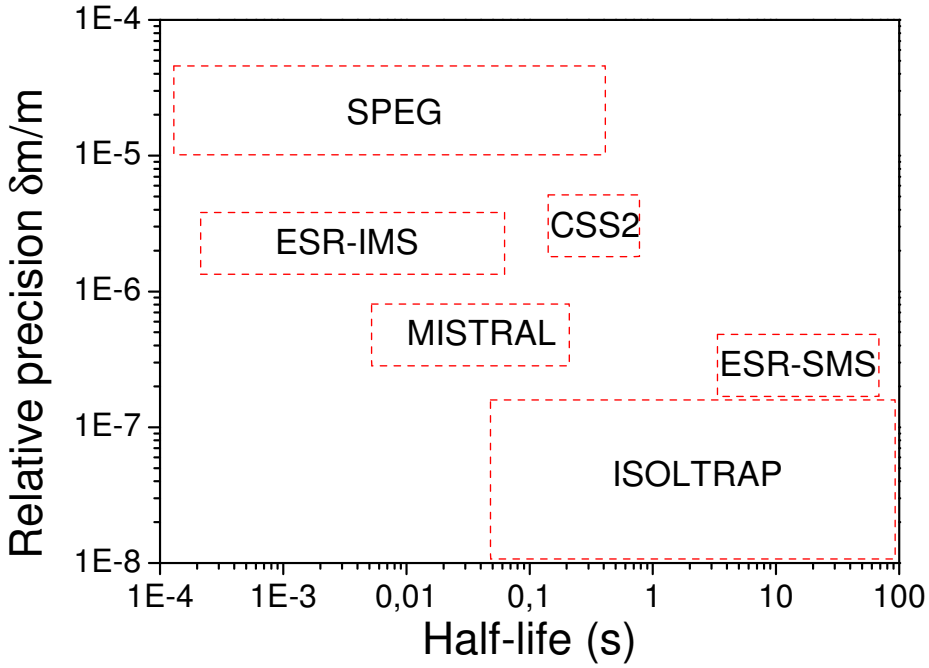

Figure 1.6: *Comparison between the different techniques for mass measurements: the relative mass precision as a function of the half-life [28]. The most precise experiment is ISOLTRAP.*

traps (see Chapter 2). Nowadays, Penning trap experiments are performing the most accurate mass measurements and going further and further away from stability. ISOLTRAP (see Chapter 3) has pioneered the use of the Penning traps for radioactive nuclides and has been followed by other Penning traps which are in operation: SMILETRAP using stable, highly-charged ions [19], the Canadian Penning Trap [20], JYFLTRAP [21], SHIPTRAP [22], LEBIT [23], and WITCH [24]. New online traps are planned for the near future like MLLTRAP at Munich [25], or TITAN [26] at TRIUMF/Vancouver [27].

1.3.3 Comparison of mass measurement techniques

All mass measurement techniques are based on different methods. Each method allows to probe a specific part of the nuclear chart with a specific precision. It is hard to get a compromise between the accuracy of the measurement and the reachable "exoticity". This is shown in figure 1.6, which presents the relative mass accuracy achieved as a function of the half-life. It shows the good complementarity of all methods. Traps provide at present the most precise and accurate method of measurement. However, according to the uncertainty principle of Heisenberg, $\Delta\nu \cdot \Delta t \geq 1$, reaching high accuracy needs time. By trapping ions, the time of measurement is increased. But this immediately confronts us with the present limit of traps: they cannot measure very short-lived nuclides.

Chapter 2

Ion manipulation

Accuracy requires observing ions during a long period for which traps are the best tools. But to trap ions and the reference isotopes under the same conditions they should be prepared. For this purpose, ion beam cooling is used. So pre-cooling is needed for trapping. It means that cooling and trapping are inherently related and cannot practically be achieved individually.

2.1 How to trap ions?

There are different kinds of traps and the most common ones use electric and/or magnetic fields. Among traps based on the use of electric fields are the Kingdon trap and the Paul trap, which are described in the following sections. The Kingdon trap [29] consists of a cylindrical electrode with a metallic wire in the center on the beam propagation axis and with a potential difference applied between them. An ion will be attracted by the wire and orbit around it. It is easy to prepare this kind of trap but the trajectory of ions is uncontrollable and trapping ions at rest is impossible.

Traps based on magnetic field are mainly the magnetic bottle and the Penning trap. As the Paul trap, the Penning trap is described in detail in the following. The magnetic bottle is based on the principle of "magnetic mirrors" [30]. Like for the Kingdon trap, only particles with a non-zero velocity can enter this trap and the ion trajectory is hard to control.

In the next sections we will describe how ions are trapped in Paul and Penning traps. In the following, the direction of propagation of ions is always along the z-axis. Paul and Penning traps are based on the use of quadrupole electric fields, with potentials of the form:

$$V(x,y,z) = \alpha(ax^2 + by^2 + cz^2). \tag{2.1}$$

This potential obeys the Laplace equation:

$$\Delta V(x,y,z) = \frac{\partial^2 V}{\partial x^2} + \frac{\partial^2 V}{\partial y^2} + \frac{\partial^2 V}{\partial z^2} = 0, \tag{2.2}$$

which leads to the condition $a+b+c=0$.
For a two-dimensional confinement one uses $c=0$ and $a=-b$ and the general potential

is

$$V_{2D}(x,y) = \beta(x^2 - y^2). \tag{2.3}$$

For three-dimensional trapping $c = -a - b$, and $a = b$ in order to ensure a symmetry in the radial direction. This leads to the condition $c = -2a$, so the general equation is

$$V_{3D}(x,y,z) = \beta(x^2 + y^2 - 2z^2). \tag{2.4}$$

Solving the equations for the ion movement in such a trap demonstrated [31] that it is impossible to trap in all directions at the same time only with this electrostatic field. Two solutions are used to counteract this problem. The first is to use an oscillating electric field to alternately trap in all directions: the Paul trap. The second solution is to use a magnetic field to trap ions in the radial direction: the Penning trap. In 2D trapping, this is more simple to understand. Figure 2.1 shows the potential created in the trap: if ions are trapped into the x-direction, they are not trapped into the y-direction, so by applying an oscillating field at the correct frequency we can trap ions in both directions.

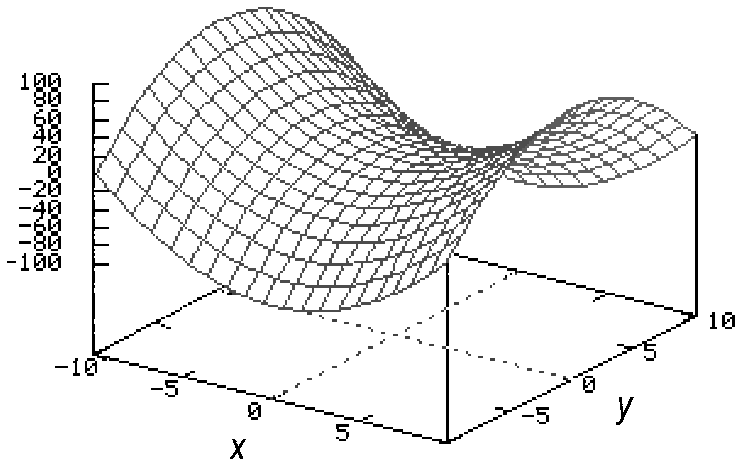

Figure 2.1: *Saddle shape like potential created by a two-dimensional quadrupole field* $V_{2D}(x,y) = \beta(x^2 - y^2)$. *Here, ions are trapped in the x-direction but not in the y-direction.*

2.2 The Paul trap

Here is presented the most used electric trap: the Paul trap.

To produce such a three-dimensional potential in a Paul trap, a two-dimensional cylindrical symmetry is used. For practical use, a hyperbolic electrode called in general "ring" with r_0 as minimal radius (in the middle of the trap), and two "endcaps" with distance $2z_0$ are used. To correct for the non-infinity of the electrodes [31], the dimensional constraint $r_0^2 = 2z_0^2$ is used . This geometry is presented in figure 2.2.

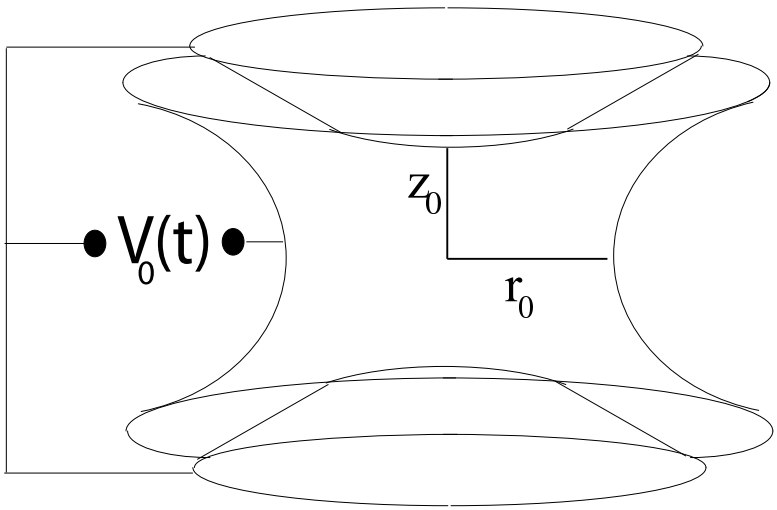

Figure 2.2: *Schematic drawing of a Paul trap.*

From eq. (2.4) the central electrode is a hyperboloid with equation $\frac{x^2}{A^2}+\frac{y^2}{B^2}-\frac{z^2}{C^2}=1$, where $A=B=r_0$ and $C=z_0$ so the geometrical condition is:

$$\frac{r^2}{r_0^2}-\frac{z^2}{z_0^2}=1. \tag{2.5}$$

The two endcaps are also hyperboloids following the equation $\frac{x^2}{A^2}+\frac{y^2}{B^2}-\frac{z^2}{C^2}=-1$, so the geometrical condition is

$$\frac{r^2}{r_0^2}-\frac{z^2}{z_0^2}=-1. \tag{2.6}$$

The general formula for this potential in a Paul trap becomes

$$V_{3D}(x,y,z,t)=\alpha V_0(t)(r^2-2z^2), \tag{2.7}$$

with $V_0(t)$ the potential applied between the electrodes. To determine α we use the continuity condition on the electrodes. The potential applied on the electrodes is $\frac{V_0(t)}{2}$. In $r=r_0$ the condition is $\frac{r^2}{r_0^2}-\frac{z^2}{z_0^2}=1$, so $r^2=r_0^2\big(1+\frac{z^2}{z_0^2}\big)$, and one obtains

$$V_{3D}(r_0,z,t)=\alpha V_0(t)\big(r_0^2+r_0^2\frac{z^2}{z_0^2}-2z^2\big)=\frac{V_0(t)}{2}, \tag{2.8}$$

with the condition $r_0^2=2z_0^2$ we get $\alpha=\frac{1}{2r_0^2}$.Consequently the potential inside the trap can be written

$$V_{3D}=\frac{V_0(t)}{2r_0^2}(r^2-2z^2). \tag{2.9}$$

Typically, the oscillating potential is

$$V_0(t)=V_{dc}-V_{rf}\cos(\omega_{rf}t) \tag{2.10}$$

The equations of motion are derived from

$$\frac{d\overrightarrow{v}}{dt} = q\frac{\overrightarrow{E}}{m}, \tag{2.11}$$

where q is the charge of the ions, and $\overrightarrow{E} = -\overrightarrow{grad}V$. So the equation of motion for $u = x, y, z$ are:

$$\frac{d^2u}{dt^2} = -\frac{q}{m}\frac{dV(x,y,z,t)}{du} \tag{2.12}$$

This is the so-called "Mathieu equation", obtained by posing $\tau = \frac{\omega_{rf}t}{2}$:

$$\frac{d^2u}{d\tau^2} + (a_u - 2q_u cos(2\tau))u = 0, \tag{2.13}$$

with the "Mathieu parameters":

$$a_{x,y} = -\frac{a_z}{2} = \frac{4qV_{dc}}{mr_0^2\omega_{rf}^2} \tag{2.14}$$

$$q_{x,y} = -\frac{q_z}{2} = \frac{2qV_{rf}}{mr_0^2\omega_{rf}^2}, \tag{2.15}$$

The parameters depend on the trap geometry, the trapping potential, and the ion mass. They determine the motion stability inside the trap. A stable solution of Mathieu's equation will be for a motion amplitude bound in all directions. Stable solutions [31, 32] are a superposition of oscillations with frequency

$$\omega_k = (2k+\beta)\frac{\omega_{rf}}{2} \text{ with } k = 0, 1, 2, ..., \infty. \tag{2.16}$$

The low-order component of motion ($k = 0$) is called "macro-motion" and $\omega_0 = \beta\frac{\omega_{rf}}{2}$. For more details see [31, 33]. A trapped ion thus oscillates at its macro-motion frequency in a pseudo-potential well D_u formed by the RF and operating parameters [31]:

$$\overline{D_u} = \frac{eV_{rf}^2}{4m\omega_{rf}^2 r_0^2} = \frac{q_u V_{rf}}{8}. \tag{2.17}$$

Ion guide: the 2D linear Paul trap

The use of 3D Paul traps for the collection of external ions proved difficult due to the strong RF fields experienced by ions entering the trap at large values of z (see [34]). The way to avoid this is to use a 2D trap.

An ion guide allows to trap ions in radial directions without disturbing the beam propagation. This kind of trap is also useful to work in continuous mode. The potential in a two-dimensional trap is defined by eq. (2.3). Such a potential can be made by using two pairs of infinite hyperboloid electrodes. The distance between two opposite electrodes is $2r_0$. For practical reasons cylindrical electrodes are used, with radius $r = 1.148r_0$, which is optimum to compensate for the non-hyperbolic form [28, 31]. A potential difference

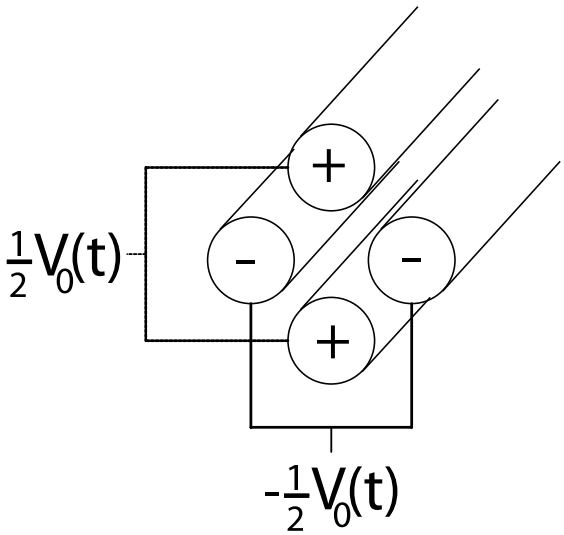

Figure 2.3: *Cylindrical electrodes used for the two-dimensional Paul trap with the applied potential.*

$V_0(t)$ is applied between each pair of opposite electrodes (see figure 2.3). The equations of motion are based on this potential. One obtains $a_x = -a_y$ and $q_x = -q_y$, defined by equations (2.14) and (2.15).

Figure 2.4 represents the line of stability for these parameters a and q in a 2D-Paul trap. Practically, we use $a = 0$, which means ions are stable for $0 < q < 0.91$ (see figure 2.4). This geometry, a radio-frequency potential applied on 4 cylindrical electrodes, is also called a Radio-Frequency Quadrupole (RFQ). The use of such a trap is described in section 4.2.

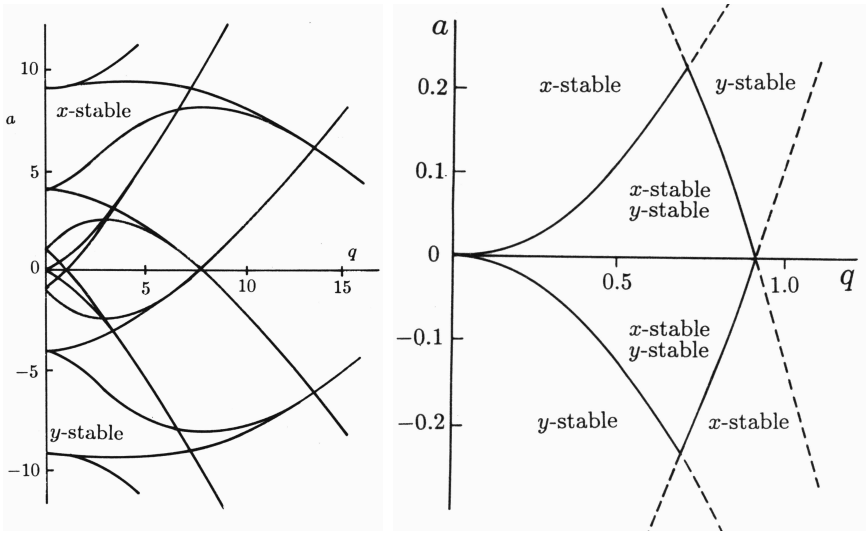

Figure 2.4: *Mathieu stability diagram of a 2D-Paul trap as a function of the parameter a and q. On the right a zoom in the region near (a,q)=0 is presented, with regions of stability in x- and y-direction.*

2.3 The Penning trap

In this part the principle and the properties of a Penning trap will be briefly explained as far as they apply to the ISOLTRAP spectrometer. For a more detailed description of the theoretical aspects concerning Penning traps see [35, 36, 37].

2.3.1 The trapping

This section presents how to trap ions with a Penning trap.

The electrode configuration of a Penning trap is the same as for a 3D-Paul trap (see figure 2.5) with a ring and two end-caps.

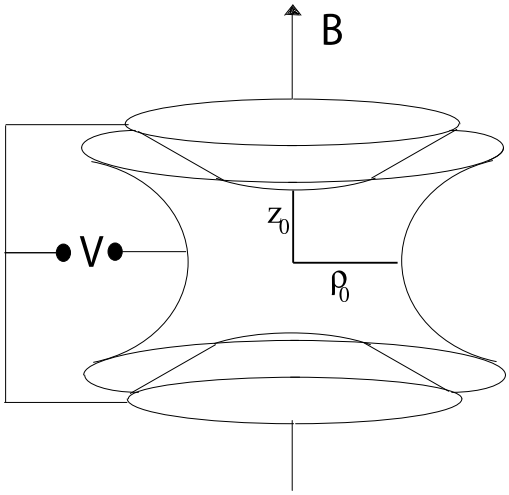

Figure 2.5: *Schematic drawing of a Penning trap. The difference with a 3D-Paul trap is the magnetic field and the static potential.*

The potential applied is

$$V(x,y,z) = \frac{V_0}{2\rho_0^2}(x^2+y^2-2z^2), \tag{2.18}$$

with V_0 a static potential. Since there is no time-varying electric field a magnetic field (in the axial direction) is applied to trap in the radial direction. The equations of motion are derived from:

$$m\frac{d\overrightarrow{v}}{dt} = q\overrightarrow{E} + q\overrightarrow{v} \wedge \overrightarrow{B}, \tag{2.19}$$

with q the charge of the particle, m its mass, and $\frac{d\overrightarrow{v}}{dt} = \overrightarrow{a}$. Thus,

$$\begin{bmatrix} a_x \\ a_y \\ a_z \end{bmatrix} = \frac{q}{m}\left(\begin{bmatrix} E_x \\ E_y \\ E_z \end{bmatrix} + \begin{bmatrix} v_x \\ v_y \\ v_z \end{bmatrix} \wedge \begin{bmatrix} 0 \\ 0 \\ B \end{bmatrix} \right) \tag{2.20}$$

with $\overrightarrow{E} = -\overrightarrow{grad}V$. In the axial direction z we obtain a harmonic oscillator equation:

$$\frac{d^2z}{dt^2} + \omega_z^2 z = 0 \text{ with } \omega_z = \sqrt{\frac{2qV_0}{m\rho_0^2}}, \tag{2.21}$$

which is independent from B. In the radial directions x and y one obtains

$$\frac{d^2x}{dt^2} - \omega_c\frac{dy}{dt} - \frac{\omega_z^2}{2}x = 0 \tag{2.22}$$

$$\frac{d^2y}{dt^2} + \omega_c\frac{dx}{dt} - \frac{\omega_z^2}{2}y = 0, \tag{2.23}$$

with $\omega_c = \frac{qB}{m}$ the cyclotron frequency of an ion in a magnetic field B. To solve these equations we have to use the complex representation $u = x + iy$ which leads to

$$\frac{d^2u}{dt^2} + i\omega_c\frac{du}{dt} - \frac{\omega_z^2}{2}u = 0, \tag{2.24}$$

the corresponding characteristic equation which one obtains by using $u = u_0\exp(-i\omega t)$ is

$$\omega^2 - \omega_c\omega + \frac{\omega_z^2}{2} = 0, \tag{2.25}$$

with the solutions

$$\omega_\pm = \frac{\omega_c \pm \sqrt{\omega_c^2 - 2\omega_z^2}}{2}. \tag{2.26}$$

The ion motion in a Penning trap is a superposition of three independent harmonic oscillator motions, one in the axial direction and two in the radial direction, *i.e.* the reduced cyclotron motion with frequency ω_+, and the slow magnetron motion with frequency ω_- [35, 38]. These motions are the consequence of the defocusing component coming from the fields coupling. The corresponding trajectory is presented in figure 2.6.

The relation between the frequencies, supposing a pure quadrupole field, is:

$$\begin{aligned} &\omega_c = \omega_+ + \omega_-, \\ &\omega_c^2 = \omega_+^2 + \omega_-^2 + \omega_z^2, \\ &\text{with } \omega_c \sim \omega_+ \gg \omega_z \gg \omega_-, \end{aligned} \tag{2.27}$$

This is the principle on which mass measurements in Penning traps are based. While the use of quadrupole fields seems complicated (introduction of an extra eigenmode), the description is exact.

The stability of the ions trajectory in the trap is defined by the condition

$$(\omega_c^2 - 2\omega_z^2) > 0 \tag{2.28}$$

for the term in the square root in equation (2.26). This leads to the condition

$$B^2 > \frac{4V_0 m}{q\rho_0^2}. \tag{2.29}$$

For instance, to measure a nuclide with mass 100u, and with a potential difference $V_0 =$ 5V, the required magnetic field is 5 T. This can only be realized by the use of superconducting magnets. A real Penning trap deviates in many aspects from the ideal Penning trap just described. These differences are explained in Chapter 5.

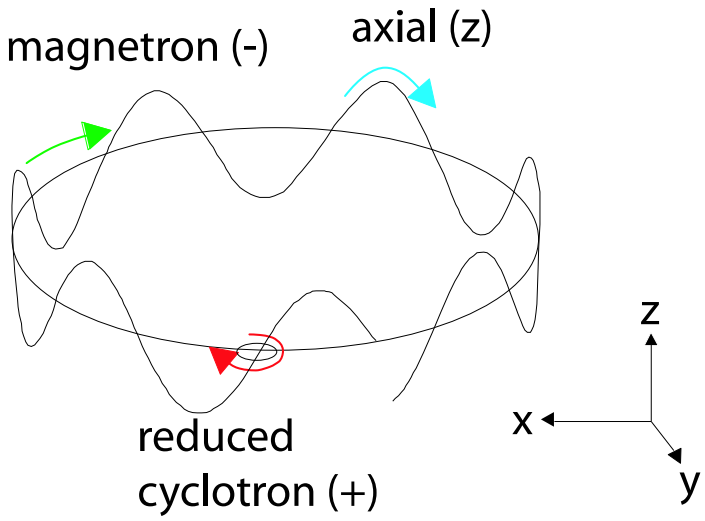

Figure 2.6: *Schematic representation of the three eigenmotions of an ion in a Penning trap: the slow magnetron motion, the fast reduced cyclotron motion and the axial motion produces by the electric field.*

2.3.2 The Excitation

A Penning trap can also be used to manipulate the ions, here are presented various excitations which can be applied to trapped ions.

In the previous section, the ion motion in a Penning trap was presented. But one also needs to manipulate the ion motion, *e.g.* to determine the cyclotron frequency, which may be done by measuring the different components of the motion: $\omega_+, \omega_-, \omega_z$. This means to measure three frequencies with their errors, so the final error on ω_c would be the sum of three errors, which leads to a smaller precision.

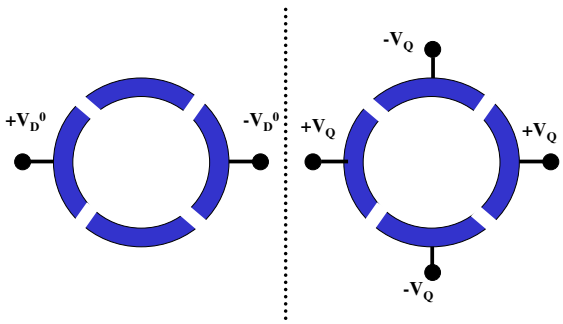

Figure 2.7: *Schematic view of the ring electrode with applied potential for dipolar (left) and quadrupolar excitation (right).*

To avoid this traps are also used in "excitation mode": dipolar or quadrupolar excitations (see figure 2.7) are applied. To do so the ring electrode in a hyperboloid Penning trap, or the central electrode for a cylindrical one, are segmented in four parts in order to apply an azimuthal time varying field to excite the radial ion motion. Here, only the results from these excitations are described, for further details see [38, 39].

A dipolar excitation increases the motional radius of all ions inside the trap, irrespective of their mass. Quadrupolar excitation applied at a sideband, as *e.g.* $\omega_c = \omega_+ + \omega_-$, results in a conversion between magnetron and reduced cyclotron motion [36].

Dipolar excitation

In this case, a sinusoidal voltage with frequency ω_D and amplitude V_D^0 is added to V_0. The corresponding dipolar potential is:

$$V_D(x,t) = \frac{V_D^0}{2\rho_0^2}\cos(\omega_D t + \phi_D)\cdot x, \tag{2.30}$$

with the rf phase ϕ[1]. The corresponding electric field induced by this potential is:

$$\vec{E}_D = -\overrightarrow{grad}V_D = -\frac{V_D^0}{2\rho_0^2}\cos(\omega_D t + \phi_D)\cdot \vec{u}_x. \tag{2.31}$$

The equations of motion (eq. (2.21), (2.22), and (2.23)) thus become:

$$\frac{d^2x}{dt^2} - \omega_c\frac{dy}{dt} - \frac{\omega_z^2}{2}x = -\frac{V_D^0}{2\rho_0^2}\cos(\omega_D t + \phi_D) \tag{2.32}$$

$$\frac{d^2y}{dt^2} + \omega_c\frac{dx}{dt} - \frac{\omega_z^2}{2}y = 0 \tag{2.33}$$

$$\frac{d^2z}{dt^2} + \omega_z^2 z = 0. \tag{2.34}$$

These equations lead to the expression of motions radii listed in ref [35, 36, 38, 39], depending on ω_D. They show that when the applied frequency, ω_D, is close to the $\omega_\pm$ frequency the corresponding radius increases, it means a dipolar excitation performed at the right frequency allows to increase a motion radius.

Quadrupolar excitation

The oscillating azimuthal quadrupole field created via a four-segmented ring electrode is:

$$E_x = \frac{V_Q}{2a}\cos(\omega_Q t + \phi_Q)\cdot y \tag{2.35}$$

$$E_y = \frac{V_Q}{2a}\cos(\omega_Q t + \phi_Q)\cdot x, \tag{2.36}$$

where ω_Q and ϕ_Q are the frequency and the phase of the rf field. The amplitude V_Q corresponds to the maximum potential of the quadrupole rf field on a circle with radius a.

In general this type of excitation allows the coupling and the conversion of the radial eigenmotions (including harmonics) [35, 38]. This kind of manipulation is exploited for mass measurements as explained in Chapter 3

[1] The x-direction is chosen arbitrarily as represented in figure 2.7.

2.4 Ion beam cooling

Trapping and cooling cannot be achieved individually, the ion beam cooling can be used for ion beam preparation.

The reduction of the dimension and the dispersion of an ion beam is directly related to the diminution of the temperature. To understand this relation, one has to refer to our "old" statistics lectures: in the beam referential, ions are a statistical unit. The ions density in the phase space is distributed according to the Boltzmann law, which can be adapted to the ions velocity in one direction. This becomes the Maxwell-Boltzmann distribution [28]:

$$f(v_x) = \sqrt{\frac{m}{2\pi kT}} e^{-\frac{mv^2}{2kT}}. \tag{2.37}$$

For more details see [40].

Different methods of cooling exist: Resistive cooling [31], electron cooling [41], stochastic cooling [42], laser cooling [43, 44, 45], and buffer gas cooling [46]. Due to its universal nature but especially because of its rapid time constant (milliseconds) buffer gas cooling has emerged as the dominating cooling mechanism in trapping techniques applied to exotic nuclides. Therefore only this cooling technique will be discussed in the context of this thesis.

Buffer-gas cooling

If the ions move through a buffer gas, there is an energy exchange between ions of the beam and gas atoms. Ions have a temperature well above the temperature of the buffer gas atoms because of their kinetic energy. This method needs an infinite reservoir of cold, light, inert gas that takes energy from the ions. The diffusion induced by collisions requires the use of confinement. By forcing ions on their initial trajectory, the traps are a good answer to this problem.

Collisional cooling by buffer-gas atoms of ions trapped in a Paul trap has been examined both theoretically and experimentally in [47, 48, 49]. It has been found that the confinement time has a strong dependence on the *a-q* parameters of the stability diagram. The confinement time is shorter with light buffer gases. This is due to the RF (Radio-Frequency) heating [34], which is the increase of the ion energy by colliding with the gas atoms. These collisions move the ion from the center of the trap to a region with less trapping action. The bigger the mass of the gas atoms compared to the mass of the ions, the more important is this RF-heating. The RF-heating is minimal when $m_{gaz}/m_{ion} \ll 1$.

Savard *et al.* [50] have demonstrated a mass-selective collisional cooling technique for heavy ions in a Penning trap. In this method the cyclotron motion is cooled by collisions with buffer-gas atoms. The radial diffusion of ions, caused by buffer gas collisions, which increases the magnetron motion radius, is counteracted by imposing an additional azimuthal RF quadrupole field at the sum frequency of the magnetron and reduced cyclotron motions. There is a coupling between these two motions, which increases the reduced-cyclotron motion and decreases the magnetron motion. This effect completely transforms the magnetron motion into the reduced cyclotron motion [31]. The presence

of a buffer gas, such as helium, cools the fast components of this ion motion through collisions; the reduced cyclotron radius decreases. An application of the quadrupole excitation in combination with the buffer gas cooling therefore cools and centers the entire ion cloud mass selectively, because the cyclotron frequency ω_c is mass selective: $\omega_+ + \omega_- = \omega_c = \frac{qB}{m}$ (see figure 2.8) [38].

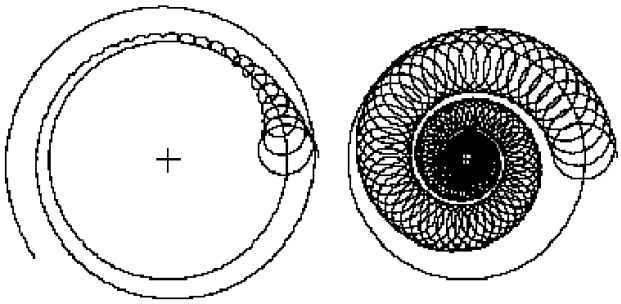

Figure 2.8: *Ion motion under quadrupolar excitation. Left: without gas in the trap. Right: with gas interacting with ions in the trap. The interaction with the gas cools and centers the ion motion.*

Chapter 3

Two complementary spectrometers: MISTRAL and ISOLTRAP

Both MISTRAL and ISOLTRAP experiments are located at ISOLDE (figure 1.5). While ISOLTRAP carefully excites stored-ions motion, MISTRAL excites the ions in-flight, giving access to the shortest-lived species.

3.1 The MISTRAL technique

The MISTRAL spectrometer is a transmission spectrometer, described briefly in the following.

MISTRAL [51, 52] (Mass Measurements at ISOLDE with a Transmission and Radiofrequency Spectrometer on-Line) is installed in the ISOLDE hall since 1997. It is described in detail in various theses [28, 53, 54]. Here only the general features of MISTRAL will be presented.

MISTRAL is a transmission mass spectrometer based on the principle proposed and realized by L.G. Smith [55]: radio-frequency excitation of ions rotating in a homogeneous magnetic field. Its rapidity (flight duration of around 50μs) allows mass measurements of nuclides with very short half-lives such as ^{11}Li with $T_{1/2}$=8.75 ms, recently accomplished with a mass uncertainty of 5 keV [56].

The spectrometer consists mainly of a homogeneous magnetic field (0.8 T) in which the 60-keV ISOLDE beam performs a two-turn helicoidal trajectory (figure 3.1). At the end of the first half-turn and after the third half-turn, ions go through a radio-frequency modulator which changes their kinetic energy. The first time, they are drawn aside from the nominal trajectory and their radius is becoming larger or smaller depending on the radio-frequency phase. If during the second passage in the modulator the change of kinetic energy is exactly compensated, they are back on the nominal trajectory at the end of the last half-turn, and they can exit through the 0.4 mm ejection slit to be counted.

Since the motion is isochronous, *i.e.* the cyclotron frequency $f_c = qB/2\pi m$ is not depending on the kinetic energy of the ion or on the diameter of its trajectory, the transmission of the ion through the system can be controlled by adjusting the frequency of the modulation. There is then a condition of resonance between the cyclotron frequency f_c of

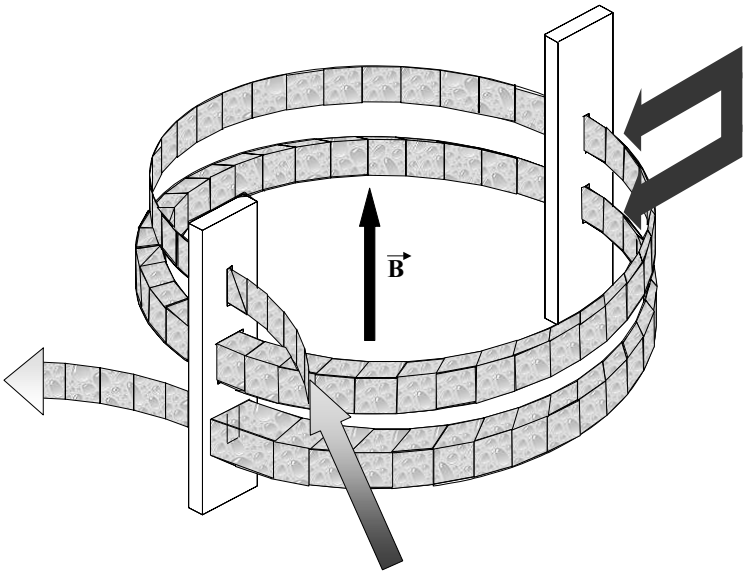

Figure 3.1: *The trajectory envelope of ions inside MISTRAL: ions are in a homogeneous magnetic field. They are making two turns before to exit the setup. First, there is the 0.4 mm injection slit followed by the modulation, done after one half-turn and three half-turns, and finally they exit from the 0.4 mm ejection slit.*

the ions in the magnetic field and the frequency f_{RF} of the excitation:

$$f_{RF} = (n + \frac{1}{2}) \cdot f_c, \tag{3.1}$$

with n an integer representing a harmonic of the radio-frequency. A scan of f_{RF} is presented in figure 3.2, which shows a frequency spectrum made of equidistant peaks separated by f_c. So the measurement of f_c can be obtained from the transmission peaks. The mass determination should be complemented by the measurement of the magnetic field. But to perform high-precision measurements, the accuracy of the magnetic field determination is inadequate. To avoid this problem, the measurement of a mass A is compared to that of a well-known reference mass B produced by MISTRAL's off-line ion source.

$$f_c^A = \frac{qB}{2\pi m^A} \text{ and } f_c^B = \frac{qB}{2\pi m^B} \tag{3.2}$$

We assume that during the measurement of these two frequencies (less than one minute) the magnetic field variation ($\sim 3 \cdot 10^{-7}$) is well below the required precision. So it leads to:

$$m^A \cdot f_c^A = m^B \cdot f_c^B. \tag{3.3}$$

The mass resolving power of this spectrometer is defined by:

$$R = \frac{m}{\Delta m} = 2\pi n \frac{D_m}{w} \tag{3.4}$$

where n denotes the harmonic, w the exit slit width, and D_m the trajectory diameter variation. This mass resolving power is not depending on the ion mass: $R \propto \sqrt{m}$. We will see in the following that this also the case for Penning traps.

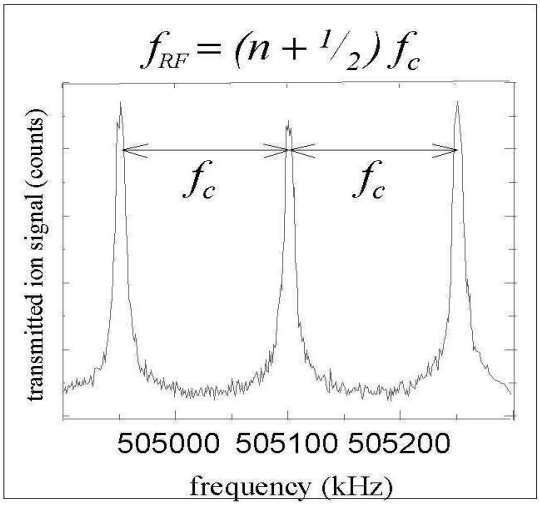

Figure 3.2: *Transmitted ion signal as a function of the modulation radio-frequency. Each peak represents a successive different harmonic number. The distance between two peaks is the cyclotron frequency f_c.*

The mass resolving power is thus directly related to the exit slit size. Moreover, the slits define the ion path inside the magnet through the region of homogeneity of the magnetic field. In a compromise between transmission and resolving power, a slit size of 0.4 mm width and 5 mm height was chosen. The slits and the optimization of n and D_m lead to a mass resolving power up to 10^5. But this geometry is a limitation in the transmission through the mass spectrometer. A solution to improve this transmission was the development of an ion beam cooler, like the one developed for ISOLTRAP (see next section), described in Chapter 4. This ion beam cooler has the particularity to be fast enough to pursue MISTRAL measurements on short-lived nuclides.

3.2 The ISOLTRAP experiment

The ISOLTRAP is a triple-trap spectrometer, here will be describe its setup and its principle.

3.2.1 Experimental setup

ISOLTRAP is a high-precision Penning trap mass spectrometer, located at ISOLDE. It is divided in three main parts (see figure 3.3): First, a linear gas-filled radio-frequency quadrupole (RFQ) dedicated to adapt the 60-keV ion beam coming from ISOLDE to the ISOLTRAP requirements in respect to kinetic energy, time structure, and beam emittance [57]. The second part is a gas-filled cylindrical Penning trap used for isobaric cleaning. The cooled ion bunch is then transferred to the precision Penning trap for isomeric separation (if necessary) and for the mass measurement. These two traps are described in

detail in [58, 59].

The linear gas-filled radio-frequency quadrupole (RFQ) is a cooler and buncher (see figure 3.4) [60]. It transforms the quasi-continuous 60-keV ion beam into short ion bunches at low energy (2.7 keV). This is needed is order to transfer and capture the ions into the first Penning trap.

The cylindrical Penning trap [59], installed in a superconducting magnet (B=4.7 T), called the "cooler" trap (see figure 3.5) is used for isobaric cleaning of the beam by exploiting a helium-buffer gas cooling technique [50], described in section 2.4, with a resolving power of up to 10^5. The buffer gas pressure is about $10^{-3} - 10^{-4}$ mbar.

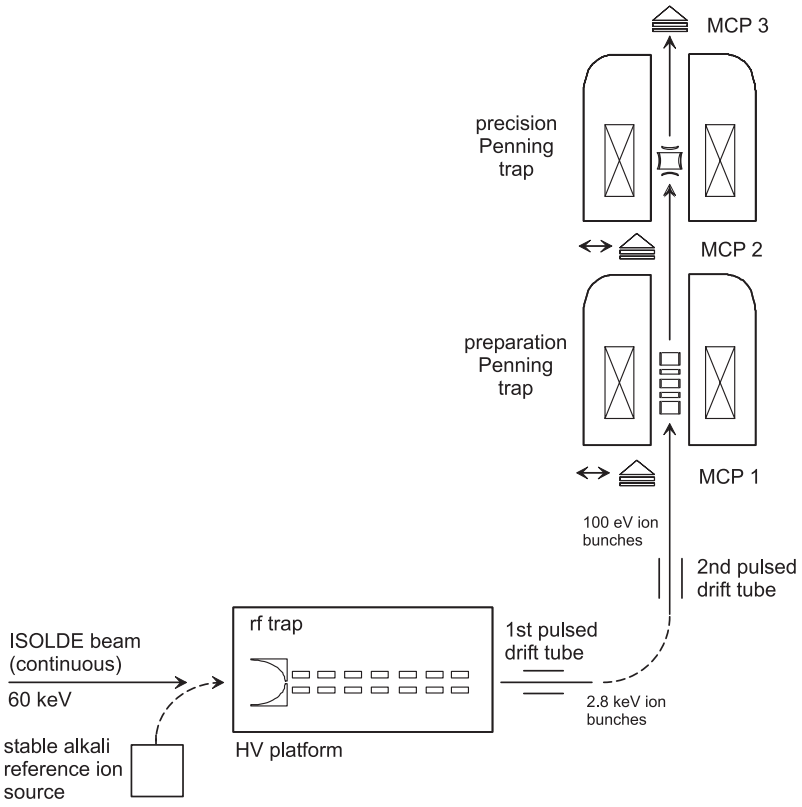

Figure 3.3: *Experimental setup of the ISOLTRAP mass spectrometer, showing the main parts: a gas-filled linear radio-frequency quadrupole (RFQ) trap for capturing and preparing the ISOLDE beam, a gas-filled cylindrical Penning trap for isobaric separation and a high-vacuum hyperboloidal Penning trap for the mass measurement.*

The precision Penning trap is also installed in a superconducting magnet, now with B = 5.9 T magnetic field strength. The mass measurement is carried out by determining the cyclotron frequency of the stored ions, using a time-of-flight detection method [61] on ions extracted from this trap (see next section).

A micro-channel plate detector (MCP) is installed at the very top of the experimental setup (see figure 3.3). Typical detection efficiencies for this type of detector are from 30 to 60% [62, 63]. This detector will be exchanged by a Channeltron [64], with up to 90% detection efficiency. The overall efficiency in the ISOLTRAP setup, which is mainly limited by the buncher efficiency of 20 % [60], is $\sim 2\%$.

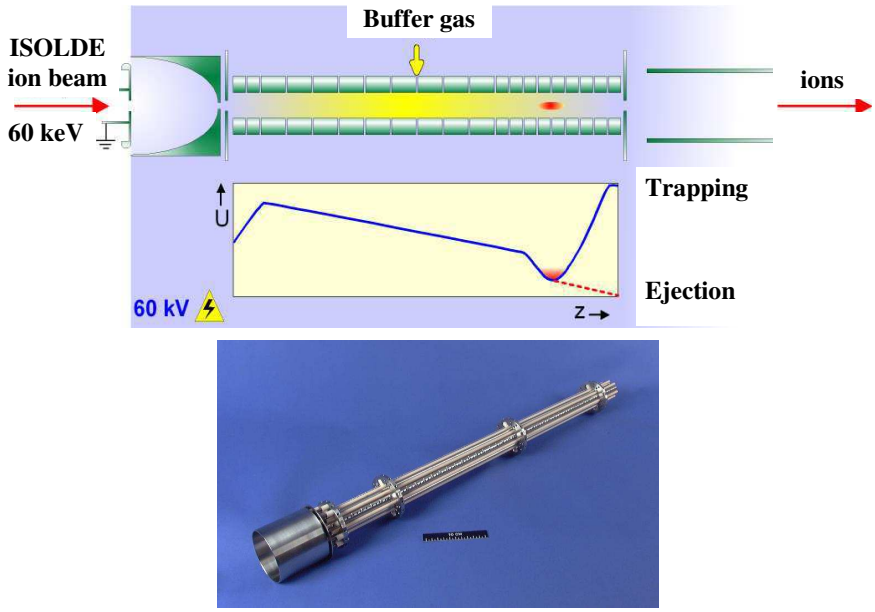

Figure 3.4: *The radio-frequency ion beam cooler and buncher with the potential along the direction of propagation of the ions. Ions are trapped before to be ejected. The lower part shows a picture of the quadrupole.*

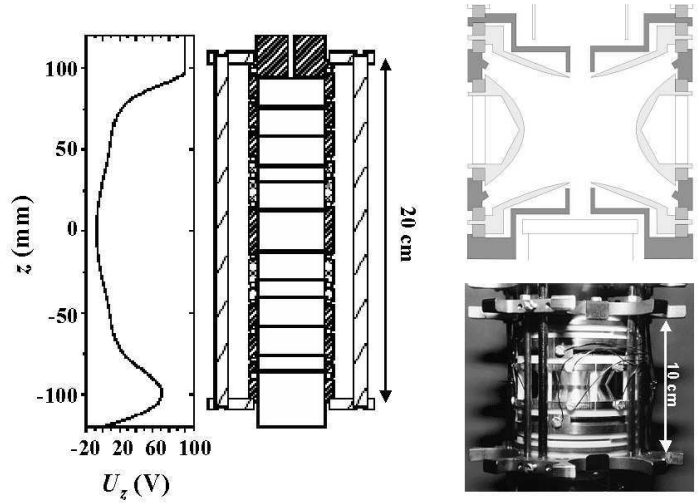

Figure 3.5: *The two Penning traps of ISOLTRAP. The left part shows the electrodes and axial potential on the "cooler" trap. Right: the precision Penning trap, described in details in Chapter 5.*

3.2.2 Principle of a mass measurement: experimental procedure

The mass measurement is based on the cyclotron frequency f_c measurement like for MISTRAL. In the same way, to measure with a high-accuracy the mass, the magnetic field has to be known with a high-precision. To avoid this problem the ratio between the frequency of the ion of interest and a well-known reference mass is measured. To do so ISOLTRAP has its own off-line ion source which can also be used for tuning the spectrometer (see Chapter 5).

The ion beam is alternatively injected (for each measurement around 3000 ions are used) from ISOLDE or from the off-line ion source, to the buncher. This cooler-buncher is depicted in figure 3.4, a segmentation of the electrodes is needed to obtain an axial trapping. A beam gate enables only a part of the beam to enter the RFQ to chose a proper number of ions going in the two Penning traps in order not to overfill the precision Penning trap, thus avoiding ion-ion interactions in this trap. The capacity of the precision trap is limited to 10 ions to avoid space charge effects which can cause frequency shifts.

The bunch coming from the RFQ is sent to the cooler trap where the ions are trapped. Interaction with the gas inside the trap is cooling the axial motion. Then a dipolar excitation with a frequency ν_- is applied to increase the magnetron radius of all ions. Their radius is then too big to be extracted through the exit hole of the trap. To select the ions of interest and to bring them back to the center of the trap, the mass-dependent quadrupolar excitation at frequency ν_c is applied. This way the trap is an isobar separator with a resolving power $R = \frac{m}{\Delta m}$ around $10^4 - 10^5$ [59].

Ions coming from the cooler trap are captured in the upper trap by changing the potential on the lower end-cap (for more details see Chapter 5). When the time of capture is correct, ions end up in the center of the trap, which is at the same potential as the ring electrode, so their axial energy is minimal. Different excitations are performed in this trap. First a dipolar excitation at ν_- is applied to increase the radius like in the cooler trap. Then if there are some contaminants (like isomers) a second mass dependent dipolar excitation is performed at ν_+ to remove unwanted species. Finally a radio-frequency azimuthal quadrupole field is applied to convert pure magnetron motion into cyclotron motion. At $\nu_{rf} = \nu_c$ a full conversion is obtained, leading to an increase of the orbital magnetic moment μ and the radial kinetic energy $E = \mu B$ [65]. After ejection at low axial energy, ions go through the inhomogeneous part of the magnetic field. Since the axial acceleration in this fringe field is proportional to μ the shortest time-of-flight (TOF) is observed for $\nu_{rf} = \nu_c$ (see figure 3.6).

All these excitations are applied with a precise timing scheme shown in figure 3.7. It presents typical timings used for slow and fast measurement processes. Usually the slow process is used, the fast one is for very short-lived ions, as *e.g.* ^{74}Rb [66] with 65 ms half-life measured by ISOLTRAP in 2004.

As an example of a cyclotron frequency measurement, figure 3.6 represents a resonance curve for ^{85}Rb with in total $\sim$ 3000 ions. The TOF as a function of the applied radio-frequency is shown. The solid line is a fit of the theoretical expected line-shape [38] to the data points, the side bands are due to the excitation profile: a Fourier transformation of a rectangular shaped excitation.

The mass resolution and the precision of the determination of the cyclotron frequency depends strongly on the excitation time. The line width $\Delta\nu$ of the resonance is mainly de-

termined by the duration of the applied RF-field (T_{RF}) for coupling the two radial motions. The relation is [60]:

$$\Delta\nu(FWHM) \sim \frac{0.9}{T_{RF}}. \tag{3.5}$$

An example of this strong dependence is shown in the inset of figure 3.8 which depicts cyclotron frequency measurements of ^{85}Rb for different excitation times. The resolving power is also limited by the residual gas pressure inside the trap ($P \simeq 10^{-9}$). At this pressure the probability of collisions with an atom will change the relative amplitudes and phases of the different eigenmodes inside the trap. Typically $T_{RF} = 300$ or 900 ms are used. Moreover, higher resolving powers and higher statistics improve the mass precision:

$$\frac{\delta m}{m} \propto \frac{T_{RF}}{R\sqrt{N}}, \tag{3.6}$$

with N the number of ions and R the resolving power. The relative mass accuracy typically obtained is 10^{-8} [67].

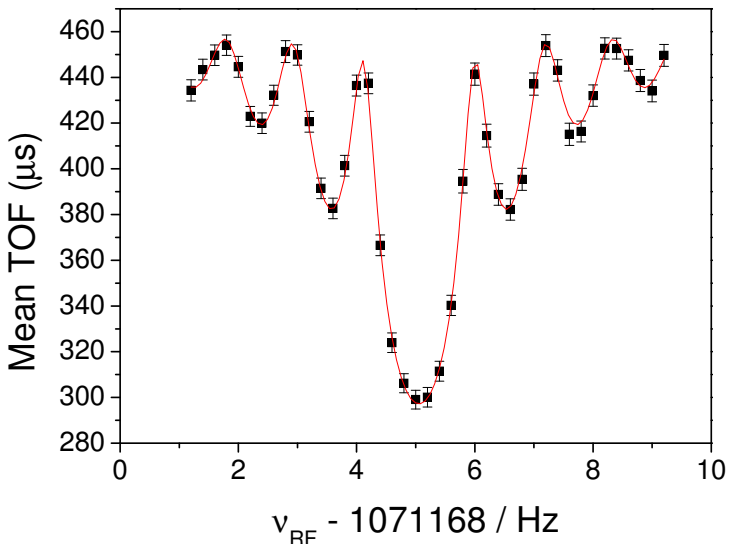

Figure 3.6: *Time of flight (TOF) as a function of the applied radio-frequency excitation for $^{85}Rb^{+}$ ions. This measurement was performed with 3000 ions and an excitation time $T_{RF} = 900$ ms. The corresponding relative frequency uncertainty is $\delta\nu/\nu = 9 \cdot 10^{-9}$.*

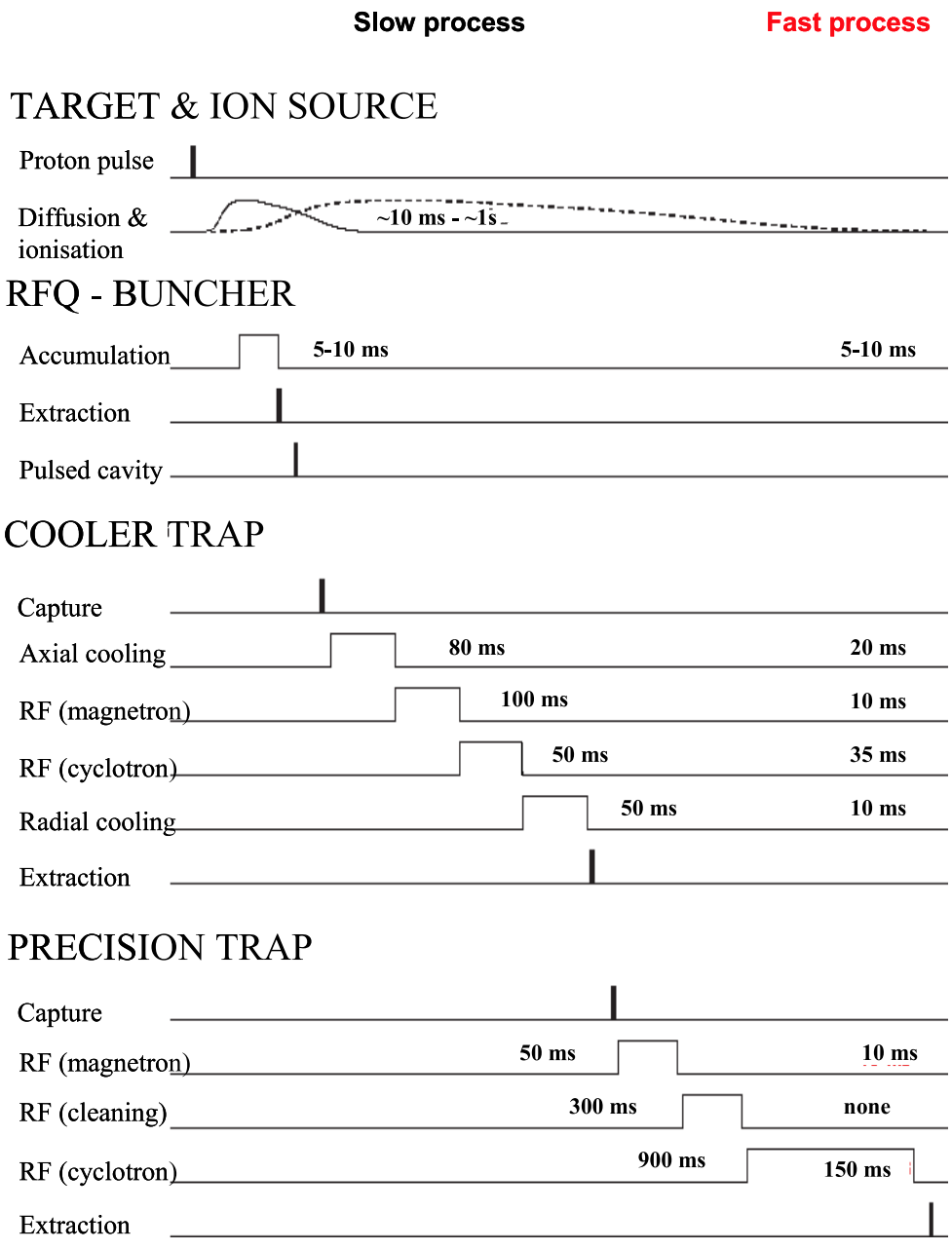

Figure 3.7: *Time sequence of an ISOLTRAP mass measurement cycle for a slow (1.5 s) and a fast process (240 ms). The latter is used for very short-lived nuclides like ^{74}Rb (65ms half-live).*

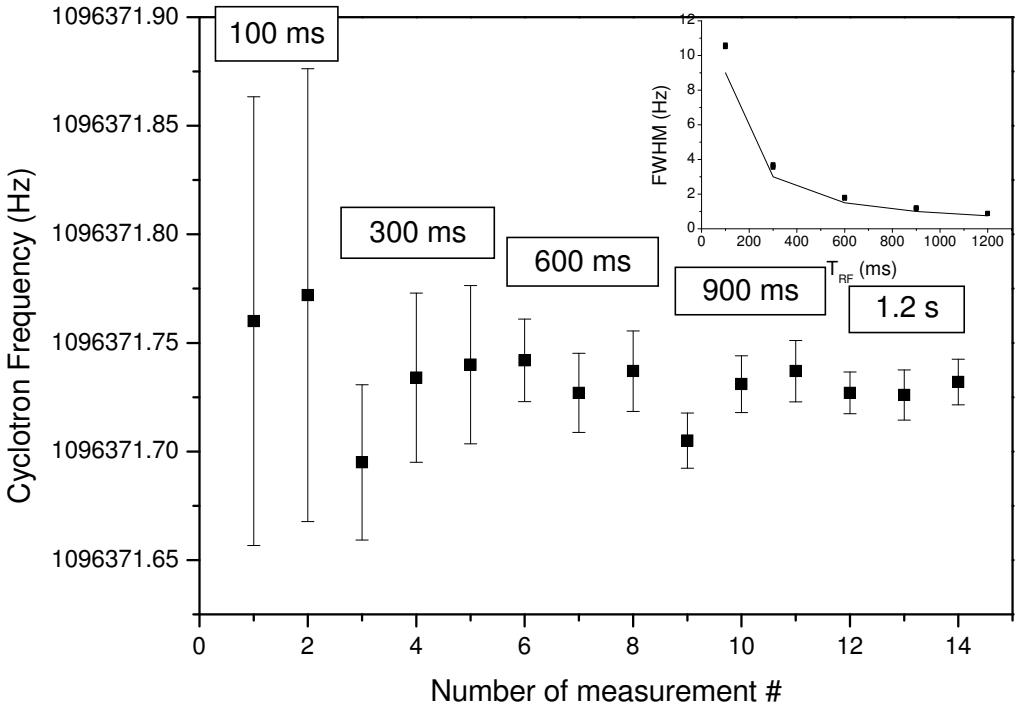

Figure 3.8: *Cyclotron frequency measurements for different excitation times (T_{RF}). The better accuracy is achieved for the longest T_{RF}, here 1.2 s. The inset shows the line width of the resonance as a function of T_{RF}: the experimental points and the theoretical behavior described by eq.(3.5).*

3.3 Comparison between ISOLTRAP and MISTRAL

MISTRAL and ISOLTRAP are two complementary spectrometers because of the part of the nuclear chart they can measure.

MISTRAL and ISOLTRAP are two complementary spectrometers. They are both based on cyclotron frequency measurements, but since ISOLTRAP is trapping ions, it cannot reach very short-lived nuclides, while MISTRAL, which is a transmission spectrometer, can. Another difference is the precision achieved by these spectrometers: $1 \cdot 10^{-8}$ in the case of ISOLTRAP, $5 \cdot 10^{-7}$ in the case of MISTRAL. Nowadays traps are the most accurate tools for mass measurement. So the complementarity is coming from the fact that ISOLTRAP is measuring with a better accuracy than MISTRAL, but ISOLTRAP cannot measure nuclides MISTRAL has access to. Another difference is the capacity of the traps in ISOLTRAP: 10^6 ions for the buncher, 10^5 for the cooler trap and 10 ions in the precision trap (to avoid space charge), while for MISTRAL there is no limitation in the incoming number of ions.

These two spectrometers have their own limitations. A limitation of MISTRAL is its transmission which is determined by the slits. These slits determine the ion trajectory into

the homogeneous part of the magnetic field, which is very small since MISTRAL is not using a superconducting magnet. The limitation of the transmission is dramatic for very low production rates of very short-lived nuclides. To solve this problem COLETTE, an ion beam cooler, is being installed at MISTRAL. This is described in Chapter 4. One of the limitations of ISOLTRAP is the precise control of the fields inside the precision trap. To ensure a good precision and a very good accuracy of the measurements, fields should be as much as possible optimized. This is presented in Chapter 5.

Part II

Pushing the limits of MISTRAL and ISOLTRAP

Chapter 4

A beam cooler for MISTRAL

COLETTE is the ion beam cooler developed to increase MISTRAL's transmission. It is based on the use of a linear Paul trap filled by buffer gas.

4.1 Acceptance and Emittance: Definitions

A notion is used in term of beam definition: the emittance, the acceptance is a geometrical property linked to the emittance.

4.1.1 Emittance

In an ion beam each particle is defined by its "phase-space" [68] position, *i.e.* its position (x,y,z) and its momentum (p_x,p_y,p_z). This leads to the definition of the emittance: the hypervolume in the phase-space englobing all the particles of the beam:

$$\varepsilon = \int_V dx \cdot dy \cdot dz \cdot dp_x \cdot dp_y \cdot dp_z. \tag{4.1}$$

This quantity is used to calculate the evolution of a particle ensemble with time. To simplify this notation, we can consider the motion in one direction independently from the two others. The resulting emittance for each component becomes:

$$\varepsilon_u = \int du \cdot dp_u \qquad \text{for } u = x,y,z. \tag{4.2}$$

All the points included in this ε_u are represented by a surface for each dimension. This surface is theoretically an ellipse.

Liouville's theorem [69] plays an important role for the emittance evolution: it states that the emittance is conserved under conservative forces, *e.g.*, electric and magnetic field influences. The shape of the ellipse can be changed but the area is conserved. To reduce the emittance, dissipative forces must therefore be used.

The representation most used to depict an ion beam is to draw the emittance in (x,x') and (y,y'), with z the direction of propagation, $x' = \frac{p_x}{p_z}$, and $y' = \frac{p_y}{p_z}$. Figure 4.1 shows the emittance: it is defined by the area of the ellipse divided by π. The area of the ellipse is $2p \cdot 2q\frac{\pi}{4} = \pi pq = \pi ab$, so the emittance is $\varepsilon = pq = ab$, in π·m·rad, usually expressed in π·mm·mrad for ISOLDE beams. The emittance has various properties:

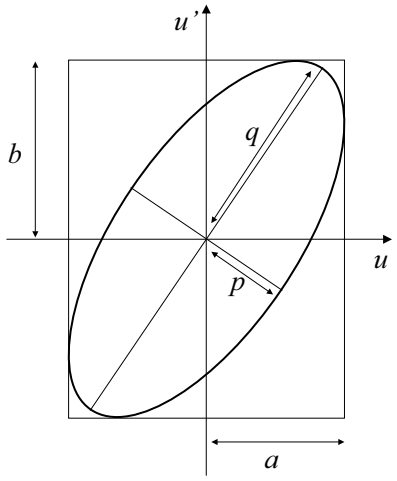

Figure 4.1: *The emittance definition for u = x or y, with p and q the ellipse parameters.*

- The definition of the measured emittance is the ellipse englobing 95% of the beam.
- x' and y' are directly related to the energy via p_z. So the emittance is depending on the transport energy: it is inversely proportional to the square root of the energy.
- The emittance defined initially will evolve with beam transport, as shown in figure 4.2: the ellipse orientation reflects the beam property.

4.1.2 Acceptance

The acceptance is geometrically defined as the maximum emittance that can enter a specific device. For MISTRAL one has to consider the trajectory of ions inside the 5 slits of the spectrometer with 0.4 mm horizontally and 5 mm vertically width. Its acceptance is 2π·mm·mrad vertically and 2π·mm·mrad horizontally [70, 28].

The emittance of the ISOLDE beam is roughly 35π·mm·mrad[1]. in both directions. This results in a loss of transmission of more than 94%, as it is shown in figure 4.3. The transmission in MISTRAL is even less, only around 10^{-4} because of the shape of the emittance which is distorted during beam transport.

To increase the transmission of MISTRAL, we can either increase the acceptance or decrease the emittance. Increasing the acceptance means a loss of resolving power for MISTRAL and an increase of the region of magnetic field homogeneity has so far proved impossible. So the only solution is to decrease the emittance by using dissipative forces. Different methods of cooling are explained in Chapter 2. The buffer-gas cooling was chosen, because it is the easiest method.

[1]For the surface ion source [71]

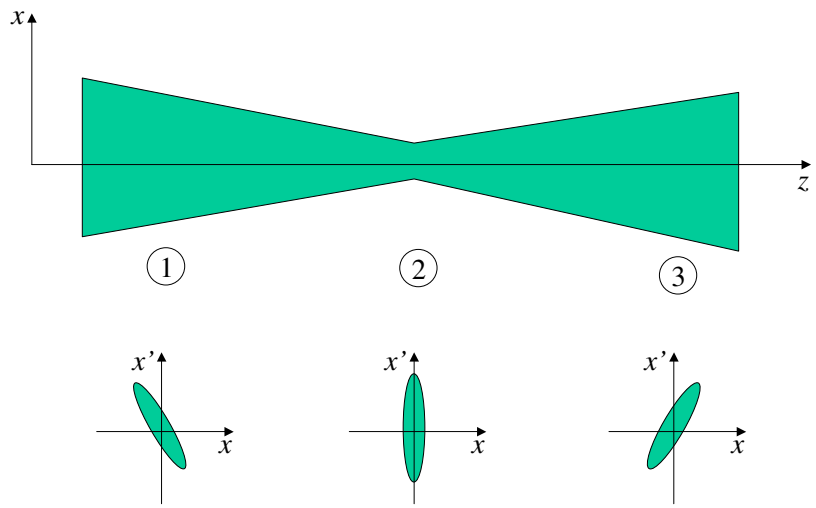

Figure 4.2: *Evolution of the emittance for a (1) converging, (2) focalized, and (3) diverging beam. The area is the same in each case because of Liouville's theorem.*

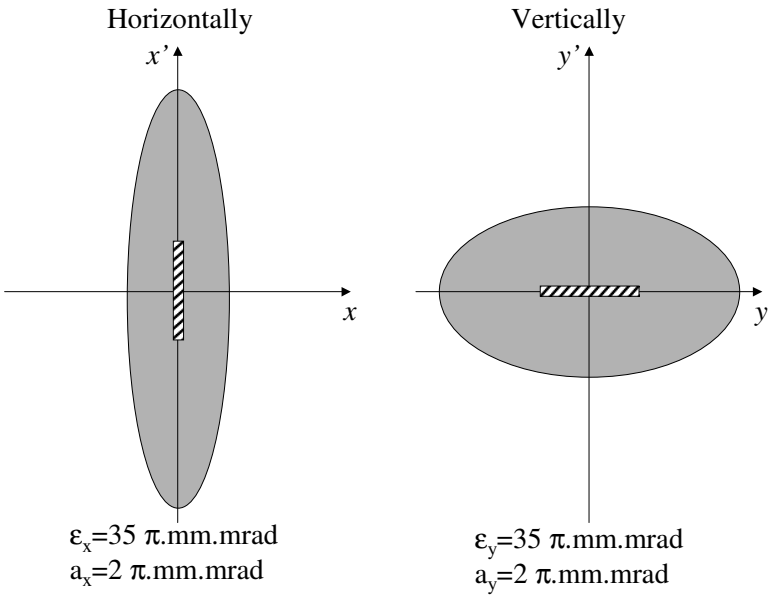

Figure 4.3: *ISOLDE emittance compared to MISTRAL acceptance in both directions. For elliptic emittances less than 6% of the beam can enter the MISTRAL experiment.*

4.2 COLETTE experimental setup

COLETTE is the ion beam cooler developed to increase the transmission of MISTRAL by decreasing the ISOLDE beam emittance. It was first tested in Orsay on the SIDONIE separator.

4.2.1 COLETTE

The challenge of COLETTE is two-fold: it has to reduce the ISOLDE beam emittance by at least a factor of one hundred, but also to be fast enough to continue the MISTRAL program of measurement: mass measurements of short-lived nuclides.

For this purpose COLETTE is constituted of a gas-filled 2D-Paul trap, shown in figure 4.4 with radius $r_0 = 7$ mm. The Paul trap is used to counteract the beam diffusion due to the interaction with the gas. To give the ions enough time to interact with the gas without stopping them (*i.e.* to be fast), the Paul trap is operated at high-voltage to decelerate the beam to few tens of eV. The Paul trap is composed of four rods, divided into 15 segments to produce an axial field to allow the beam to reach the extraction electrodes. Figure 4.5 presents the axial potential applied to the quadrupole electrodes. Moreover the "hill" potential applied at the entrance of the quadrupole is necessary to decrease the ions energy to few eV before interacting with the gas, while the decreasing potential after the hill serves to give to the ions enough energy to reach the extraction electrodes.

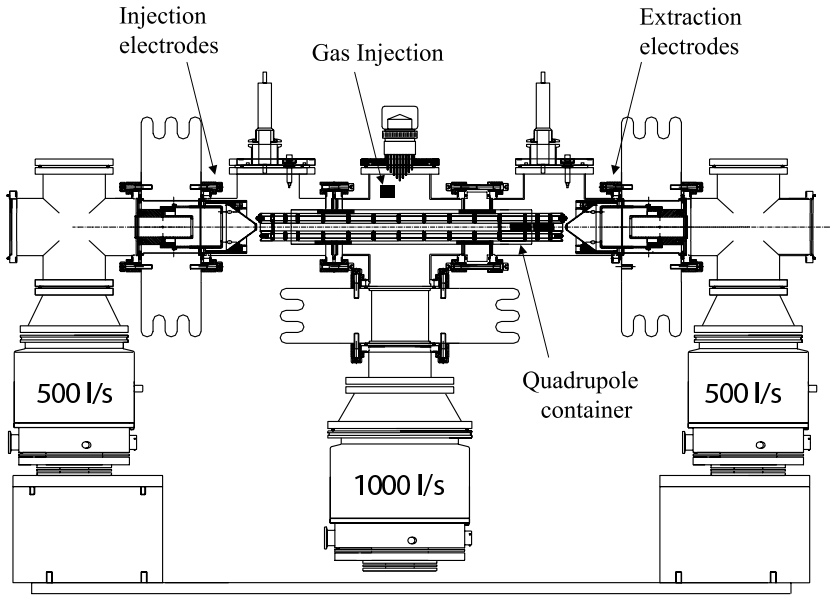

Figure 4.4: *Schematic drawing of the COLETTE setup with its radio-frequency quadrupole, its set of injection and extraction electrodes, and the pumping system. A photo is presented in figure 4.13.*

Three pumps are used to limit the gas diffusion outside of the quadrupole. A chamber is also installed around the quadrupole to control the gas diffusion. Without this differential pumping the ion beam would also interact with the gas outside of the trap and the diffusion would increase the beam loss [72]. The buffer-gas pressure is an important

parameter in determining the transmission of ions through the cooler. To check this transmission of COLETTE two Faraday cups were installed at the entrance and at the exit. Another parameter is the frequency and the amplitude of the radio-frequency applied to the Paul trap, since both directly determine the trapping capacity via the Mathieu parameter "q", and the pseudo-potential D (see Chapter 2). All these parameters were used to optimize the transmission of COLETTE.

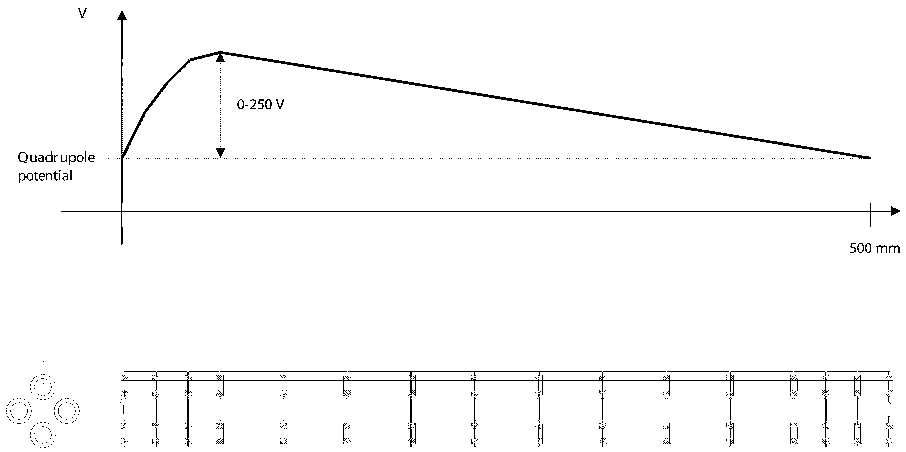

Figure 4.5: *Axial potential applied to the segmented electrodes of the RFQ use to allorw the beam to reach the ejection electrodes.*

4.2.2 SIDONIE

Before installing COLETTE on MISTRAL, a "low-energy" prototype was first tested at 10 keV [33] using a surface ionization ion source. To test the COLETTE setup at 60 keV, it was installed behind the isotope separator SIDONIE [73] at the CSNSM-Orsay. This separator can provide a beam comparable to the ISOLDE one concerning energy and emittance structure. The ion beam, produced by a "Bernas-Nier" source, is separated by a high dispersion analyzing magnet. Then a set of electrostatic quadrupoles and plates are installed to control the ion beam trajectory (see figure 4.6). COLETTE is installed instead of the "decelerating device" normally used to produce thin targets.

Before installing COLETTE on SIDONIE, the emittance-meter [33, 74] was used to measure the emittance at the exit of SIDONIE. Its principle is based on the electrostatic sweeping of the beam in front of two slits. It can determine the emittance in both the vertical and horizontal directions. The emittance was found to be 65π·mm·mrad vertically and 25π·mm·mrad horizontally.

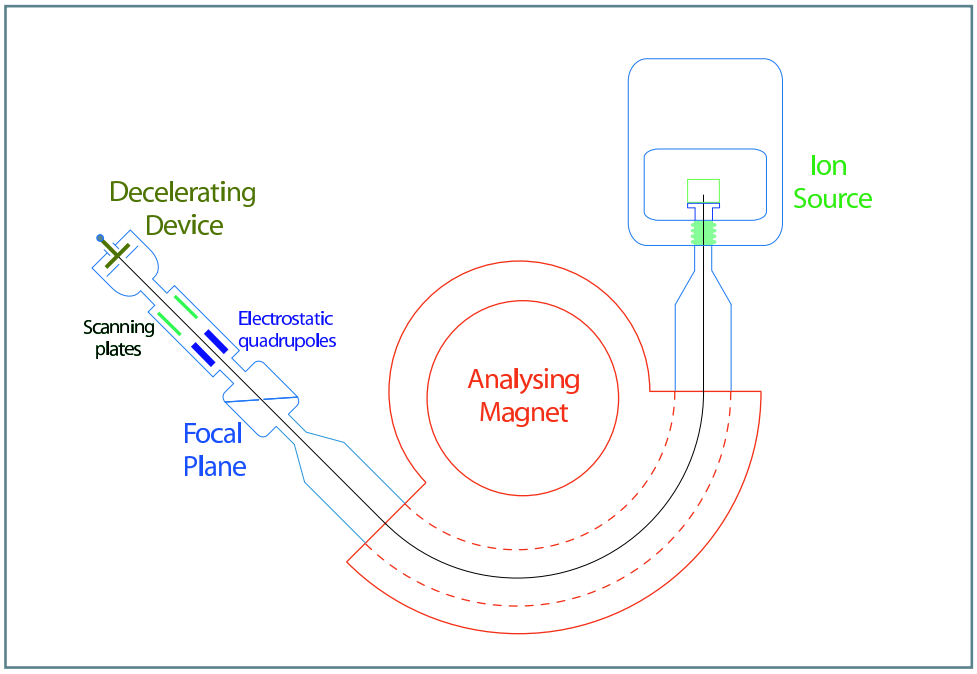

Figure 4.6: *Schematic drawing of the isotope separator SIDONIE located in CSNSM in Orsay.*

4.3 Specifications of the RFQ

Here are presented the first tests on the COLETTE transmission, and results on the emittance reduction in Orsay.

4.3.1 Transmission

First tests of deceleration

Before testing the complete setup, only the injection electrodes were mounted (see figure 4.7) with a Faraday cup 10 mm after the injection orifices. These electrodes are compound of an Einzel lens and an injection cone. Their geometry was optimized by simulations to decelerate the incoming beam with minimal transverse energy [28]. First results showed a good transmission for beams decelerated down to 50 eV [75, 76], as shown in figure 4.8. This represents the transmission as a function of the decelerating voltage applied on COLETTE. The beam energy is the difference between the incoming ion beam (30 keV) and this decelerating voltage. These results show an energy distribution of 20 eV. The energy difference of 7 eV between a focalized and a parallel beam is due to the gain in transverse energy for a focalized beam. More detailed results are given in [76].

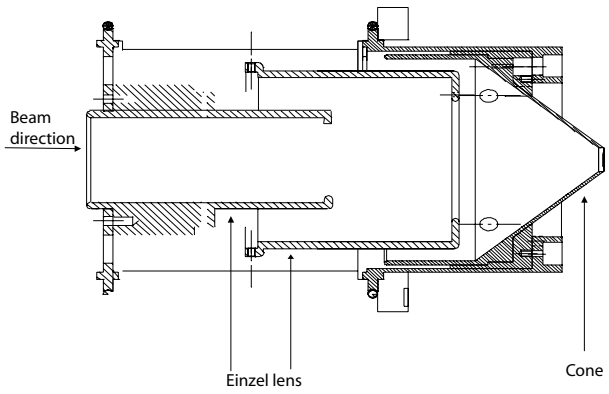

Figure 4.7: *Experimental setup of the injection electrodes, on which the first deceleration tests were performed. They are constituted of two electrodes: an Einzel lens, and a cone electrode. The Faraday cup was installed 10 mm behind the exit orifice.*

COLETTE transmission

The transmission of the COLETTE setup, as depicted in figure 4.4, was tested as a function of various parameters. The first experimental results are presented here. An optimum configuration at 20 kV was found for 1.7 MHz applied on the quadrupole with the limited pseudo-potential $D = 17.7$ eV for ^{14}N. This pseudo-potential is the maximum which can be applied. Therefore, a new RF-system was built to increase this potential, as to increase the cooling power of our setup since the trapping capacity is directly related to this pseudo-potential. Another parameter is the gas pressure inside the trap. The pressure should be high enough to interact with the gas but not too high in order not to stop the beam. The optimum flow injected into the quadrupole was found to be 0.9 mbar.l.s^{-1}.

The final transmission with this setup was measured to be 60%. The loss of transmission, compared to the 90% obtained with the deceleration electrodes (see figure 4.8), is mainly due to the limited pseudo-potential.

4.3.2 Emittance reduction

Before the installation of COLETTE at SIDONIE, the emittance was measured at the exit of SIDONIE (figure 4.9). The emittance is 65π·mm·mrad vertically and 25π·mm·mrad horizontally[2] at 20 keV. With COLETTE it is now 11π·mm·mrad vertically and horizontally 8π·mm·mrad. These results were obtained with a gas flow of 0.8 mbar.l/s, corresponding to a pressure of $10^{-}2$ mbar inside COLETTE. The gas used is helium in order to reduce the charge exchange with the ions. Figure 4.9 is the demonstration of the emittance reduction with COLETTE. All these results show a divergent beam (see figure 4.2). This beam divergence is due to the fact that the focus point after the ion beam cooling in COLETTE is localized just after the extraction electrodes. Moreover we obtain about the

[2]These results for SIDONIE are in good agreement with previous measurements at 20 keV [77], and at 40 keV [78] vertically: $> 40\pi$·mm·mrad. This is in good agreement with the energy dependence, *i.e.* inversely proportional to the square root of the energy. Horizontally, more investigations are needed to confirm previous values.

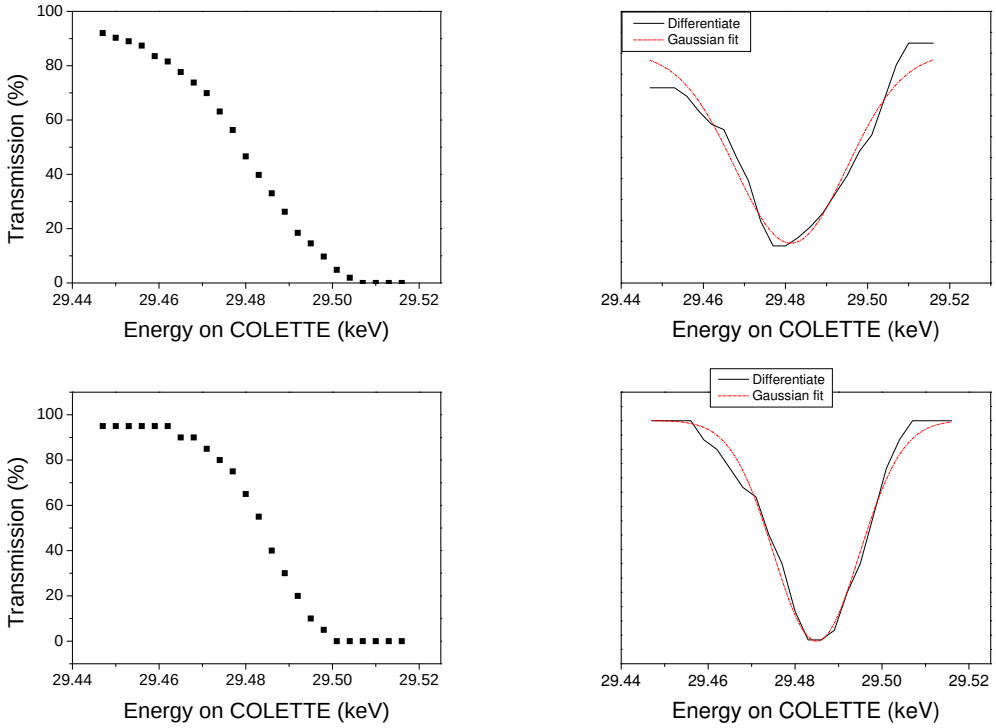

Figure 4.8: *Left: transmission as a function of the decelerating voltage. Right: the derivative and its gaussian fit. The gaussian width is defining the energy distribution. At the top, a focalized beam on the faraday cup with 27 eV width; at the bottom, a parallel beam with 20 eV width. The center shift is due to the difference in energy of the incoming beam.*

same emittance in both directions. This shows the good operation of our setup: the cooling beam is well defined in both directions. The divergence is ~ 8 mrad, and the position focus is ~ 2 mm, which is well below the exit hole of the deceleration electrode (15 mm).

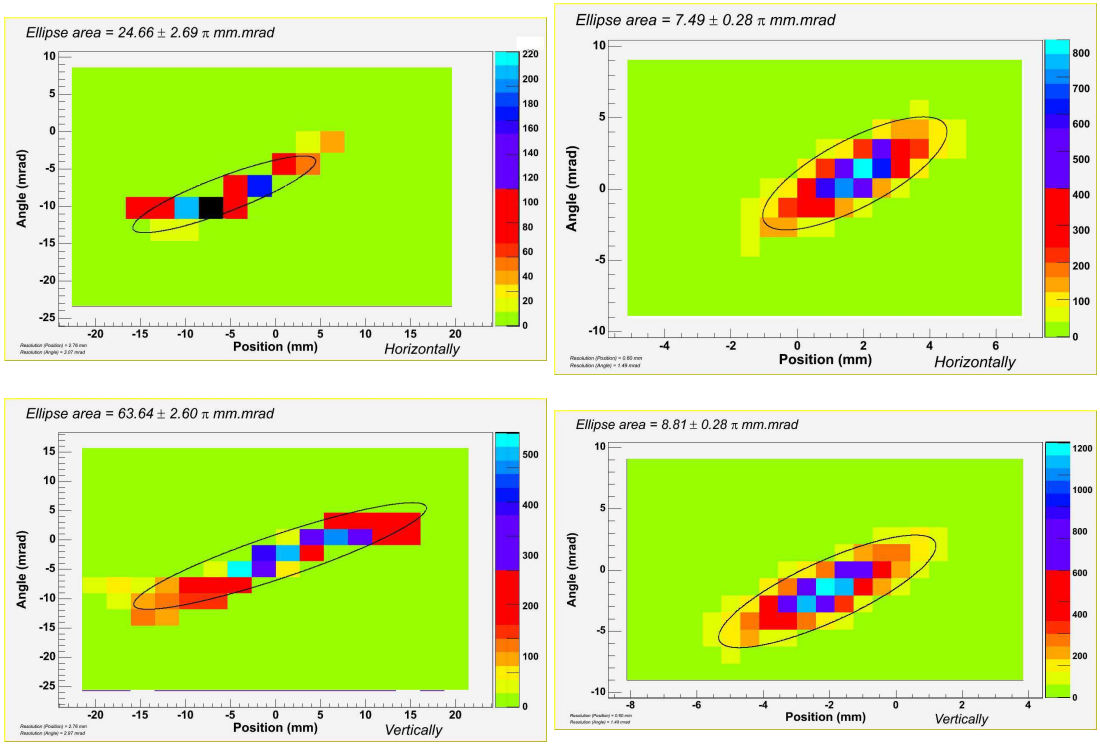

Figure 4.9: *Emittance measurement of SIDONIE (left), and behind COLETTE (right), horizontally on the upper part and vertically on the bottom. All these measurements were performed at an energy of 20 keV.*

Due to this reproducibility in both directions, we performed systematic emittance measurements as a function of the RF-amplitude and the gas flow only in the y-direction. The influence of the gas flow is presented in figure 4.10, for a gas flow between 0 and 1.2 mbar.l/s, at 20 keV. These results show that the emittance is decreasing and the number of ions is increasing for a higher gas flow. Studies at a gas flow higher than 1.2 mbar.l/s showed an increase of the ion beam loss, and indicated that the pumping system was not sufficient at so large gas flows.

Figure 4.11 is an illustration of the evolution of the emittance for three different values of the pseudo-potential D (see eq. (2.17)), depending on a variation of the RF-amplitude. The measurements were performed at 20 keV with a gas flow of 0.9 mbar.l/s. All these results show that by decreasing the pseudo-potential, we decrease the power of trapping, so we lose the ions. With the applied RF-amplitude divided by only two, the pseudo-potential is decreased by more than a factor 3 and the emittance increased by the same factor 3. This demonstrates the utility of the new RF-system which can increase the amplitude, and so reduce further the emittance. Another solution will be to reduce r_0 (See eq.(2.17)), this, first, would be more difficult technically, and would mean an ion beam loss for ions entering with large divergence. Figure 4.12 presents the phase space density $\frac{N}{\varepsilon}$, with N the number of ions counted in the ellipse representing the emittance. It shows

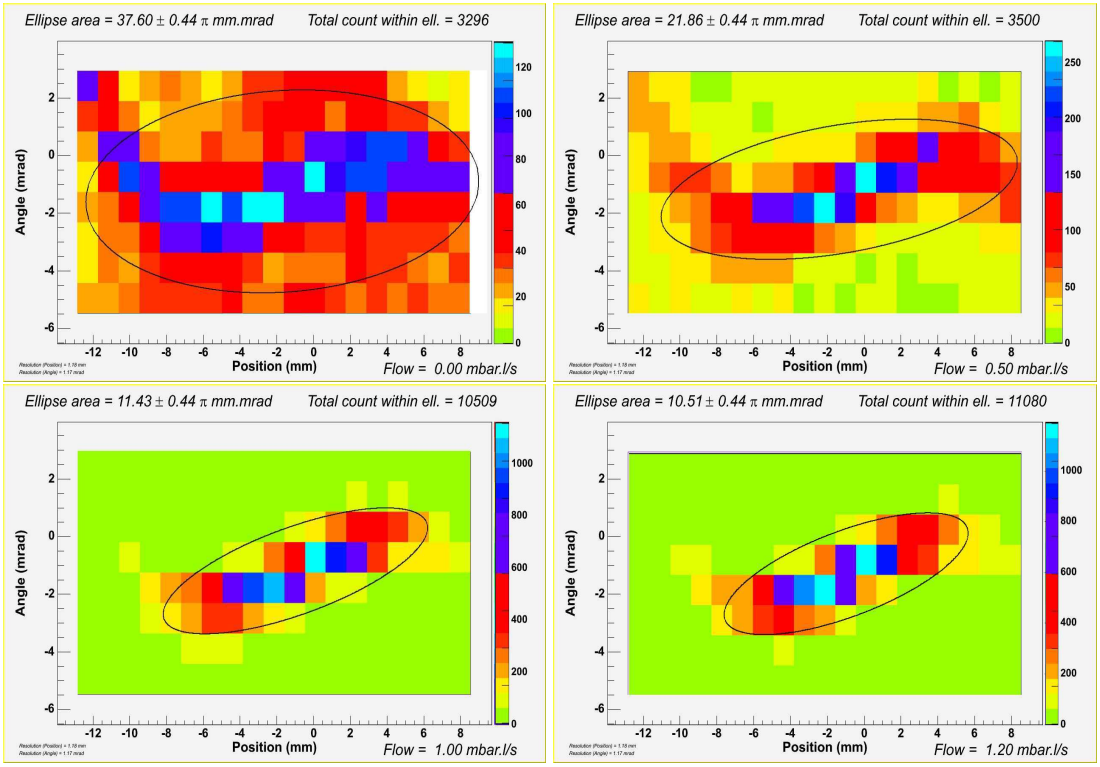

Figure 4.10: *Influence of the gas flow inside the quadrupole at 20 keV. On the top left the gas flow was equal to zero, on the top right a gas flow of 0.5 mbar.l/s was applied, on the bottom left 1.00 mbar.l/s and 1.2 mbar.l/s on the bottom right.*

that the phase space density increases with the pseudo-potential. The new RF-system is needed to reach a higher phase space density value, and to reach an eventual saturation point.

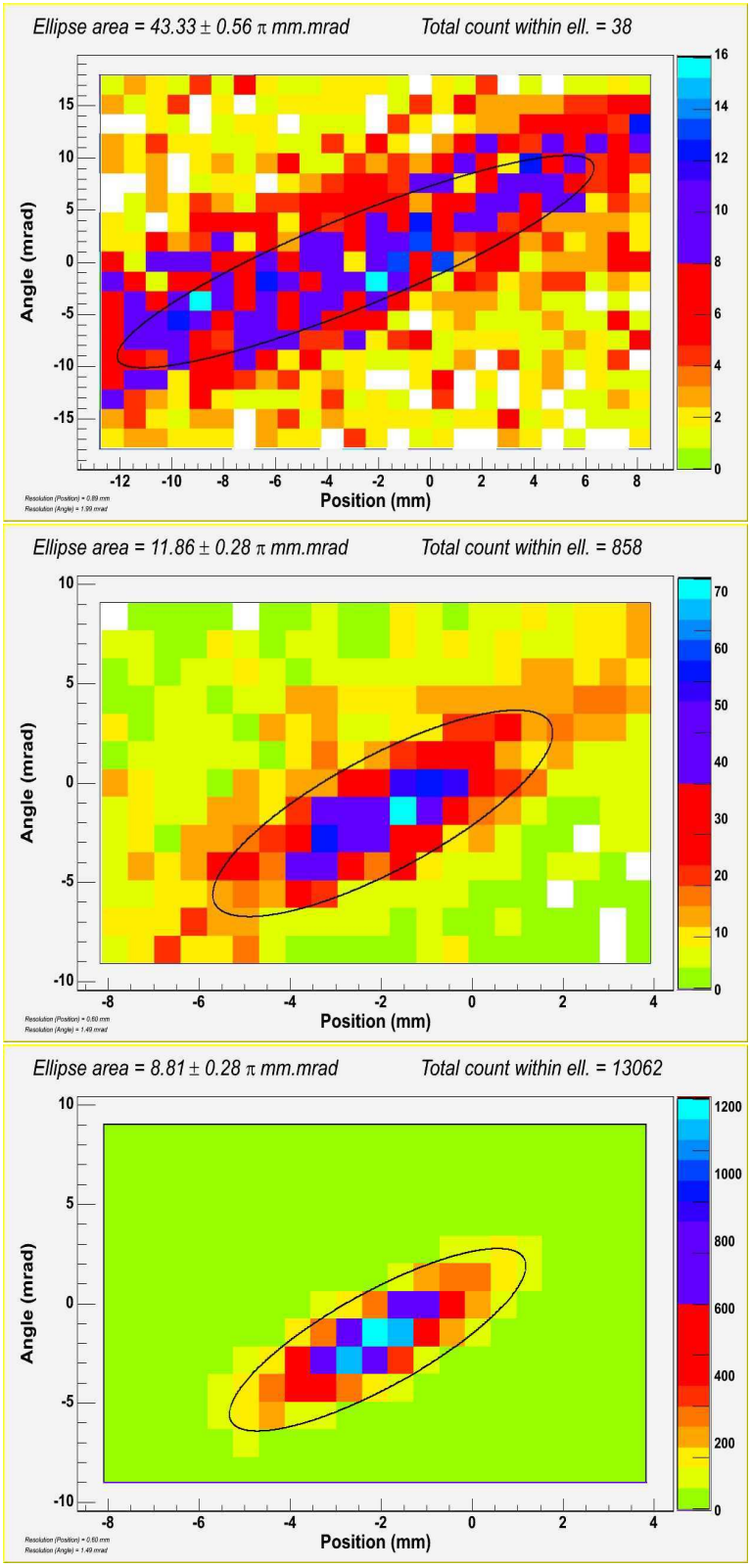

Figure 4.11: *Influence of the RF-amplitude applied on the quadrupole at 20 keV. The figure on the top corresponds to a pseudo-potential (eq. (2.17)) $D = 4.4\,eV$, $D = 11\,eV$ in the middle, and the one on the bottom corresponds to $D = 17.7\,eV$, which is the maximum we can reach with the present setup.*

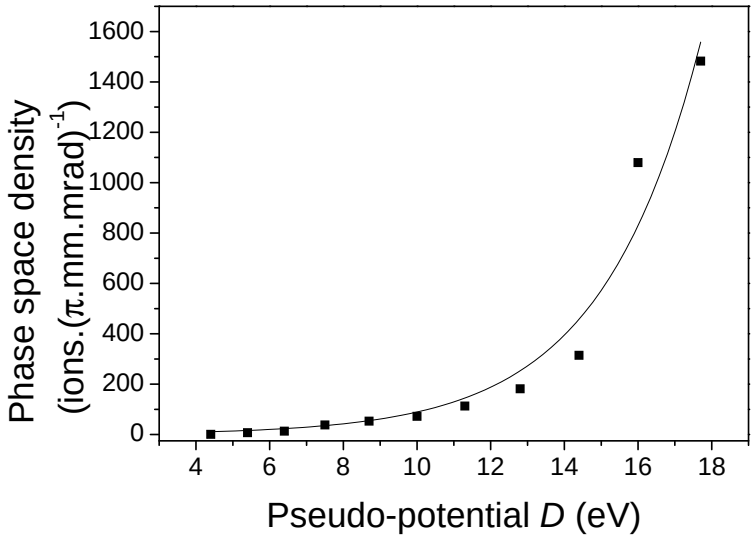

Figure 4.12: *Phase space density as a function of the pseudo-potential D (eq. (2.17)). An exponential fit is applied to the experimental points.*

COLETTE is now installed at CERN on the MISTRAL beam line (figure 4.13).

Figure 4.13: *Picture of the COLETTE setup at ISOLDE just before the MISTRAL setup.*

Chapter 5

Optimization of ISOLTRAP

To do a high-precision measurement, a homogeneous magnetic field and a quadrupole electric field are required in the precision trap, in order to trap all ions under the same conditions irrespective of their position. If not, the cyclotron frequency measurement would depend on the position, especially along the axial direction z*, introducing systematic errors. The optimization described in the following is used to ensure this axial homogeneity.*

5.1 Deviation from an ideal Penning trap

A real Penning trap deviates in many aspects from an ideal Penning trap, here are presented some differences, and their consequences on the electric and the magnetic fields inside the trap.

In Penning traps systematic errors arise from misalignment, temporal fluctuations of the magnetic field, and magnetic and electric field imperfections since ion motion in Penning traps is controlled by magnetic and electric fields. The misalignment was minimized during the installation.

An ideal Penning trap can be defined as the superposition of a homogeneous magnetic field B and an electrostatic quadrupole field $V(\rho, z)$ coaxial to the magnetic field as explained in Chapter 2. The combination of these particular fields allows a charged particle to be stored in a well-defined volume. Also, there is an exact solution of the particle's equations of motion (eq. 2.24).

The largest source of uncertainty are electric and magnetic field inhomogeneities causing a broadening and a shift of the cyclotron frequency resonance. These inhomogeneities are caused by the fact that a real Penning trap deviates from the ideal case in many aspects [58, 35]. In the following only two of them will be discussed, concerning the electric and the magnetic field.

5.1.1 Electric field

Electric field inhomogeneities arise from geometrical imperfections of the trap construction such as holes in the endcaps for injection or ejection of ions or from the unavoidable truncation of the electrodes. They lead to deviations from a pure quadrupole field. The

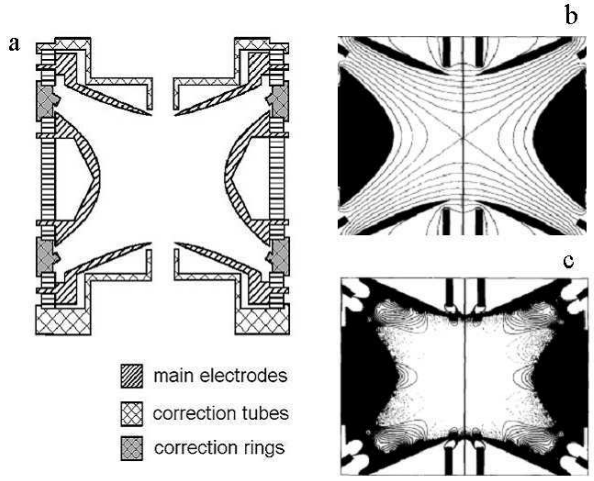

Figure 5.1: *In (a), a section of the high-precision Penning trap is shown. It consists of a four-fold segmented ring electrode, two endcaps, two correction tubes for the holes in the endcaps and two correction rings. (b) Equipotential lines for a compensated trap as shown in (a) with 1.0 V on the ring electrode, 9.5 V on the endcaps, 5 V on the correction rings and 12.2 V on the correction tubes. (c) Residual electric potential ΔV after the subtraction of a pure quadrupole field. Only equipotential lines in the range of $|\Delta U/U_0| < 5 \cdot 10^{-4}$ are shown. (b) and (c) are taken from Refs. [58, 80].*

quadrupolar field inside the trap is required to precisely control the ion motion and to get the exact condition $\omega_c = \omega_+ + \omega_-$.

In a real Penning trap, the solution of Laplace's equation is defined by [36]:

$$\begin{aligned} V(\rho,z) &= \frac{1}{2}V_0\left[\frac{C_2}{d^2}\left(z^2-\frac{1}{2}\rho^2\right)+\frac{C_4}{d^4}\left(z^4-3z^2\rho^2+\frac{3}{8}\rho^4\right)\right. \\ &+ \left.\frac{C_6}{d_6}\left(z^6-\frac{15}{2}z^4\rho^2+\frac{45}{8}z^2\rho^4-\frac{5}{16}\rho^6\right)+\ldots\right]. \end{aligned} \tag{5.1}$$

with C_2 the quadrupole component. The frequency shift $\Delta\omega_c^{elec}$ [79, 58] due to the octupole (represented by C_4) and dodecapole (C_6) contributions, depends on the motion amplitudes: a_+, a_-, a_z respectively of the cyclotron, the magnetron and the axial motion, and is given by

$$\Delta\omega_c^{elec} = \frac{V_0}{2d^2B}\left[\frac{3}{2}\frac{C_4}{d^2}(a_-^2-a_+^2)+\frac{15}{4}\frac{C_6}{d^4}\left(a_z^2(a_-^2-a_+^2)-(a_-^4-a_+^4)\right)\right]. \tag{5.2}$$

To correct for the imperfections correction electrodes are implemented in the precision Penning trap: two rings and two correction tubes as shown in figure 5.1(a), *i.e.* to eliminate C_4 and C_6. Figure 5.1(b) shows the equipotential lines obtained including these correction elements. Figure 5.1(c) shows the remaining deviation from a pure quadrupole field: they are far away from the ion path, since typically the axial motion amplitude does not exceed 1 mm. The theoretical influence of the correction elements on the components

of the field (see eq. (5.1)) is shown in Table 5.1.

Electric field optimization therefore consists of varying the correction rings and correction tubes voltages and monitoring the effect on the cyclotron frequency. This will be explained in more detail in the next section.

Table 5.1: *Multipole contributions of the potential: without and with the compensation electrodes in the ISOLTRAP hyperbolical Penning trap [81]. In the case of the correction elements, the influence on C_2 component is indicated.*

	C_2	C_4	C_6
Without correction electrodes	0.96	0.23	-0.26
	Influence on C_2	C_4 value	C_6 value
Correction ring electrode	$1.55 \cdot 10^{-5}$	$-5.50 \cdot 10^{-4}$	$1.47 \cdot 10^{-4}$
Correction tube electrode	$5.42 \cdot 10^{-3}$	$5.60 \cdot 10^{-3}$	$9.02 \cdot 10^{-3}$

5.1.2 Magnetic field

To do a high-precision cyclotron-frequency measurement, an excellent homogeneity and temporal stability of the magnetic field are required. Here we address the possibility to minimize magnetic field inhomogeneities by a special optimization procedure. The temporal stability is discussed in [82].

Magnetic field imperfections are arising from the homogeneity limits of commercial superconducting magnets: nowadays they can provide a homogeneity of typically $\Delta B/B < 10^{-8}$ over a volume of 1 cm^3. This volume is smaller than the entire volume of the trap ($3-4$ cm^3). In addition, the magnetic field homogeneity can be disturbed if materials with a magnetic susceptibility are introduced into the magnetic field. Such material can be the components of the trap itself. To avoid as much as possible this problem, the ISOLTRAP electrodes are made from oxygen-free copper. Like in the E-field case there are magnetic components of higher order that must be minimized but only even components occur due to rotational symmetry. The frequency shift [35] due to the inhomogeneities can be approximated by

$$\Delta\omega_c^{magn} \approx \beta_2 \omega_c (a_z^2 - a_-^2), \tag{5.3}$$

where β_2 denotes the relative strength of the lowest-order component of magnetic inhomogeneities.

The precision Penning trap (see figure 3.3) is placed in a 5.9 T magnetic field generated by a superconducting solenoid. To provide a homogeneous magnetic field the magnet is provided with a set of superconducting shim coils and a set of room-temperature shim coils (see figure 5.2). The current on all shim coils was optimized before the first use of the trap. For practical use, only the room-temperature shim coils can be optimized when the magnet is charged. The three coils closest to the trap (dashed boxes in figure 5.2) have the strongest influence on the field distribution and thus on the field homogeneity inside the

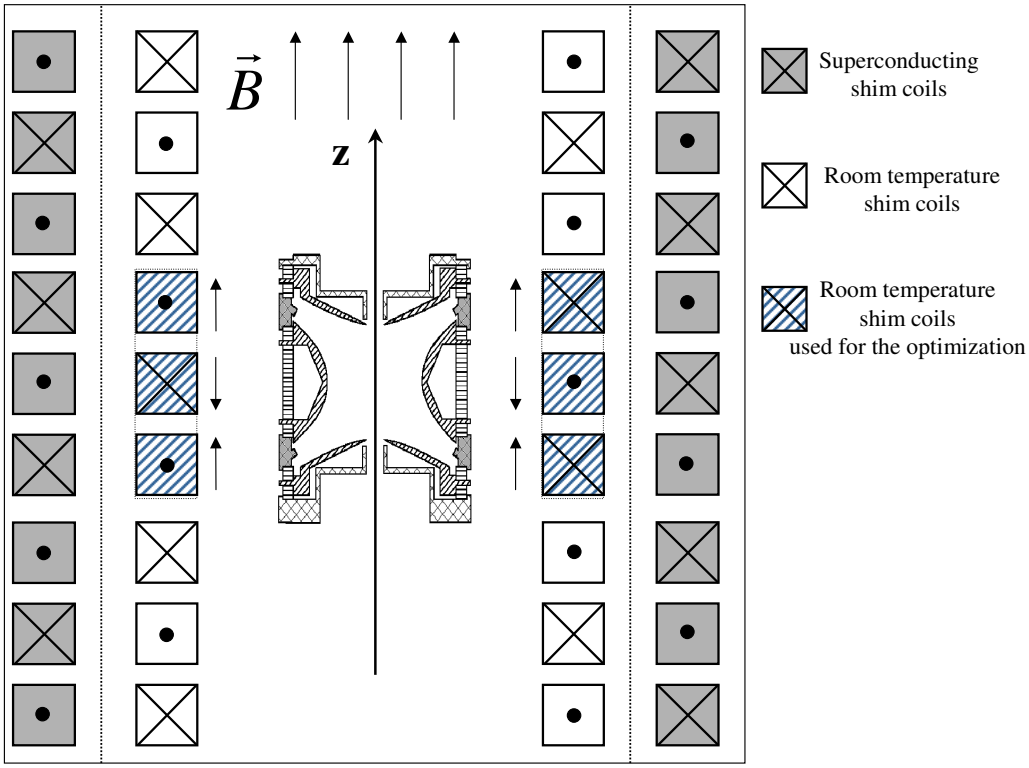

Figure 5.2: *A section of the measurement trap, which is installed in a superconducting magnet which generates a magnetic field B in the axial direction. Several superconducting shim coils and room-temperature shim coils are shown. The correction for magnetic field inhomogeneities is done on the latter. Points and crosses represent the current direction out of and into the plane respectively.*

trap. Consequently, the optimization parameter is the current I_S applied simultaneously to these three room-temperature shim coils. This current induces a magnetic field oriented in one direction for the two outer coils and in the opposite direction for the inner one (see figure 5.2).

5.2 The key of the optimization: the capture timing

A parameter is used to probe the trap in order to perform an optimization of the fields: it is the capture timing.

Despite some axial cooling in the first Penning trap, ions coming into the precision trap do not have exactly the same axial energy so they are not trapped at the same initial position in the trap. Therefore, a homogeneous magnetic field and a quadratic electric field are required in the precision trap, in order to trap the ions under the same conditions irrespective their exact initial position trapping.

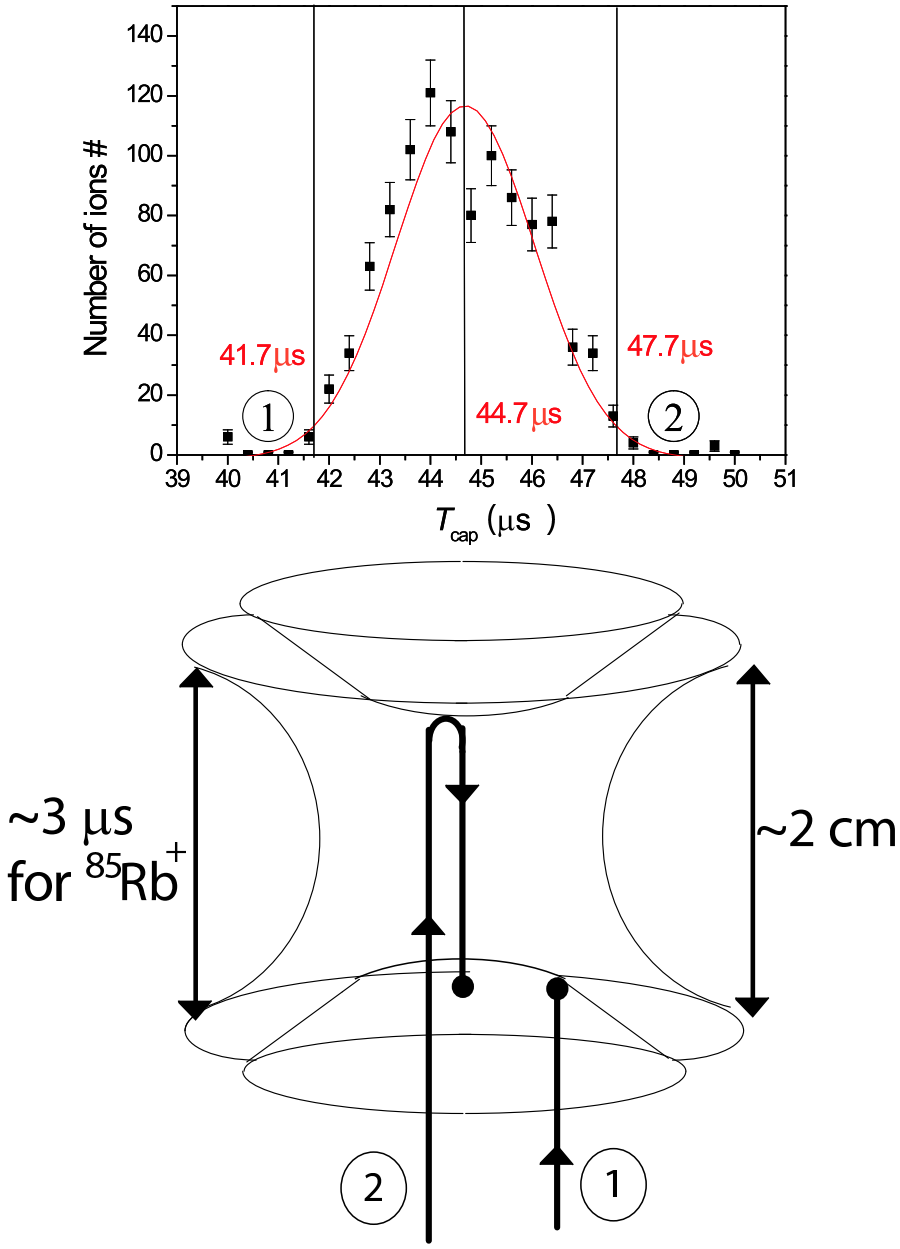

Figure 5.3: *Top: Number of captured ions as a function of the capture timing for $^{85}Rb^{+}$. The solid line is a Gaussian fit to the data points. The FWHM of the fit is 3.5 μs. Bottom: Schematic drawing of the high-precision Penning trap: (1) The capture timing is too short: i.e. the ions can not get captured since the trapping potential at the lower endcap is not yet lowered. (2) The capture timing is too long, ions already left the trap before switching up the potential.*

If not, the cyclotron frequency depends on the position of ions, especially along the axial direction z[1]. To study this phenomenon, the capture timing (T_{cap}) defined as the time between the ejection from the lower trap and capturing in the precision trap (see figure 3.3) is used. The injection and ejection are controlled by using potential applied on the two

[1]This problem is avoided in the first trap by ion cooling.

end-caps[2]. Depending on their axial energy ions have different capture times, as shown in figure 5.3 for $^{85}Rb^{+}$. With a T_{cap} too long or too short, ions are lost (it corresponds here to a variation of 6 μs of the capture timing). So the capture timing allows to probe the entire trap region from the time when an ion enters the trap (1), its transit to the upper endcap, its reflection from this endcap, plus the return journey (2).

5.3 Optimization of the magnetic field

In order to control the magnetic field inside the trap superconducting and room temperature shims coils are installed. The superconducting shim coils cannot be optimized when the magnet is charged. The three temperature shim coils closest to the trap are used for the optimization.

The optimization parameter is the current I_S applied to the three room-temperature shim coils close to the trap (see figure 5.2). The optimum value of the shim-coil current will make the magnetic field constant over the trapping volume, hence minimizing frequency variations for all capture timings between 41.7 μs (1) and 47.7 μs (2) for $^{85}Rb^{+}$ (see figure 5.3). The difference between these two values corresponds to the travel time of the ions in the trap in both directions: first from the entrance of the trap to the top and then from the top to the entrance. To probe the magnetic field, the cyclotron frequency is determined, since it is directly related to the magnetic field (see eq. (1.6))[3]. This determination of the cyclotron frequency is done as explained in section 3.2.2 and in figure 3.6. So for each value of T_{cap}, a full TOF resonance curve was performed.

The importance of such an optimization is shown in figure 5.4, which gives the cyclotron frequency as a function of the capture timing for two extreme values of the shim-coil current. The corresponding relative frequency deviation for $\Delta T_{cap} = \pm 2.5 \mu$s for each current setting is $\frac{\Delta \nu_c}{\nu_c} = 4 \cdot 10^{-7}$. Note that there is a shift in absolute frequency as well as an inflection in the frequency variations.

To find the optimum value for T_{cap}, *i.e.* where $\Delta \nu_c = 0$, the shim-coil current is varied, and the frequency shift $\Delta \nu_c$ between two different capture timings marked as (3) ($T_{cap} = 44.7\ \mu$s) and (4) ($T_{cap} = 47.2\ \mu$s) in figure 5.4 is measured. These timings correspond to half of a capture timing scan, *i.e.* the travel of the ions in only one direction (here from the top of the trap to the entrance)[4]. The frequency variation was measured for several shim coil currents and the results are plotted in figure 5.5. The optimum value was obtained from a linear fit to the data points, yielding $I_S = 270$ mA.

Results obtained with this optimum value are presented in figure 5.6. The relative deviation is well below $5 \cdot 10^{-8}$ within the normal capture time variation of $\pm$ 1.5 μs. Figure 5.6 also nicely illustrates the overall behavior of the cyclotron frequency as a function of field homogeneity and inhomogeneity with the frequency shifts and broadening. These two effects lead to systematic errors so the field optimization is very important.

[2] Ions arrive in the precision trap with an energy of few eV.

[3] The correction for the magnetic field drift phenomenon is explained in Appendix A.

[4] 47.7 μs was not used because of the lack of statistics at this point. Moreover it is expected that during a "normal" measurement this region is never reached by the ions, so it is not necessary to make the entire trap homogeneous.

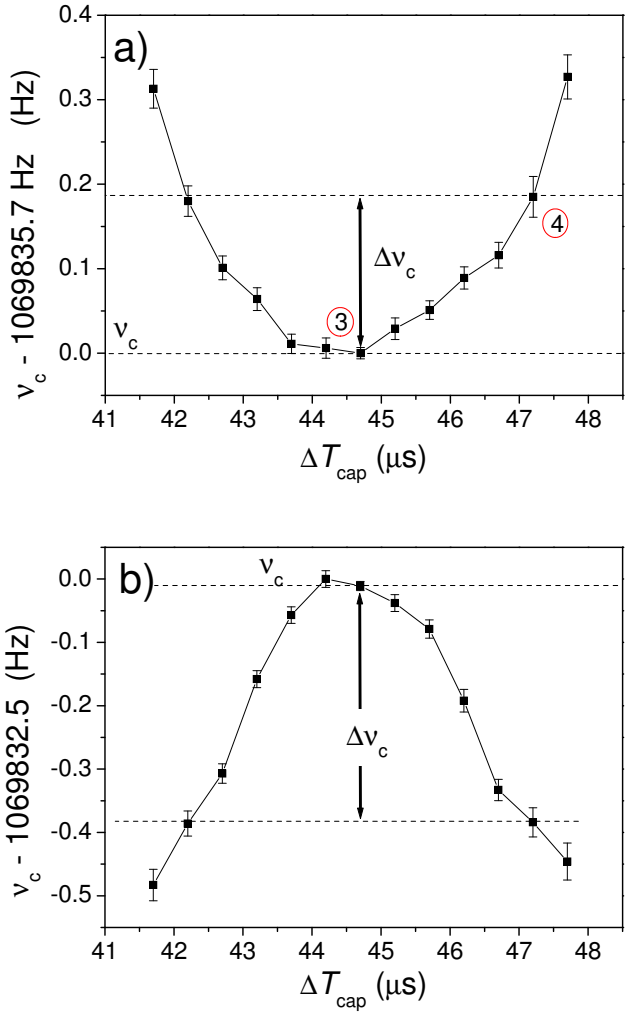

Figure 5.4: *The cyclotron frequency ν_c as a function of the capture timing T_{cap} for two different shim-coil currents: (a) $I_S = 350\,mA$ and (b) $I_S = 100\,mA$.*

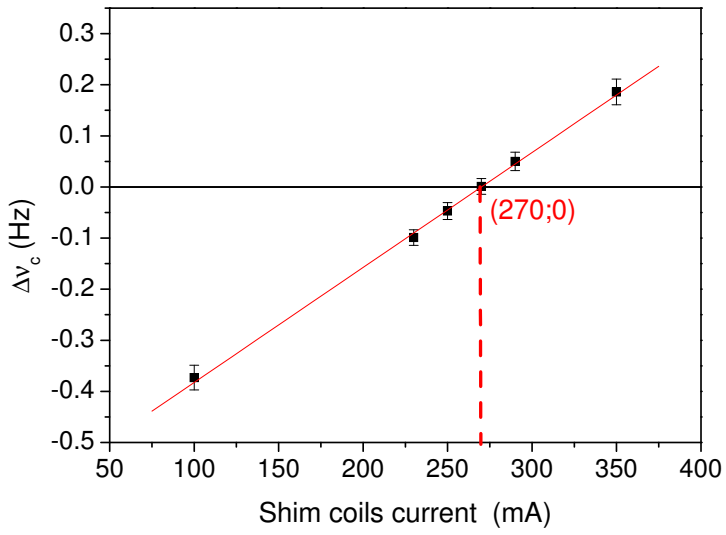

Figure 5.5: *Cyclotron frequency difference $\Delta\nu_c$ between two capture timings (T_{cap} = 44.7 μs and 47.2 μs) as a function of the shim-coil current. The linear fit to the data points provides the optimal value: where $\Delta\nu_c = 0$, $I_S = 270\,mA$.*

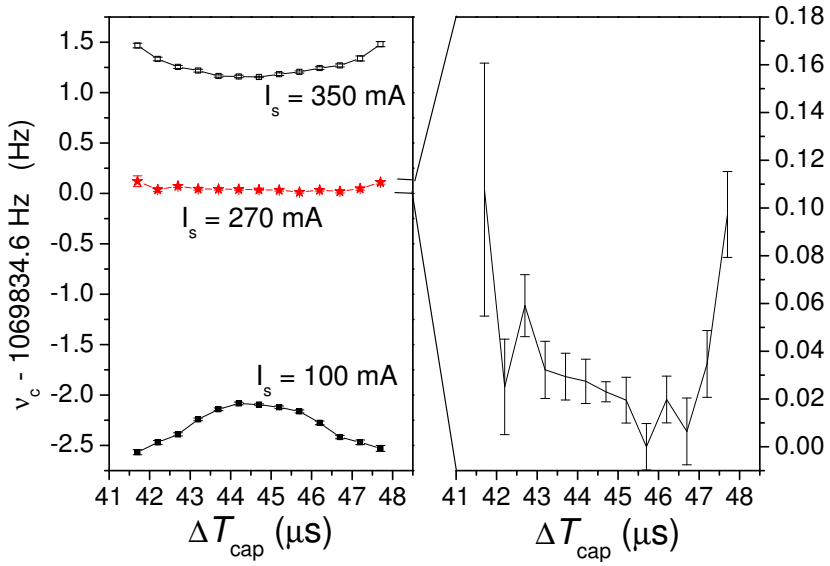

Figure 5.6: *Left: The deviation of the cyclotron frequency as a function of the variation of T_{cap} for two extreme values of the shim-coil current (open boxes: $I_S = 350\,mA$; full boxes: $I_S = 100\,mA$) and for the interpolated optimum value $I_S = 270\,mA$ (stars). Right: Zoom on the cyclotron frequency for the optimum shim-coil current of $I_S = 270\,mA$. The relative variation $\frac{\Delta\nu_c}{\nu_c}$ is about $5 \cdot 10^{-8}$ for $\Delta T_{cap} = \pm 1.5 \mu s$ which is an excellent setting for the trapping volume.*

5.4 Optimization of the electric field

To correct for the electric field imperfections two correction rings and tubes can be used, as shown in figure 5.1. The correction rings are used to correct for the non-infinity of the electrodes, the correction tubes for the discontinuity in the endcaps coming from the ions' entrance and exit holes. The influence of the rings is far much smaller than the influence of the tubes (see Table 5.1 and section 5.4.2).

5.4.1 Correction tubes

The two correction tubes are named "Lower Correction Tube" (LCT), and "Upper Correction Tube" (UCT). The voltage applied to these two tubes is identical. This voltage is the optimization parameter for the electric field adjustment. Again the capture timing is used to probe the effects of the changing field on the cyclotron frequency.

The optimum value of the correction tube voltage is found when a constant electric field is realized in the trap for all capture timings between 41.7 μs and 47.7 μs (see figure 5.3). To probe the electric field, the reduced cyclotron frequency ν_+ is used (eq. (2.26)). The magnetic field optimization was done first to ensure that B and ν_c are constant along the axial direction of the trap. Consequently the variation of ν_+ is directly related to the electric field via V_0. This explains why we choose ν_c (directly related to B and not to V_0) for the magnetic field and ν_+ (related to V_0) for the electric field. The approximation $\nu_+ = \nu_c - \frac{V_0}{4\pi B d^2}$ can be made[5], where V_0 is the trapping voltage, B the magnetic field magnitude, and d a parameter for the trap dimension ($2d^2 = \rho_0^2$).

Figure 5.7(b) presents a measurement of the reduced cyclotron frequency as a function of the capture timing for two extreme values of the correction-tube voltage. The deviation $\frac{\Delta\nu}{\nu}$ is about $1.5 \cdot 10^{-6}$ for both voltages, which shows the importance of the electric field optimization. To determine the optimum value, the frequency difference $\Delta\nu_+$ between two different capture timings (T_{cap} = 44.7 μs and T_{cap} = 47.2 μs) is measured as a function of the correction-tube voltage. The results are plotted in figure 5.7(a). The optimum value with a minimal frequency shift $\Delta\nu_+$ was found to be 1.120 V by interpolation. Results with this optimum value are presented in figure 5.7(b). Again frequency shifts and broadening are seen. The deviation $\Delta\nu_+$ is minimized to about $5 \cdot 10^{-8}$. The remaining deviations may be due to temperature fluctuations in the ISOLDE hall. Further investigation is needed.

5.4.2 Correction rings

Figure 5.8 shows a comparison of the influence of the correction rings and the correction tubes. For this the optimal value for the voltage applied to the correction rings and to the correction tubes (*i.e.* to obtain a flat dependence as a function of T_{cap}) was used and also two extremes values, chosen in the same proportion for the rings and the tubes. For measurements of the influence of the correction rings the optimum value was set on the correction tubes (1.12 V). During measurement of the influence of the correction tubes, the optimum value was set on the correction rings (6.80 V).

[5] The demonstration can be found in Appendix A.1.

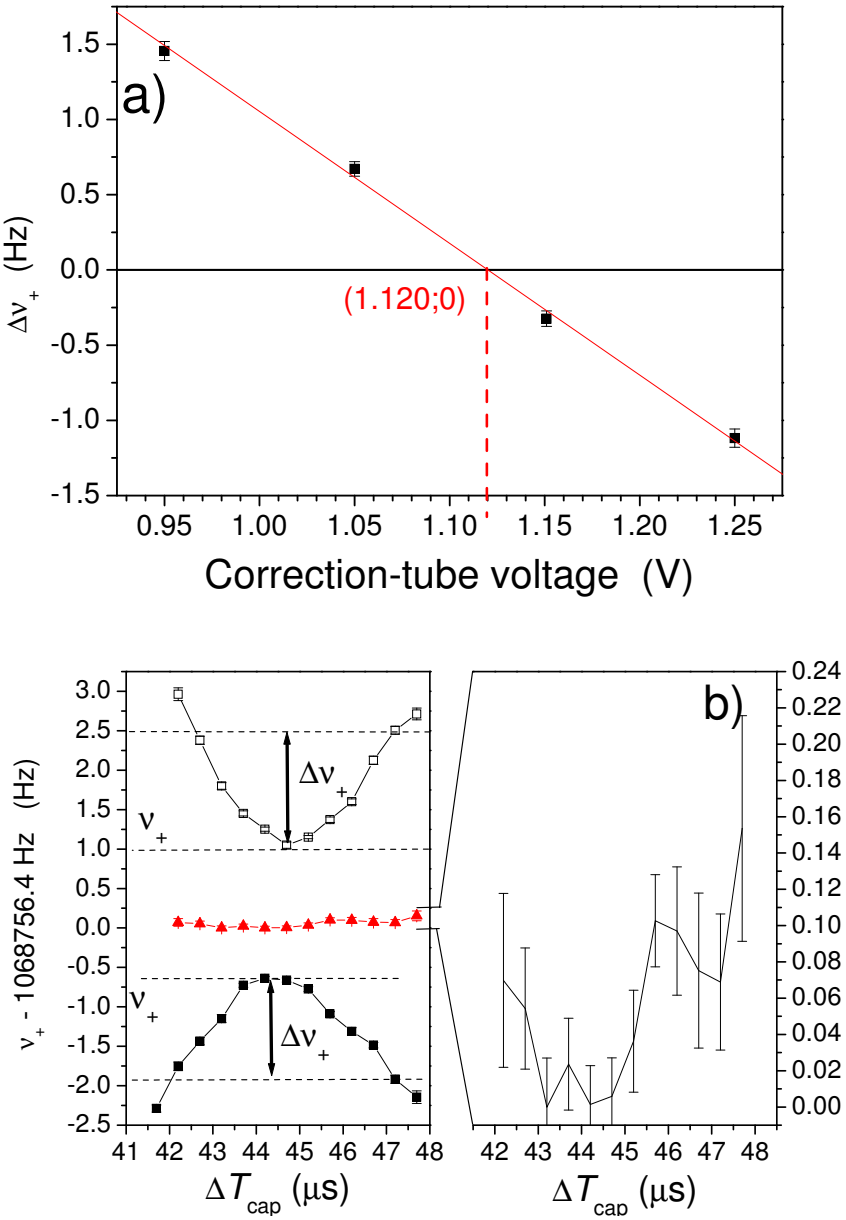

Figure 5.7: *(a) Frequency shift between two capture timings (T_{cap} = 44.7 μs and 47.2 μs) as a function of the correction tubes voltage. The linear extrapolation provides the optimal value: 1.120 V for $\Delta\nu_+ = 0$. (b) Reduced cyclotron frequency as a function of the variation of the capture timing for two different bad values of the correction tubes voltage (0.950 V for the empty boxes, and 1.250V for the solid boxes), and for the optimum value 1.120 V, represented by triangles. The zoom shows the frequency shift for the optimum value of the correction tubes voltage.*

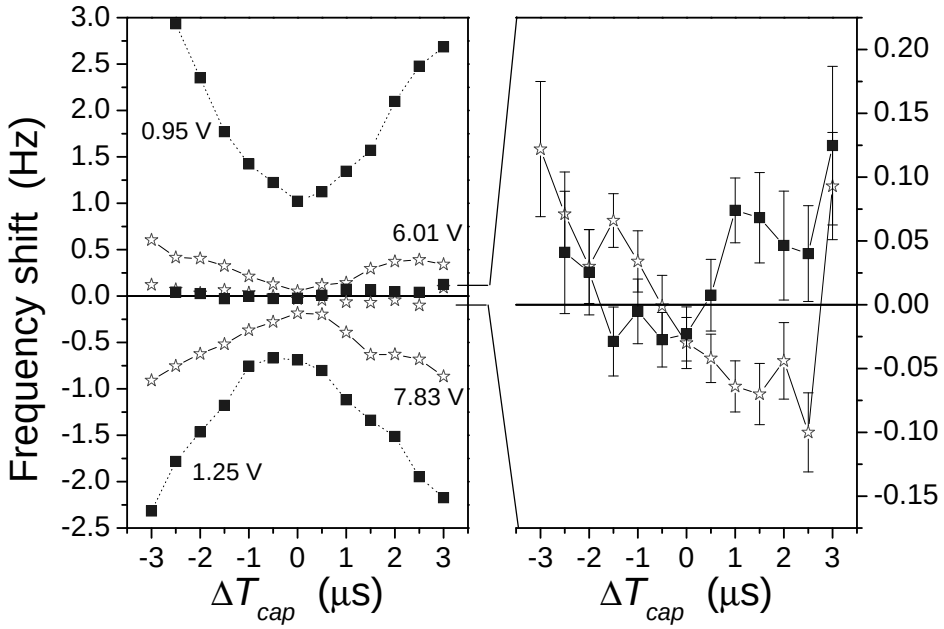

Figure 5.8: *Variation of the reduced cyclotron frequency as a function of the variation of the capture timing for different values of the voltages on the correction rings (empty stars) and tubes (filled squares) (results presented in figure 5.7). Rings voltages: 6.01 V, 6.80 V, and 7.83 V,; tubes voltages: 0.95 V, 1.12 V, and 1.25 V.*

The influence of the correction rings is about five times less than for the tubes, so the optimization should be done essentially on the tubes. This was expected from the calculations (see Table 5.1) showing a stronger influence of the tubes. The difference between the behavior observed in other systems [83] and our result is due to the fact that the axial motion of the ions is not cooled in ISOLTRAP's precision trap. So the ions have larger axial amplitudes and come closer to the holes in the endcaps and thus are influenced by the correction tubes.

5.5 Results on mass measurements

A measurement of a well known mass ^{41}K was performed with the ISOLTRAP setup in order to determine the influence of the optimization.

To check the influence of our optimization, a measurement of the very well known ^{41}K mass was performed before and after the optimization of the electric and magnetic fields. The mass value of ^{41}K was compared to the one given in the AME03 table [3]. The mass excess value extracted from the measurements before and after performing the optimization procedure are shown in figure 5.9. A clear shift in the mass value of almost one keV was observed. After the optimization the mass excess value of ^{41}K agrees well within the error bars with the AME value: -35559.07 ± 0.19 keV. The deviation was around $5 \cdot 10^{-7}$ on the mass value, it is now below $2.5 \cdot 10^{-8}$. We get the same precision

but we are more accurate.

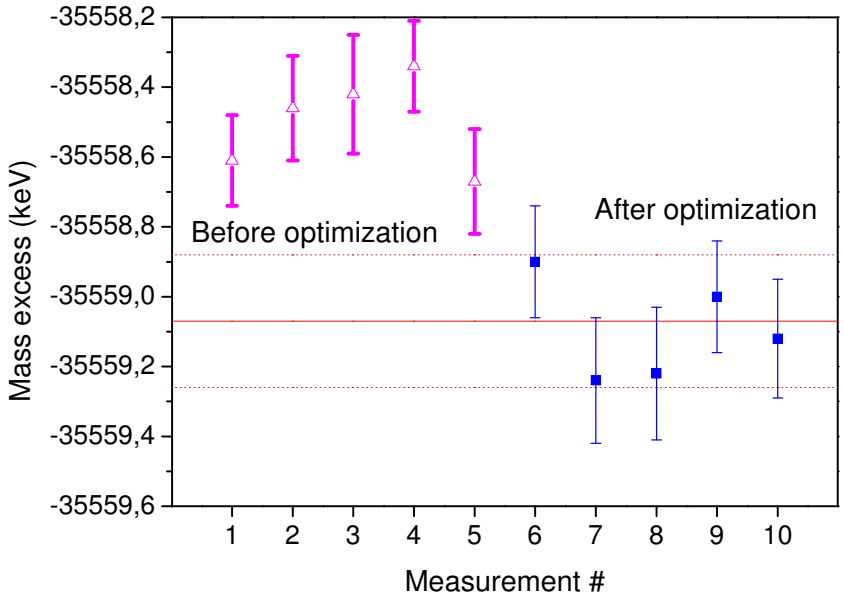

Figure 5.9: *Mass excess measurements of ^{41}K with ^{39}K as reference before and after the E/B optimization. Each measurement was done with limited statistics. The solid line represents the AME2003 value [3], the dashed lines give the error bars of the AME03 value.*

Part III

New high-precision mass results with ISOLTRAP

In the course of preparing ISOLTRAP for experiments on exotic nuclides several preliminary measurements have been performed, many of these measurements allowed to improve existing mass values. Measurements on exotic nuclides were performed to study magic numbers: $^{56-57}$Cr for $N = 32$ and more than thirty nuclides of nickel, copper, and gallium have been investigated at ISOLTRAP around $N = 40$.

They were produced at ISOLDE with a yield of $10^5 - 10^9$ ions/s by bombarding an uranium-carbide (UC) target and a ZrO target with 1.4 GeV protons from CERN's Proton Synchroton Booster. The ionization was done either with a W surface ionization ion source or with the resonance ionization laser ion-source (RILIS) [84]. The target-ion-source combinations used for the different nuclides are given in Table 5.2. Both targets were bombarded with proton pulses containing up to $3 \cdot 10^{13}$ protons. ISOLDE's General Purpose Separator (GPS) and High Resolution Separator (HRS) were respectively used with each target (see Table 5.2).

Chapter 6 presents results obtained with the preparation beams $^{56-57}$Mn, ^{82}Rb^m, ^{92}Sr, ^{124,127}Cs and ^{130}Ba and their influence on the so-called "backbone" of well-known masses along the nuclear chart. Chapter 7 presents results on $^{56-57}$Cr and studies on the $N = 32$ shell closure. Chapter 8 presents mass measurements on Ni, Cu, and Ga and discussions about the $N = 40$ "magicity".

Table 5.2: *Target ion-source combination used for the different nuclides.*

Element	Yield range	Target	Ion source	Separator
$^{56-57}$Mn, ^{82}Rb^m, ^{92}Sr, ^{124,127}Cs, ^{130}Ba		UC	RILIS	GPS
$^{56-57}$Cr	$10^5 - 10^9$	UC	RILIS	GPS
$^{57-69}$Ni	$10^5 - 10^9$	UC	RILIS	GPS
$^{65-76}$Cu	$10^5 - 10^6$	UC	RILIS	GPS
$^{68-78}$Ga	$10^6 - 10^8$	UC	RILIS	GPS
$^{63-65}$Ga	$10^6 - 10^8$	ZrO	W-tube	HRS

Chapter 6

Extending the mass backbone

A backbone of well-known nuclides is distinguished in the AME table. ISOLTRAP mass measurements on several nuclides bring new nuclides to this backbone.

The Atomic-Mass Evaluation AME [85] is a table of atomic masses which results from an evaluation of all available experimental data on mass measurements including direct measurements as well as decay and reaction energies. AME forms a linked network, using a least-squares adjustment of all values for the atomic masses. The evaluation takes into account all measurements and achieved accuracy to produce a relevant mass table. The new measurement value can replace all the old ones and become the only one used, or the new one can be combined with old values to decrease the uncertainty. Indeed, all the measurements with an uncertainty three times higher than the most precise value are not taken into account into the calculations used to build the table. Their influence on the mass value would be negligible, and they would increase the calculation time. The influence of each measurement on the mass value depends on their uncertainty. For example, for two measurements a and b with δa and δb as uncertainties, the coefficient used to determine the influence of each measurement is $\frac{\delta b^2}{\delta b^2+\delta a^2}$ for the mass a and $\frac{\delta a^2}{\delta b^2+\delta a^2}$ for the mass b.

In this Atomic-Mass Evaluation, a backbone of very well-known nuclides is distinguished, mainly consisting of stable nuclides. For these nuclides the atomic-mass values are known with exceptionally high precision *i.e.* most of the time below 1 keV. Figure 6.2 presents the nuclear chart. In this figure, nuclides are distinguished from the accuracy on their mass value. Nuclides constituting the backbone are those with a mass accuracy corresponding to the three lower accuracy in this figure *i.e.* below 4 keV. They represent 500 nuclides over the 3200 displayed on this nuclear chart. The precision now achieved with Penning traps allows to extend this backbone and to include also masses of short-lived nuclides.

In this effort, the masses of seven short-lived and one stable nuclides were investigated, almost all of them with a precision below 4 keV by ISOLTRAP. These high-precision mass values were included in the latest Atomic-Mass Evaluation 2003. All, except one (^{56}Mn), are in good agreement with the value recorded in the previous table [86]. Table 6.1 hereafter presents the mass measurements of these nuclides [87]. Their evaluation is presented in the following. This consists in a comparison of the ISOLTRAP measurement with all the previous ones and the final value chosen after the evaluation and recorded in the AME 2003 table. In all the following our measurements are presented as ISOLTRAP2003. All

these data were summarized and published for the ENAM'04 proceedings, presented at the end of this Chapter. The importance of links is also discussed.

Table 6.1: *Comparison between previous [86], ISOLTRAP and new mass excess values coming from AME2003 including the ISOLTRAP values [3]. All values are given in keV.*

Isotopes	AME95 Mass Excess	ISOLTRAP Mass Excess	AME2003 Mass Excess
^{56}Mn (2.6h)	-56905.6 (1.4)	-56910.3 (1.4)	-56909.7 (0.7)
^{57}Mn (85.4s)	-57485 (3)	-57486.4 (2.2)	-57486.8 (1.8)
^{82}Rb^{m} (6.5h)	-76121.1 (1.5)	-76118.8 (2.6)	-76119.1 (2.4)
^{82}Rb (1.27 m)		-76189 (7)	-76188.2 (2.8)
^{92}Sr (2.7h)	-82875 (7)	-82865.2 (4.0)	-82868 (3)
^{124}Cs (30.9s)	-81743 (12)	-81745.5 (14.2)	-81731 (8)
^{127}Cs (6.2h)	-86240 (9)	-86244.0 (7.2)	-86240 (6)
^{130}Ba (Stable)	-87271 (7)	-87260.2 (3.2)	-87261.6 (2.8)

Figure 6.1 presents the absolute precision of linked nuclides to ISOLTRAP measurements. More than 20 nuclides were influenced. This shows clearly that links in the table are important, and that ISOLTRAP measurements performed only on few nuclides decrease globally the uncertainties in the measurement region.

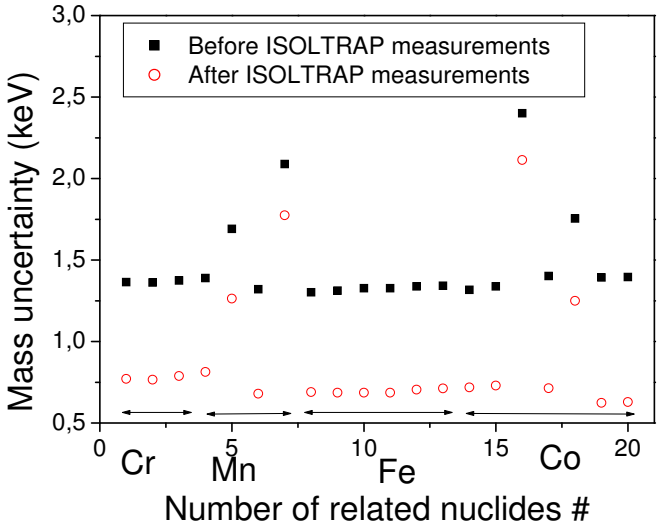

Figure 6.1: *Absolute precision of the 20 nuclides linked to ISOLTRAP measurements in the AME table. For all of them their uncertainty was decrease. Nuclides #1-3 are* $^{53-55}Cr$, #4-6 are $^{53-55}Mn$, #7-13 are $^{53-59}Fe$, and #14-20 are $^{54-60}Co$.

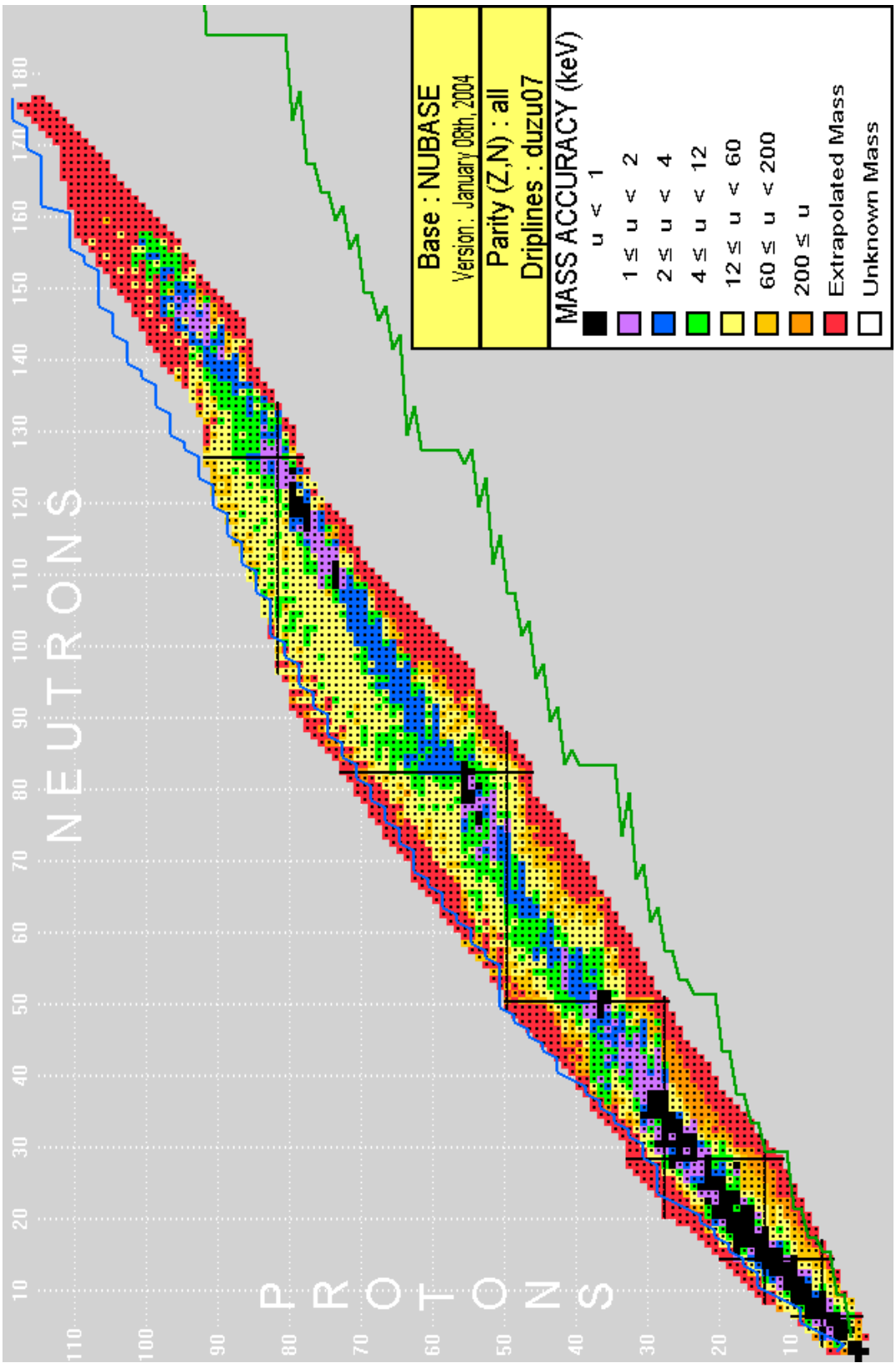

Figure 6.2: *The nuclear chart: number of protons versus number of neutrons, the range of mass accuracy u is indicated [8], nuclides with u below 1 keV constitute the backbone. Theoretical driplines from [9] are shown.*

^{130}Ba

^{130}Ba is a stable nuclide measured several times by different techniques (see Table 6.2). It was known with 7 keV uncertainty before the ISOLTRAP measurement. With ISOLTRAP its uncertainty was decreased to less than 3 keV (see figure 6.3). The new value is kept along with previous measurements, but their influence is much less than before (Table 6.2).

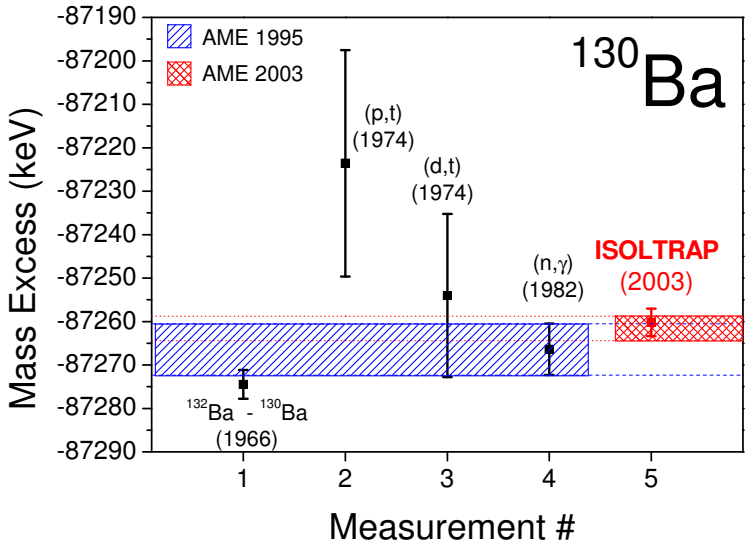

Figure 6.3: *Measurements of ^{130}Ba. The value recorded in the AME95 table was derived from the reactions $^{130}Ba(n,\gamma)^{131}Ba$ [88], ^{132}Ba-^{130}Ba [89], $^{130}Ba(d,t)^{129}Ba$ [90], and $^{130}Ba(p,t)^{128}Ba$ [91]. The new value recorded in the AME2003 table has an uncertainty two times smaller.*

Table 6.2: *Influence in % of each measurement on the two AME tables [3, 86] for ^{130}Ba.*

Type of Measurement	Year of Measurement	Influence on AME95 (%)	Influence on AME03 (%)
^{130}Ba$(n,\gamma)^{131}$Ba	1982	48.1	10.8
^{132}Ba$-^{130}$Ba	1966	39.5	8.9
^{130}Ba$(d,t)^{129}$Ba	1974	7.4	1.6
^{130}Ba$(p,t)^{128}$Ba	1974	5	1.1
ISOLTRAP	2003		77.6

^{127}Cs

^{127}Cs has a half-life of 6.25 h. Its mass was measured several times by β^+ spectroscopy, ESR, and ISOLTRAP. The final value based on the evaluation is including the ISOLTRAP-2003 measurement, but is not taking into account the ESR measurement, since its accuracy is more than 3 times worse. The final value is based on β^+ and ISOLTRAP values, it is closer from the one of ISOLTRAP since its influence is the largest, and the uncertainty is smaller. The weights are listed in Table 6.3 and the different mass values are plotted in figure 6.4.

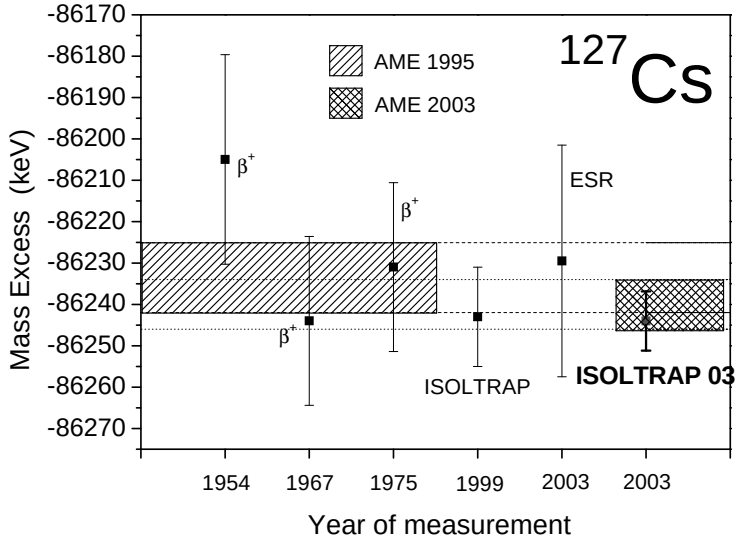

Figure 6.4: *^{127}Cs measurements done with $^{127}Cs(\beta^+)^{127}Xe$ [92, 93, 94], ESR measurement [17], ISOLTRAP measurement in 1999 [95], the resulting value recorded in the AME 1995 [86], and the 2003 ISOLTRAP value. The final value in the AME 2003 table [3] has an uncertainty 1.5 times smaller than in AME95.*

Table 6.3: *Influence in % of each ^{127}Cs measurement on the AME03 table [3] and on the table [96] before the ISOLTRAP03 measurement.*

Type of Measurement	Year of Measurement	Influence before ISOLTRAP03 (%)	Influence on AME03 (%)
$^{127}Cs(\beta^+)^{127}Xe$	1954-67-75	42.2	18
ESR	2003	9.1	0
ISOLTRAP	1999-2003	48.7	82

^{124}Cs

^{124}Cs has a half-life of 30.9 s. The mass value in the AME95 table was determined by an ISOLTRAP measurement from 1990 [97] and from an internal transition measurement from the first isomeric state. Since, ISOLTRAP has performed two new measurements [95], and the ESR [17] is providing also two values: one from a direct measurement and one from the first isomeric state measurement (see figure 6.5). Thus, the final value is including ESR and ISOLTRAP measurements. Note that the ISOLTRAP value from 1990, 1999, and 2003 are in excellent agreement, but a bit lower than the ESR value.

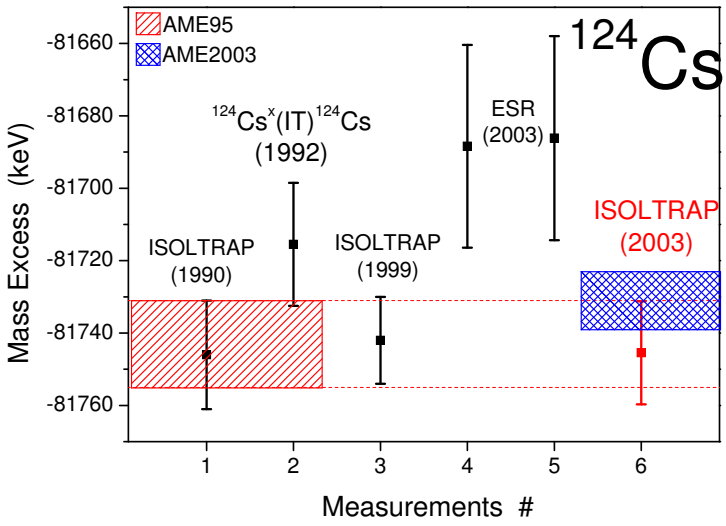

Figure 6.5: *Measurements of ^{124}Cs. The new value is a combination of ISOLTRAP measurements and ESR measurements [17].*

Table 6.4: *Influence in % of each measurement on the two AME tables [3, 86] for ^{124}Cs.*

Type of Measurement	Year of Measurement	Influence on AME95 (%)	Influence on AME03 (%)
$^{124}Cs^{x}(IT)^{124}Cs$	1992	16.1	29
ISOLTRAP	1990	83.9	13
ESR	2003		22
ISOLTRAP	1999-2003		36

^{92}Sr

^{92}Sr has a half-life of 2.7 h. All mass measurements performed before ISOLTRAP are from β-decay (see figure 6.6). The three values from ^{92}Rb(β^-)^{92}Sr reaction were averaged and the mean value accounted for 57.3% (see Table 6.5). After the evaluation β-decay values are still used but with a smaller influence. Figure 6.7 presents one of the two measurements performed on ^{92}Sr contributing to the ISOLTRAP03 [87] value.

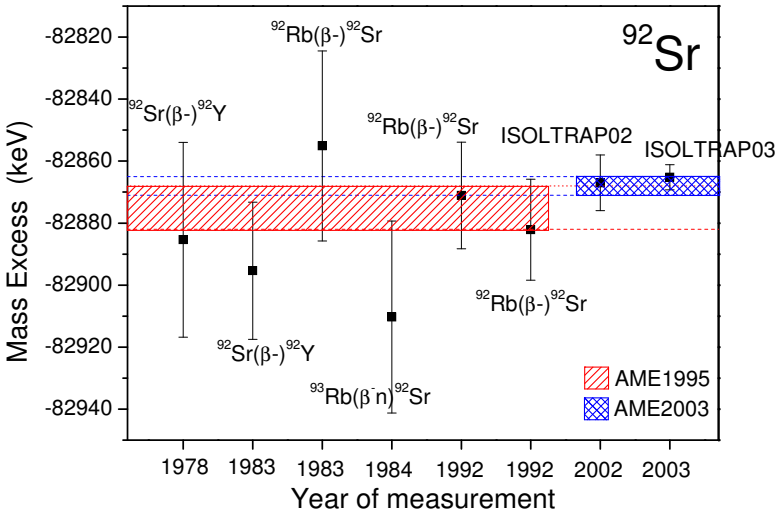

Figure 6.6: *Measurements of ^{92}Sr done with ^{92}Rb(β^-)^{92}Sr [98, 99, 100], ^{92}Sr(β^-)^{92}Y [98, 101], ^{93}Rb($\beta - n$)^{92}Sr [102], and ISOLTRAP in 2002 [103] and 2003 [87]. The final uncertainty was decreased by more than a factor 2.*

Table 6.5: *Influence in % of each measurement on the two AME tables [3, 86] for ^{92}Sr.*

Type of Measurement	Year of Measurement	Influence on AME95 (%)	Influence on AME03 (%)
^{92}Rb(β^-)^{92}Sr	1983-1992-1992	57.3	7.3
^{92}Sr(β^-)^{92}Y	1978-1983	33.0	2.9
^{93}Rb($\beta - n$)^{92}Sr	1984	9.7	1.2
ISOLTRAP	2002-2003		88.6

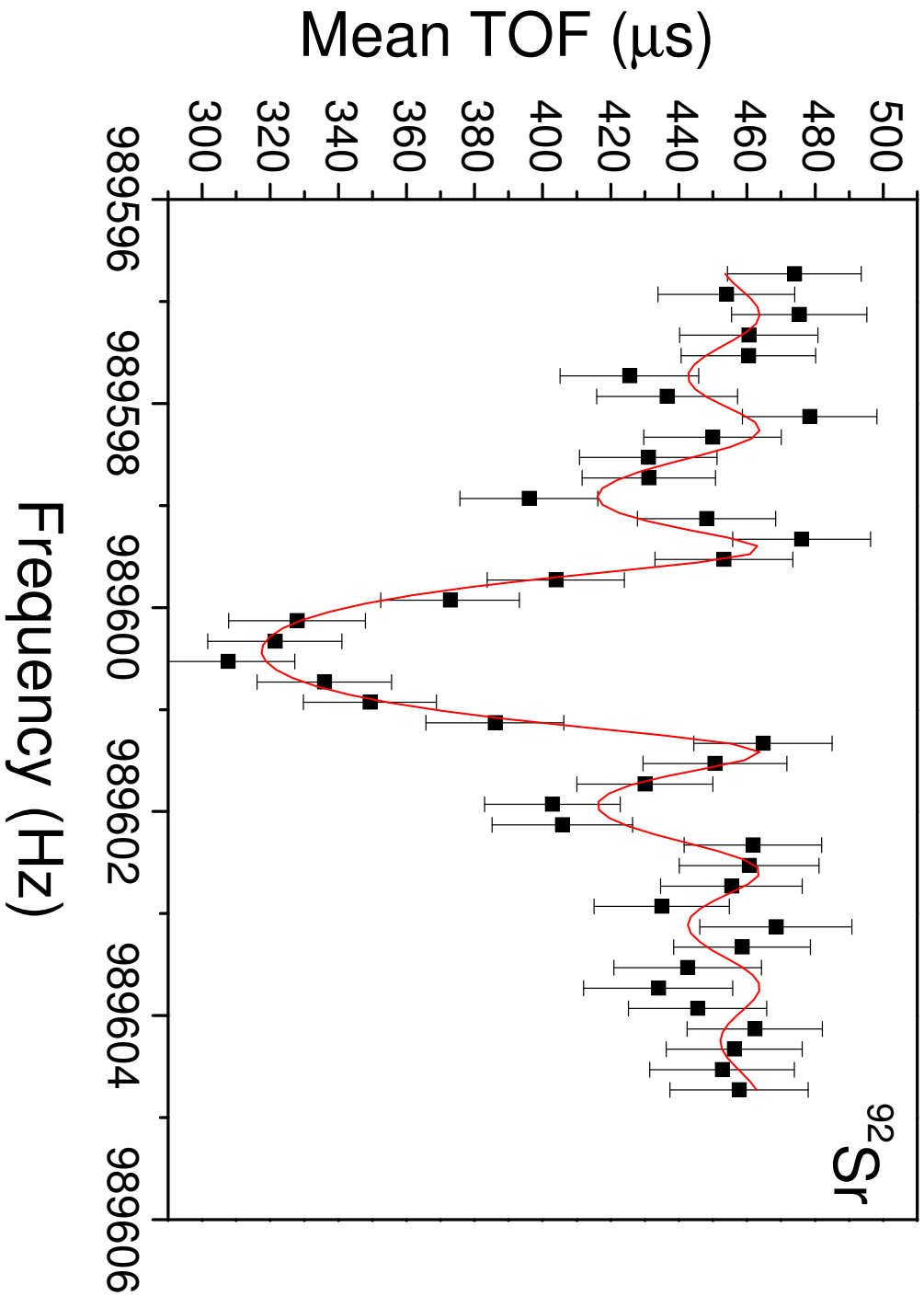

Figure 6.7: *Time of flight (TOF) as a function of the applied radio-frequency excitation for* ^{92}Sr *obtained with 1500 ions and an excitation time* $T_{RF} = 900\,ms$ *with a relative frequency uncertainty* $\delta\nu/\nu = 5 \cdot 10^{-8}$.

^{57}Mn

^{57}Mn was determined from ^{55}Mn$(t,p)^{57}$Mn [104], and ^{54}Cr$(\alpha,p)^{57}$Mn [105, 106]. The value recorded in the AME03 table after the evaluation of ISOLTRAP measurement is taking into account the ^{55}Mn$(t,p)^{57}$Mn and the ISOLTRAP values. The uncertainty of the ^{54}Cr$(\alpha,p)^{57}$Mn measurements were too large compared to the ISOLTRAP one (see figure 6.8).

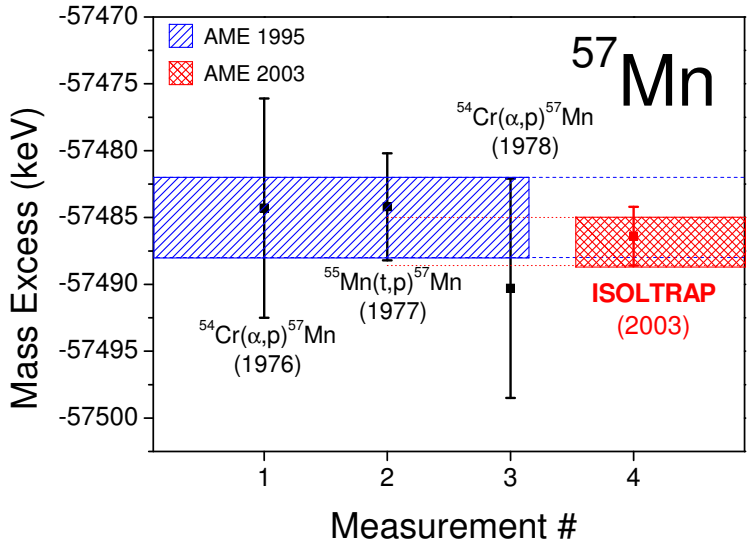

Figure 6.8: *Measurements of ^{57}Mn done with ^{55}Mn$(t,p)^{57}$Mn [104], ^{54}Cr$(\alpha,p)^{57}$Mn [105, 106], and ISOLTRAP. The final value is including the ^{55}Mn$(t,p)^{57}$Mn value and the ISOLTRAP one.*

Table 6.6: *Influence in % of each measurement on the two AME tables [3, 86] for ^{57}Mn.*

Type of Measurement	Year of Measurement	Influence on AME95 (%)	Influence on AME03 (%)
^{54}Cr$(\alpha,p)^{57}$Mn	1976	23.7	0
^{54}Cr$(\alpha,p)^{57}$Mn	1978	23.7	0
^{55}Mn$(t,p)^{57}$Mn	1977	52.6	25.5
ISOLTRAP	2003		74.5

^{56}Mn

In the case of ^{56}Mn, the ISOLTRAP measurement was not in agreement with the AME95 table, but a new measurement of ^{55}Mn$(n,\gamma)^{56}$Mn performed in 2003 confirms the ISOLTRAP value. The final value is based on all so far performed measurements (see figure 6.9). The ISOLTRAP value has an uncertainty twice bigger than the ^{55}Mn$(n,\gamma)^{56}$Mn measurement, so its influence on the final mass value is smaller (see Table 6.7).

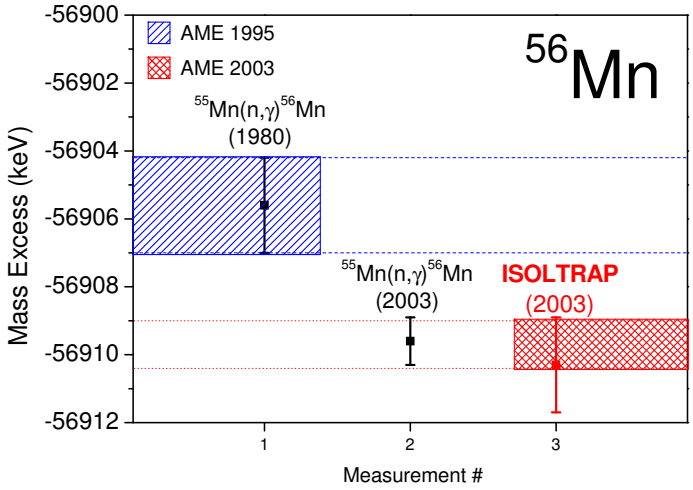

Figure 6.9: *Measurements of ^{56}Mn done with ^{55}Mn$(n,\gamma)^{56}$Mn in 1980 [107] and 2003 [108], and ISOLTRAP in 2003. The final value is based on the three measurements.*

Table 6.7: *Influence in % of each measurement on the two AME tables [3, 86] for ^{56}Mn.*

Type of Measurement	Year of Measurement	Influence on AME95 (%)	Influence on AME03 (%)
^{55}Mn$(n,\gamma)^{56}$Mn	1980	100	7.6
^{55}Mn$(n,\gamma)^{56}$Mn	2003		68.3
ISOLTRAP	2003		24.1

^{82}Rb^{m}

Thanks to the high resolving power of ISOLTRAP, we succeeded to resolve and to measure the isomeric state of ^{82}Rb. The energy difference between the ground state and its first isomeric state is known [109] to be 68.9(1.5) keV. But the ground state was known only with an uncertainty of $\delta m = 7$ keV. The high-precision measurement of ISOLTRAP on the isomeric state also influenced the ground state, known now with 2.8 keV uncertainty.

Page 1 proceeding backbone

Page 2 proceeding backbone

Chapter 7

Is *N*=32 a magic number?

Among the "new" magic numbers, $N = 32$ is now appearing as a good candidate. New elements of discussion are brought by ISOLTRAP mass measurements on $^{56-57}$Cr.

An introduction of the problem and relevant references are given in an accompanying conference[1] *publication presented at the end of this chapter.*

7.1 Mass Measurements on ^{56}Cr and ^{57}Cr

Data taking conditions of $^{56-57}$Cr are listed in Table 5.2. The mass evaluation was not discussed in the conference publication, it is presented hereafter.

For ^{56}Cr, two measurements of ^{54}Cr(t,p)^{56}Cr [110, 111] were existing, but their value was replaced in the table by the ISOLTRAP one, since its uncertainty is five times lower. These measurements are presented in figure 7.1.

The mass of ^{57}Cr was known with only 90 keV accuracy, coming from measurements of TOFI [112, 113] and ^{57}Cr(β^-)^{57}Mn [114]. It is known now with an uncertainty below 2 keV and the value is now based only on ISOLTRAP measurement, as shown in figure 7.2.

7.2 Magicity and deformation

Though not stated in the conclusion of the article, we believe that the effect described in the paper is related to deformation. Figure 7.3 presents a HFB calculation [115] of the potential energy using the D1S interaction (see Chapter 8) as a function of the quadrupole deformation parameter β of ^{57}Cr for different k^π, with k the projection of the angular momentum onto the symmetry axis.

The deformation of ~ 0.2 of the ground state ($I = 3/2^-$) may explain the observations showed up in this paper. This $N = 32$ sub-shell closure has been discussed extensively by Prisciandaro *et al.* who measured the 2^+ energy of ^{58}Cr [116]. Moreover the observations of Sorlin *et al.* on low-energy 2^+ states in Cr lead to the conclusion of a strong deformation of chromium isotopes [117]. This was also confirmed by calculations coming from

[1] NUSTAR Surrey 2005.

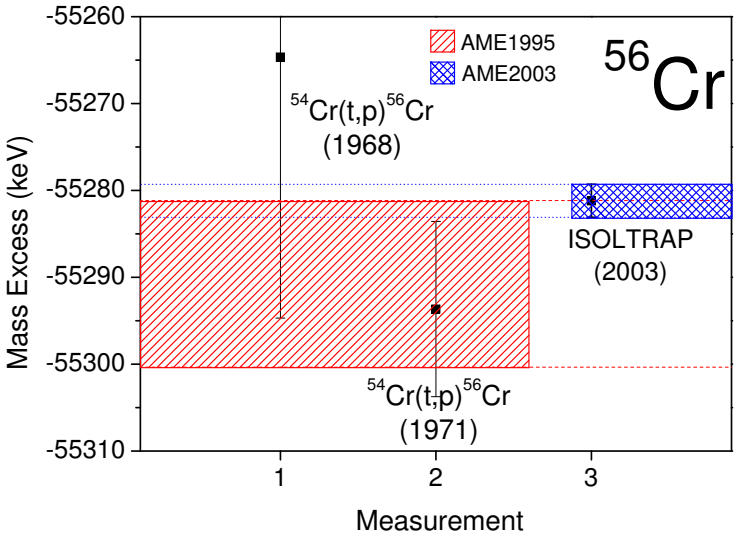

Figure 7.1: *^{56}Cr measurements done with ^{54}Cr(t,p)^{56}Cr [110, 111], the resulting value recorded in the AME 1995 [86], and the ISOLTRAP value. The final value in the AME 2003 table [3] has an uncertainty five times lower.*

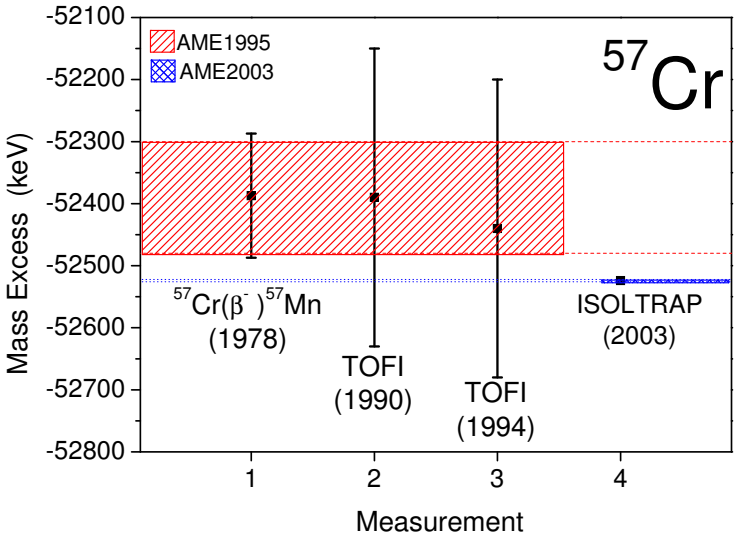

Figure 7.2: *^{57}Cr measurements done with ^{57}Cr(β^-)^{57}Mn [114], TOFI measurements [112, 113], the resulting value recorded in the AME 1995 [86], and the ISOLTRAP value. The final value in the AME 2003 table [3] has an uncertainty 120 times smaller.*

Raman *et al.* [118], which predicted (from an empirical relation) the quadrupole deformation parameter β to be 0.26 for ^{56}Cr and 0.27 for ^{58}Cr. The FRDM calculations [119] predicted $\beta = 0.189$ for ^{56}Cr and $\beta = 0.199$ for ^{57}Cr, values in good agreement with the HFB calculations.

All these measurements and predictions affirm a deformation of the chromium isotopes, which could explain the observations presented in our paper based on mass measurements. More measurements on nuclides further from the stability may confirm the non-existence of a sub-shell closure at $N = 32$.

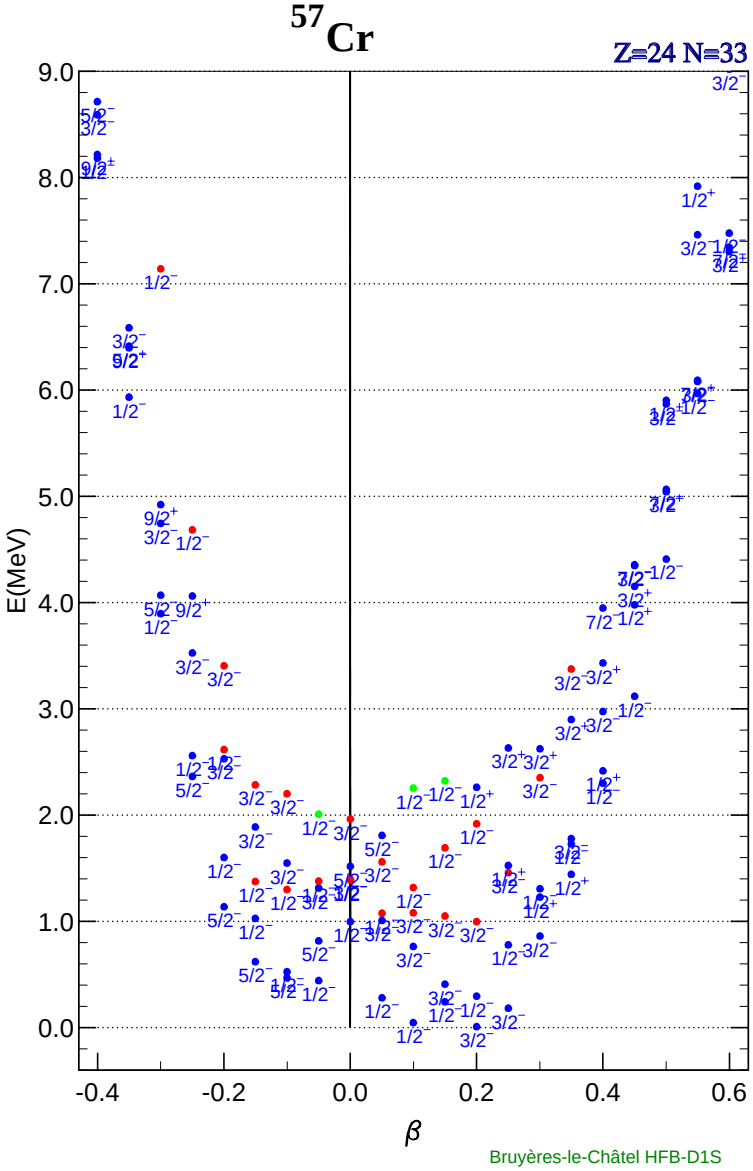

Figure 7.3: *Binding energy as a function of the deformation β for ^{57}Cr for different levels differentiated by their spin.*

7.3 Mass measurements of $^{56-57}$Cr and the question of shell reincarnation at N=32

page1 papier

page2 papier

page3 papier

page4 papier

page5 papier

page6 papier

Chapter 8

The case of *N*=40: Magic or not magic?

High-precision mass measurements were performed at ISOLTRAP to bring some elements to the question of shell closure at N=40. These measurements are presented within the experimental and theoretical context.

8.1 The magicity at *N*=40

According to Bohr and Mottelson [4]:

> In terms of the expansion of the total binding energy, the shell structure appears as a small correction compared to the surface energy, and the observed fluctuations in the binding energy function amounts to only about 1% (...) Despite the smallness of these effects on the scale of the total nuclear energy, they are of decisive importance for the structure of the low-energy nuclear spectra, which are especially sensitive to the configurations of the few most weakly bound nucleons.

As stated in the introduction a striking parallel between the atomic and nuclear system is that of closed shells. The behavior of the neutral system is largely governed by an almost infinitely massive and point-like nucleus. Describing nuclear behavior, however, is a particularly difficult task given its composition of neutrons and protons, similar in mass yet different in charge.

A property crucial to the understanding of the nuclear system is the behavior of shell structure as a function of the varying composition of protons and neutrons. The fact that shell structure seems to be modified in systems where the N and Z become unbalanced, is one of the key questions of nuclear physics today. One case of considerable interest is that of $N = 40$, due to the unexpected turn of events since the first studies in 1982.

Bernas *et al.* [120] showed in 1982 that the first excited state of ^{68}Ni was 0^+, establishing a new case of 2^+ and 0^+ inversion. This was compared to the case of $^{90}_{40}Zr_{50}$ and $^{40}_{20}Ca_{20}$, two doubly-magic[1] nuclides in which such an inversion was known. Consequently, Bernas *et al.* claimed ^{68}Ni was a doubly-magic nucleus.

[1] Since several years the $Z = 40$ shell closure has been established [121], by its well known level structure.

Since the binding energy is the key quantity for indicating whether a nuclide might be magic or not (see above), mass measurements from TOFI in 1994 [113] were performed. Though they gave no indication that $N = 40$ was magic, the precision was not sufficient to probe further.

Broda *et al.* [122] in 1995, gave a good summary of spectroscopy work since Bernas *et al.* in 1982 and elaborated the excited spectrum of ^{68}Ni concluding that it was spherical, and indicating a significant sub-shell closure at $N = 40$. They made a comparison with ^{90}Zr and looked for new states in ^{68}Ni. They found the 0^+ as the first excited state, as Bernas *et al.* [120], 2^+ as second excited state with a production of a 5^- isomeric state. This is exactly the same situation as for the ^{90}Zr excited states. They also made a comparison with the ^{80}Zr ($N = Z = 40$) which they found to be strongly deformed and absolutely not magic.

Shell model predictions of the appearance of isomeric states near magic nuclides motivated the experimental investigations of Grzywacz *et al.* [123] in 1998 who discovered many in the vicinity of ^{68}Ni, further strengthening the case for its doubly-magic character.

β-decay studies were then carried out by Hannawald *et al.* [124] in 1999, who measured a long half-live of the neighboring isotones (Cu, Mn) at $N = 40$ that indicated an (unanticipated) increase in collectivity *i.e.* closed-shell nature. However β-decay studies by Mueller *et al.* [125] in 1999 concluded that the stabilizing effect of $N = 40$ failed away from ^{68}Ni.

The powerful tool of Coulomb excitation was then brought to bear on ^{68}Ni. Sorlin *et al.* [126] in 2002 found that the resulting $B(E2)$ value[2] was unexpectedly small, reenforcing the magic nature of ^{68}Ni. Though their $B(E2)$ value indicated $N = 40$ magic, Sorlin *et al.* attributed the lack of evidence from binding energy for an erosion of the $N = 40$ sub-shell. However, a concerted theoretical effort by Langanke *et al.* [127] argued against the doubly-magic nature of ^{68}Ni arguing that the "missing" $B(E2)$ strength lies at much higher energy (>4 MeV).

In the light of these conflicting experimental and theoretical signatures as well as the relatively large uncertainty on the binding energies in this interesting region, high precision mass measurements were carried out in an attempt to bring at least some clarification to this situation.

The studies were also motivated by the interesting pairing and superfluidity arguments of Van Isacker [128] which offer an explanation for the step-like behavior observed in the S_{2n} curves.

The measurements and their evaluation are described in section 8.2 followed by their comparison to nuclear mass models in section 8.3 and 8.4. The question of N=40 is discussed in section 8.5.

[2]The probability of transition between the ground state 0^+ and the excited state 2^+, which is one of the most used parameters for shell closure studies. It is expected to be small for magic nuclides which are difficult to excite, and to become large for deformed nuclides.

Table 8.1: *Comparison between previous, ISOLTRAP, and new mass excess (ME) values for Ni (all values are given in keV). The influence of our measurement on the final mass value is given in %. The values listed in the new Atomic-Mass Evaluation (AME2003 [3]) already include our data.*

Isotopes	Half life $T_{1/2}$	AME95 ME (keV)	ISOLTRAP ME (keV)	AME2003 ME (keV)	Influence of our measurement
^{57}Ni	35.60 h	-56075.5 (2.9)	-56084.2 (2.5)	-56082.0 (1.8)	52 %
^{60}Ni	Stable	-64468.1 (1.4)	-64472.7 (1.4)	-64472.1 (0.6)	16.6 %
^{64}Ni	Stable	-67095.9 (1.4)	-67096.9 (1.3)	-67099.3 (0.6)	21.9 %
^{65}Ni	2.52 h	-65122.6 (1.5)	-65129.0 (2.3)	-65126.1 (0.6)	7.8 %
^{66}Ni	54.6 h	-66028.7 (16.0)	-66006.3 (1.4)	-66006.3 (1.4)	100 %
^{67}Ni	21 s	-63742.5 (19.1)	-63742.7 (2.9)	-63742.7 (2.9)	100 %
^{68}Ni	29 s	-63486.0 (16.5)	-63463.8 (3.0)	-63463.8 (3.0)	100 %
^{69}Ni	11.5 s	-60380 (140)	-59978.6 (3.7)	-59979 (4)	100 %

8.2 Nuclides in the region of N=40

ISOLTRAP measured more than thirty nuclides in the region of N=40, presented here.

Eight isotopes of nickel, eleven of copper, and fourteen of gallium were investigated with ISOLTRAP. All these measurements were evaluated in order to be included in the Atomic-Mass Evaluation table. For each value measured, the percentage counting in the new value is given in the Tables 8.1, 8.2, and 8.3 which record all values measured by ISOLTRAP used in this study. For most of them the mass accuracy was improved as compared to the mass table and for many of the copper isotopes they were even measured for the first time. Their previous value was then estimated from systematic trends.

Ni

The nickel results are presented in Table 8.1 and in figure 8.1. The ^{69}Ni mass value is presented in figure 8.2, this is a special case because it was completely in disagreement with the previous value recorded in the table [86]. This value was a combination from the two reaction measurements performed on this mass [113, 129], but the final value was closer to the ^{70}Zn(^{14}C,^{15}N)^{69}Ni reaction since its precision was better. The ISOLTRAP value disagrees with this one but is still in agreement with the time-of-flight measurement. And since the value of ISOLTRAP is more accurate and with a better precision, the evaluation procedure lets only the value measured by ISOLTRAP counting in the final mass value. It shows the importance of the evaluation step in a mass measurement procedure.

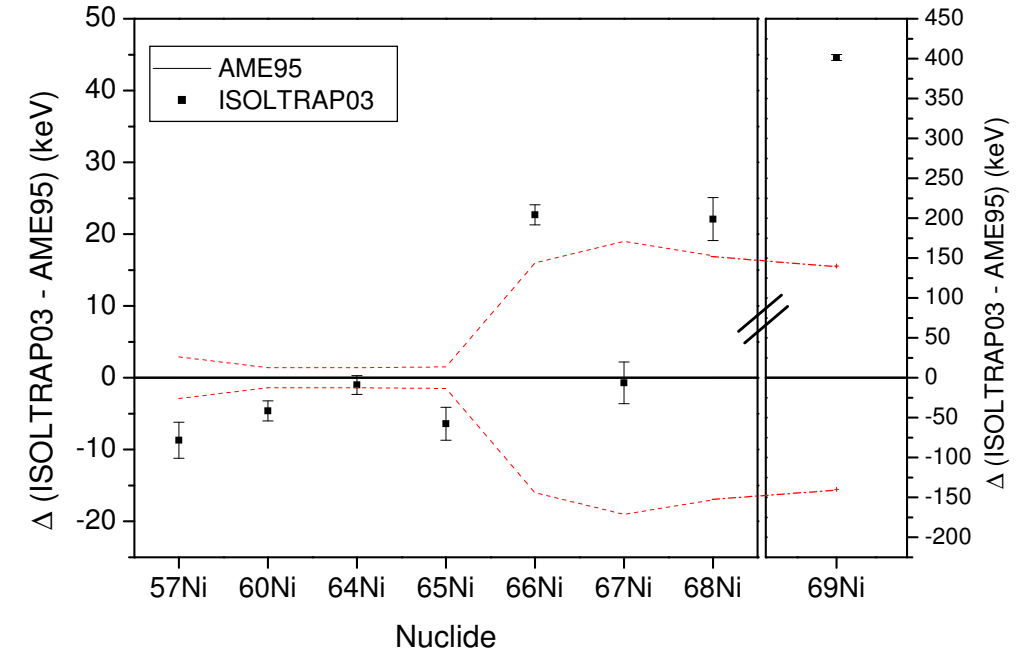

Figure 8.1: *Difference between the ISOLTRAP mass excess results for Ni and the 1995 AME values. Dashed lines represent the AME95 error bars. For all of them the precision was improved.*

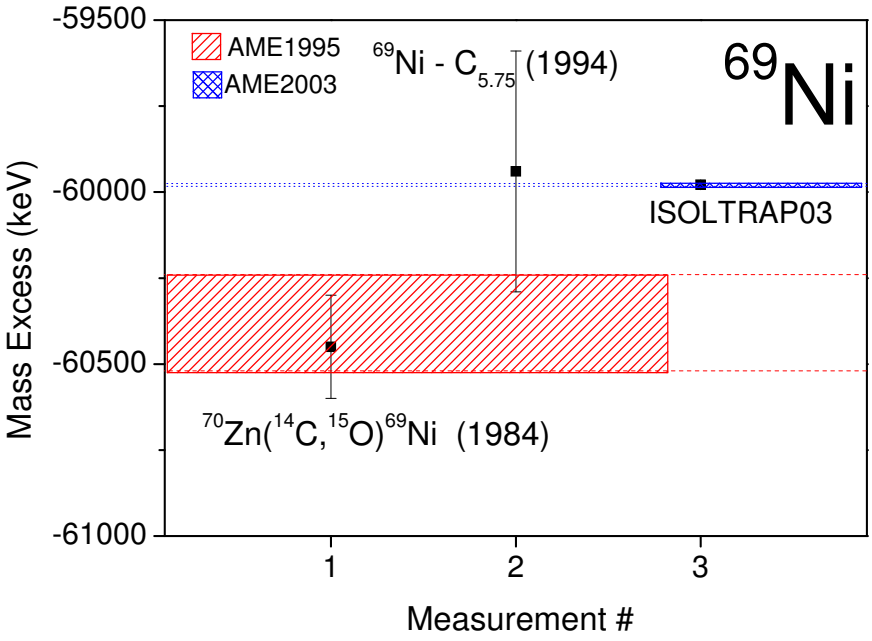

Figure 8.2: *Mass excess of ^{69}Ni: measurements performed with ^{70}Zn(^{14}C,^{15}N)^{69}Ni [129], and a time of flight measurement [113], the resulting AME 1995 value [86], and the ISOLTRAP value. The final AME 2003 value [3] has now an uncertainty 30 times smaller.*

Cu

All Copper results are presented in Table 8.2, a comparison with previous measurements is given in figure 8.4. The important difference with the previous value of ^{70}Cu^{n} was due to an incorrect state assignment. ISOLTRAP's high resolving power of more than 10^6 allowed to perform a clear identification of each state [130]. Moreover, this high resolving power allowed to resolve isomeric states in ^{68}Cu [131]. This is depicted in figure 8.3 which shows the measurement of the two states of ^{68}Cu.

Table 8.2: *Comparison between previous, ISOLTRAP, and new mass excess (ME) values for Cu (all values are given in keV). Previously unknown values only derived from systematic trends are marked with #. The influence of our measurement on the final mass value is given in %. The values listed in the new Atomic-Mass Evaluation (AME2003 [3]) already include our data.*

Isotopes	Half life $T_{1/2}$	AME95 ME (keV)	ISOLTRAP ME (keV)	AME2003 ME (keV)	Influence of our measurement (%)
^{65}Cu	Stable	-67259.7 (1.7)	-67264.5 (1.1)	-67263.7 (0.7)	36.8 %
^{66}Cu	5.120 m	-66254.3 (1.7)	-66258.8 (2.0)	-66258.3 (0.7)	11.1 %
^{67}Cu	61.83 h	-67300.2 (8.1)	-67318.8 (1.2)	-67318.8 (1.2)	100 %
^{68}Cu^{g,3}	31.1 s	-65541.9 (45.6)	-65567.0 (1.6)	-65567.0 (1.6)	100 %
^{68}Cu^{m}	3.75 m	-64818 (50)	-64850.3 (1.5)	-64845.4 (1.7)	50 %
^{69}Cu	2.85 m	-65739.9 (8.1)	-65736.2 (1.4)	-65736.2 (1.4)	100 %
^{70}Cu^{g}	44.5 s	-62960.3 (14.5)	-62976.1 (1.6)	-62976.1 (1.6)	100 %
^{70}Cu^{m}	33 s	-62859 (15)	-62875.4 (2.0)	-62875.4 (2.0)	100 %
^{70}Cu^{n}	6.6 s	-62617 (15)	-62734.1 (2.1)	-62734.1 (2.1)	100 %
^{71}Cu	19.4 s	-62764.2 (35.2)	-62711.1 (1.5)	-62711.1 (1.5)	100 %
^{72}Cu	6.6 s	-60060# (200#)	-59783.0 (1.4)	-59783.0 (1.4)	100 %
^{73}Cu	4.2 s	-59160# (300#)	-58986.6 (3.9)	-58987 (4)	100 %
^{74}Cu	1.594 s	-55700# (400#)	-56006.2 (6.2)	-56006 (6)	100 %
^{76}Cu	641 ms	-50310# (600#)	-50976.0 (6.7)	-50976 (7)	100 %

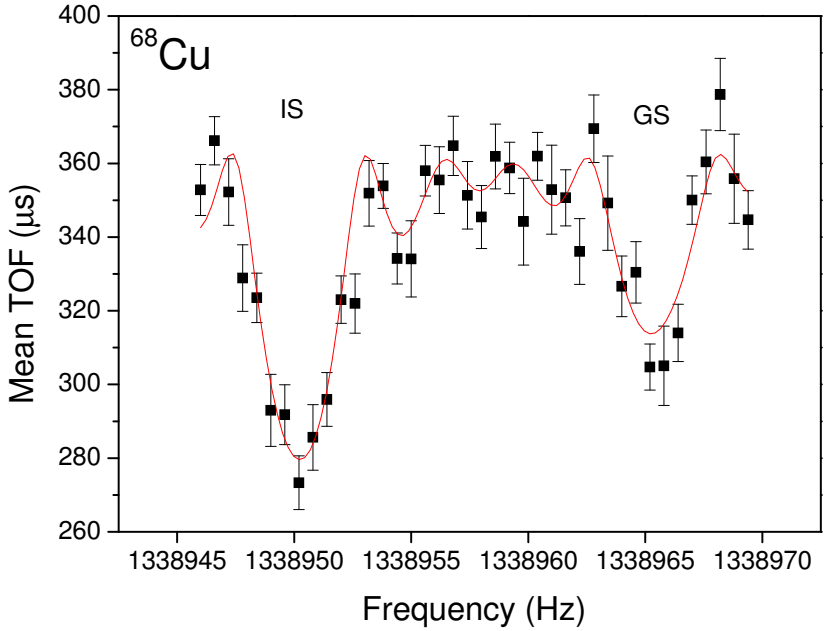

Figure 8.3: *Time of flight (TOF) as a function of the applied radio-frequency excitation for* ^{68}*Cu ions. This measurement was performed with 4300 ions and an excitation time* $T_{RF} = 300\,ms$*. The ground state and the first isomeric state were measured at the same time.*

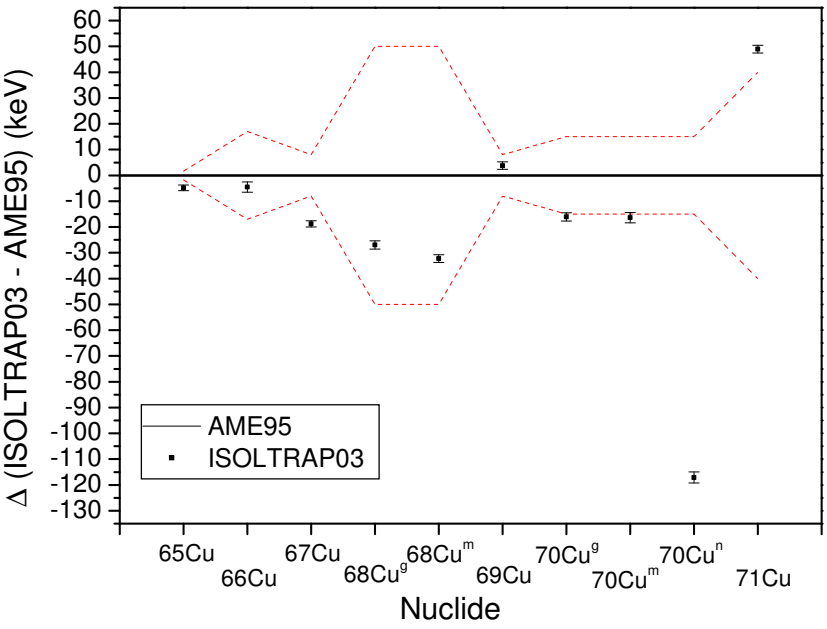

Figure 8.4: *Difference between ISOLTRAP mass excess results for Cu and the 1995 AME values. Dashed lines represent the AME95 error bars. g denotes ground states, m,n isomeric states.*

Ga

The gallium results are presented in Table 8.3 and in figure 8.6. Figure 8.5 shows a typical resonance curve obtained for gallium measurements. The ^{68}Ga mass uncertainty is much higher than for all the other nuclides. This is due to a lack of statistics: only 530 ions were used, compared to at least 3000 for the other ones, since the precision is directly related to the statistics (see eq. 3.6). Our value is still in agreement with the previous one, but due to the low precision on this measurement, this value was not taken into account in the mass table.

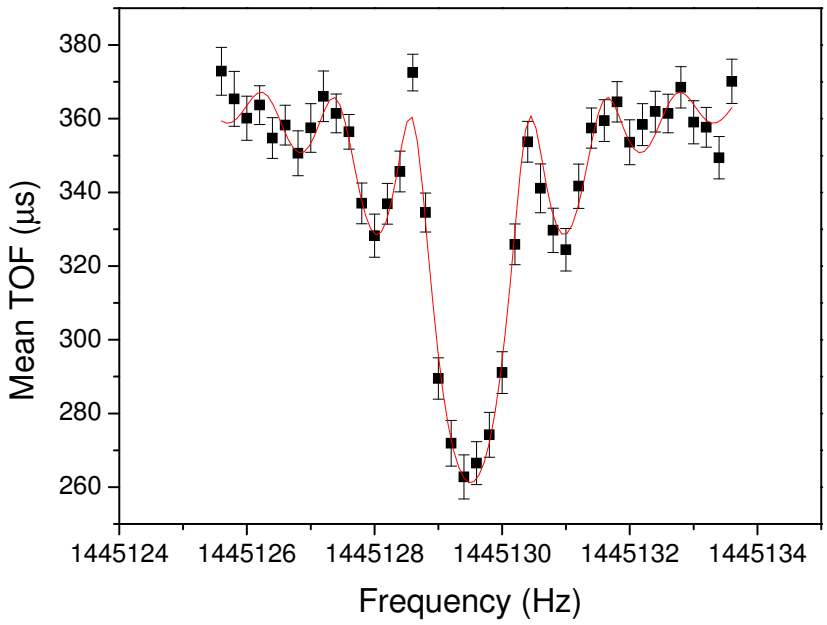

Figure 8.5: *Time of flight (TOF) as a function of the applied radio-frequency excitation for ^{63}Ga ions, obtained with 1500 ions and an excitation time $T_{RF} = 900\,ms$ with a relative frequency uncertainty $\delta\nu/\nu = 3 \cdot 10^{-8}$.*

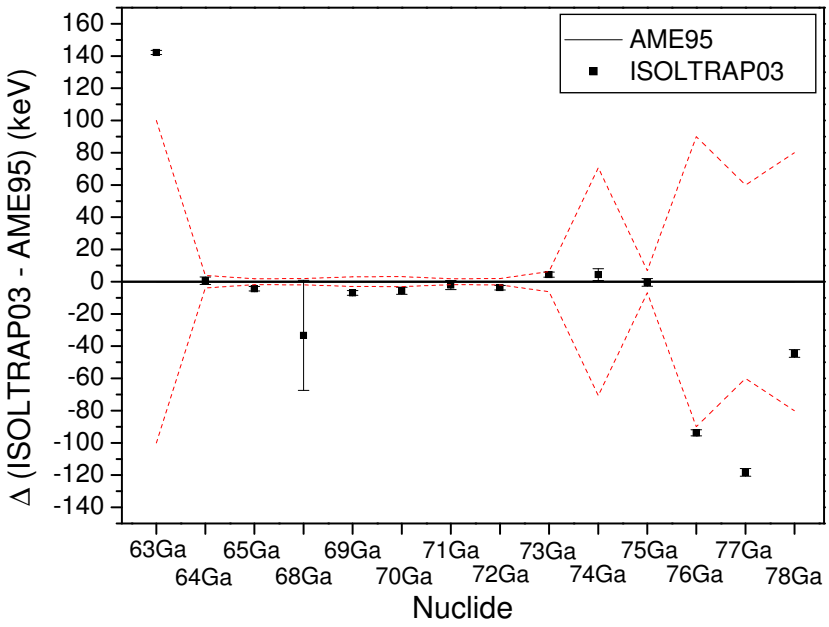

Figure 8.6: *Difference between ISOLTRAP mass excess results for Ga and the 1995 AME values. Dashed lines represent the AME95 error bars.*

Table 8.3: *Comparison between previous, ISOLTRAP, and new mass excess (ME) values for Ga (all values are given in keV). The influence of our measurement on the final mass value is given in %. The values listed in the new Atomic-Mass Evaluation (AME2003 [3]) already include our data.*

Isotopes	Half life $T_{1/2}$	AME95 ME (keV)	ISOLTRAP ME (keV)	AME2003 ME (keV)	Influence of our measurement (%)
^{63}Ga	32.4 s	-56689.3 (100.0)	-56547.1 (1.3)	-56547.1 (1.3)	100 %
^{64}Ga	2.627 m	-58834.7 (3.9)	-58834.1 (2.3)	-58834.3 (2.0)	75.2 %
^{65}Ga	15.2 m	-62652.9 (1.8)	-62657.3 (1.4)	-62657.2 (0.8)	35.6 %
^{68}Ga	67.71 m	-67082.9 (2.0)	-67116.2 (34.1)	-67086.1 (1.5)	0 %
^{69}Ga	Stable	-69320.9 (3.0)	-69327.9 (1.5)	-69327.8 (1.2)	65.3 %
^{70}Ga	21.14 m	-68904.7 (3.1)	-68910.3 (2.2)	-68910.1 (1.2)	31.8 %
^{71}Ga	Stable	-70136.8 (1.8)	-70138.9 (2.8)	-70140.2 (1.0)	13.3 %
^{72}Ga	14.10 h	-68586.5 (2.0)	-68590.2 (1.4)	-68589.4 (1.0)	53 %
^{73}Ga	4.86 h	-69703.8 (6.3)	-69699.4 (1.7)	-69699.3 (1.7)	100 %
^{74}Ga	8.12 m	-68054.0 (70.7)	-68049.6 (3.7)	-68050 (4)	100 %
^{75}Ga	126 s	-68464.2 (6.8)	-68464.6 (2.4)	-68464.6 (2.4)	100 %
^{76}Ga	32.6 s	-66202.9 (90.0)	-66296.7 (2.0)	-66296.6 (2.0)	100 %
^{77}Ga	13.2 s	-65874.1 (60.0)	-65992.4 (2.4)	-65992.3 (2.4)	100 %
^{78}Ga	5.09 s	-63662.1 (80.1)	-63706.6 (2.4)	-63706.6 (2.4)	100 %

8.3 Theoretical models applied to mass calculations around N=40

Various models can be used for mass predictions. They differ by their properties, hypothesis and their domain of validity.

Various models and formulas have been developed over the years to predict properties of nuclides, for instance their mass. A review of them can be found, for instance, in [2]. We have chosen to compare our experimental data to few of them: the Bethe-Weizsäcker mass formula, based on the liquid drop model, one of other global approaches: the Duflo-Zuker (DZ) mass formula, one of the macroscopic-microscopic approaches: the finite-range droplet model (FRDM), and various microscopic approaches using Hartree-Fock Bogolioubov (HFB). Shell-model calculations [132] are useful to know excitation energies, but not dedicated for mass prediction even if efforts have been intended in this direction [133].

The comparison is done with two categories of models: Models adjusted to the entire mass table or microscopic models adjusted only to the properties of a few nuclides. Microscopic models are based on the self-consistent HFB mean field and beyond: for example associating the GCM-GOA (Generator Coordinate Method used with the Gaussian Overlap approximation) taking into account some long-range correlations (rotation, vibration), projection,...

Bethe-Weizsäcker mass formula

A first model of the nuclear binding energy was made by C.F. von Weizsäcker [134, 135]. Representing the nucleus with Z protons and N neutrons as a liquid drop, the formula for its mass m is given by:

$$m(N,Z)c^2 = Zm_pc^2 + Nm_nc^2 - a_vA + a_sA^{2/3} + a_cZ^2A^{-1/3} + a_{sym}\frac{(Z-A/2)^2}{A}, \quad (8.1)$$

where m_p and m_n are proton and neutron masses, and A the mass number of the nucleus. The parameters are a_v the volume term, a_s the surface term, a_c is the Coulomb parameter, and a_{sym} the asymmetry parameter. Over the years this formula was adapted and various calculations for the coefficients were performed.

The adapted formula from Pearson [136], with a pairing term of Fletcher [137], for its binding energy per nucleon is given by:

$$\begin{aligned}\frac{E_{nuc}}{A} &= a_{vol} + a_{sf}A^{-1/3} + \frac{3e^2}{5r_0}Z^2A^{-4/3} + (a_{sym} + a_{ss}A^{-1/3})I^2 \\ &\quad + a_pA^{-y-1}\Big(\frac{(-1)^Z + (-1)^N}{2}\Big),\end{aligned} \quad (8.2)$$

with $I = (N-Z)/A$. The parameters are $a_{vol} = -15.65$ MeV, $a_{sf} = 17.63$ MeV, $a_{ss} = -25.60$ MeV which is the surface symmetry term introduced by Myers and Swiatecki [138], $a_{sym} = 27.72$ MeV, $r_0 = 1.233$ fm with r_0 the constant used in the radius estimation $R \simeq r_0A^{1/3}$, $a_p = -7$ MeV the pairing term, and $y = 0.4$. This formula is not taking

into account shell effects, so it is not a good way to predict exotic mass values but it can be used as a neutral indication for shell structures (see section 8.5.4).

The Duflo-Zuker mass formula

It is not strictly a microscopic approach since no nucleonic interaction appears implicitly [139]. The starting point of this formula is the assumption that there exist effective interactions. It is mainly based on Hartree-Fock calculations with adding a part of the residual interaction, pairing and Wigner correlations, without taking into account rotational energies. This formula has been updated over the years to fit as much as possible the mass tables [86], using in the last version 28 parameters.

Finite-range droplet model

There are two parts in this model [119]: a macroscopic one based on the liquid drop model and a microscopic one including Strutinsky shell corrections, pairing corrections, a charge-asymmetry term, and a Wigner term. This model is based on a mass fit using 31 parameters. It provides a large number of nuclear-structure properties in addition to nuclear ground-state masses. A more detailed description may be found in Lunney *et al.* [2].

Microscopic approaches: Mean-field theories & Beyond mean field

At present, microscopic nuclear models are based on the interaction between nucleons. Here, we will concentrate on the mean-field models. It is assumed that a nucleon moves independently in a mean field created by the other nucleons. The Hartree-Fock (HF) approach is based on the two-body non-relativistic Hamiltonian:

$$H = \sum_{i=1}^{A} T_i + \sum_{i<j=1}^{A} v_{ij}^{eff}, \tag{8.3}$$

where T_i is the kinetic energy operator for the i^{th} nucleon and defined as $T_i = \frac{\overrightarrow{p_i}^2}{2m_i}$ with m_i the nucleon mass and v_{ij}^{eff} is the interaction between nucleon i and j. To simplify this problem, one has to consider that every nucleon is moving independently in a potential created by its interaction with other nucleons $U(\overrightarrow{r}_i)$. The hamiltonian becomes:

$$\begin{aligned} H &= \sum_{i=1}^{A} \Big[\frac{\overrightarrow{p_i}^2}{2m_i} + U(\overrightarrow{r}_i)\Big] + \Big(\sum_{i<j=1}^{A} v_{ij}^{eff} - \sum_{i=1}^{A} U(\overrightarrow{r}_i)\Big) \\ &\equiv H_0 + V_{res}, \end{aligned} \tag{8.4}$$

where H_0 describes the motion of an independent particle in a one-body potential (U), and where V_{res} is the difference (residual) between this potential and the "real" potential v_{ij}^{eff}. The wave function Ψ has the form of a Slater determinant $\Psi = \det(\psi_i(x_i))$, which is a properly antisymmetrized product of the single-particle wave function $\psi_i(x_i)$. The unknown wave functions $\psi_i(x_i)$ are the eigenfunctions of the so-called HF-equation, which

is a single-particle Schrödinger-like equation:

$$\Big(-\frac{\hbar^2}{2m}\nabla^2+U\Big)\psi_i=\varepsilon_i\psi_i. \tag{8.5}$$

The solution of this equation is obtained by minimizing the energy $E_{HF}=\langle\Psi|H^{eff}|\Psi\rangle$. Various HF calculations differ by the choice of the effective potential v_{ij}^{eff}. Most of the calculations which were performed employ the so-called zero-range Skyrme force [140] or the finite-range Gogny force [141]. The BCS method and more generally the Hartree-Fock-Bogoliubov (HFB) method introduce pairing correlations compared to HF including independent quasi-particles. This is the most used method in mean field theory.

***Calculations using Skyrme forces**

Calulations using Skyrme forces are either applied to a wild range of nuclides properties [142, 143, 144, 145], even if some calculations are developed in order to increase the mass predictive power of these models [146]; or either devoted to fit the mass table: a large range of them was produced over the last few years, a brief description of possible calculations is presented hereafter.

- HFBCS-1: A ten-parameter Skyrme force, along with a four-parameter δ-function pairing force, have been fitted, using the Hartree-Fock-BCS method, to the masses of 1719 nuclei [147, 148].
- HFB-1: Being based on the Hartree-Fock-Bogoliubov method, it also used a ten-parameter Skyrme force, a four-parameter δ-function pairing force and a two-parameter phenomenological Wigner term [149].
- HFB-2: This mass formula was developed to correct the two previous ones: the δ-function pairing was improved to be force density-dependent, and a Wigner term linear in $|N-Z|$ was added. This is a 18-parameter Skyrme force fitted on 2135 measured masses [150].
- HFB-3: This is an improvement of HFB-2, the form of the density dependence of the δ-function pairing being determined by nuclear-matter calculations [151].
- HFB-4-5-6-7: Four tables producing data for 9200 nuclei. They suppose different constraints on the "isoscalar effective mass". HFB-4 and HFB-6 have a density-independent pairing, while HFB-5 and HFB-7 have a density-dependent pairing [152].
- HFB-8: It is built from HFB-6, the difference being in the particle number projection of the wave function [153].
- HFB-9: The HFB-8 was modified to conform the Friedman-Pandharipande calculation of neutron matter [154].

We will compare our data to HFB-2 and HFB-8, because they are the two mass tables the most devoted to mass predictions, HFB-2 is the first one, and HFB-8 is better to predict the entire mass table than HFB-9 which is more dedicated to r-process calculations and neutron-star studies.

***HFB on beyond with the Gogny force**

These calculations, mainly performed in Bruyères-le-Châtel and Orsay [155, 156, 157], use the D1S Gogny force which uses of bulk properties of doubly magic nuclides. But in general, HFB wave functions are not well suited to describe fundamental and excited states of the nuclei: one HFB state is not sufficient to describe the system. To get a complete description, a dynamic state of the system has to be generated. To this purpose, the Generator Coordinate Method (GCM) is used to find the wave function and the nuclei energy of the fundamental state, and wave functions of excited states. Moreover the GCM method is used with the Gaussian Overlap approximation (GOA) in order to take into account as much as possible deformations of the nuclei and to couple to the rotation. The GCM-GOA calculation goes beyond mean field theory by including long-range correlations *i.e.* the GCM method is used to correct the symmetry-breaking induced by the non-spherical HFB and to correct the value of the binding energy by the energy vibration-rotation not estimated with a pure HFB calculation.

HFB and GCM-GOA binding energy calculations are shown in figure 8.7 for Ni, Zn, and Ge isotopes. As expected, the GCM-GOA is closer to the experimental results. To compare, with experimental values, and other theories, the GCM one was chosen because it is taking into account correlation terms due to rotation and vibrations, contributions introduced in an approximate way in other mean-field approaches (HFB2-08).

This figure clearly shows that the HFB model is not sufficient to predict mass values, but long-range correlations and rotation-vibration corrections should be added. This is well done with the GCM-GOA method. This clearly shows that the explicit inclusion of correlations is decisive to describe masses. Nevertheless, the difference between experiments and theory is still ± 1 MeV.

8.4 Comparison between experimental results and models

Most of the theoretical predictions present difference with experimental results as shown in figure 1.3, here are presented the comparison between our results and the mass models presented in the previous part.

8.4.1 Two proton gap and paring gap energy

The enhancement of shell effects can be seen in the neutron (non-)dependence of the two-proton gap, defined as

$$\Delta_p(N,Z) = B(N,Z-2) - 2B(N,Z) + B(N,Z+2), \tag{8.6}$$

where B is the binding energy. Δ_p is proportional to the difference between the Fermi energies of nuclides differing by two protons, and thus it is a measure of shell gaps. There is a reduction of Δ_p when going away from magic numbers. Figure 8.8 presents this two-proton gap as a function of neutron number N for Ni, Cu, and Zn, it shows that the predictions obtained with HFB-D1S are following a good trend for Ni and Cu.

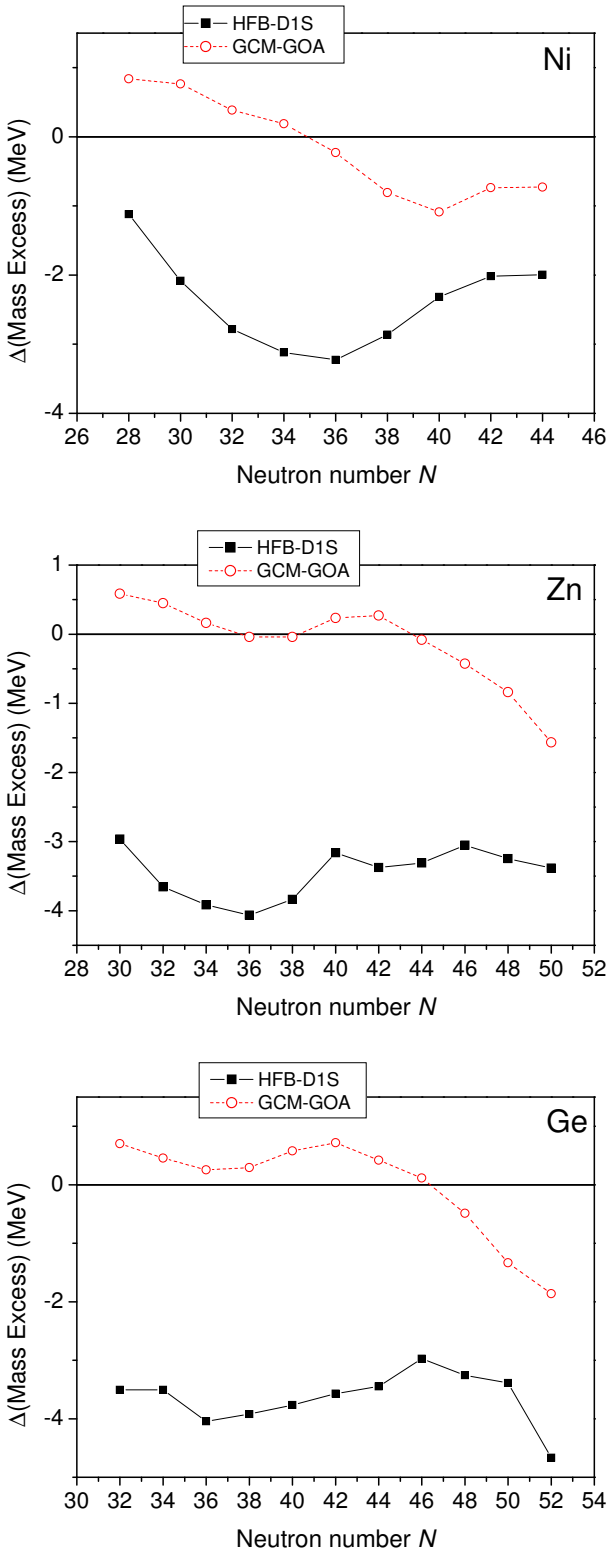

Figure 8.7: *Difference between the mass excess from the AME2003 table [3] (including many ISOLTRAP results) and theoretical predictions from HFB-D1S calculations corrected in different ways for Ni, Zn, and Ge isotopes. The GCM-GOA calculations are the closer from the experimental results.*

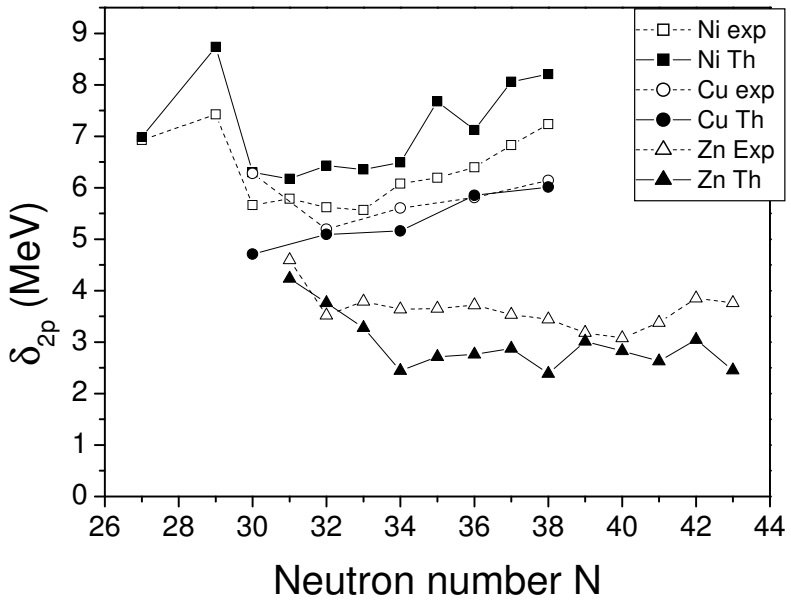

Figure 8.8: *Two-proton gap as a function of neutron number N for Ni, Cu, and Zn for experimental results [3] represented by dashed lines and empty boxes and HFB-D1S calculations with full symbols and solid lines. The trend is respected for the Cu and Ni isotopes.*

To compare more closely all these Gogny-force calculations to our experimental data and to see the variation as a function of the neutron number, the three-point pairing gap [158] which depends on the neutron number N variation may be used. It is defined by:

$$\Delta_3(N,Z) = \frac{(-1)^N}{2}\Big(B(N+1) - 2B(N) + B(N-1)\Big). \tag{8.7}$$

To avoid, in addition, the staggering effect, the four-point formula should be used:

$$\Delta_4(N,Z) = \frac{(-1)^N}{4}\Big(B(N+1) - 3B(N) + 3B(N-1) - B(N-2)\Big). \tag{8.8}$$

All these comparisons are presented in figure 8.9. It shows that the trends of the experimental results are relatively well represented by the theoretical calculations for Ni and Zn but there are big structures showing up, especially with the four-points formula. These differences are correlated with odd nuclides for which the ground state is difficult to predict especially for deformed nuclides[4]. Some more work is needed to repair these irregularities.

[4]For deformed nuclides the projection of the angular momentum onto the symmetry axis differs from the angular momentum.

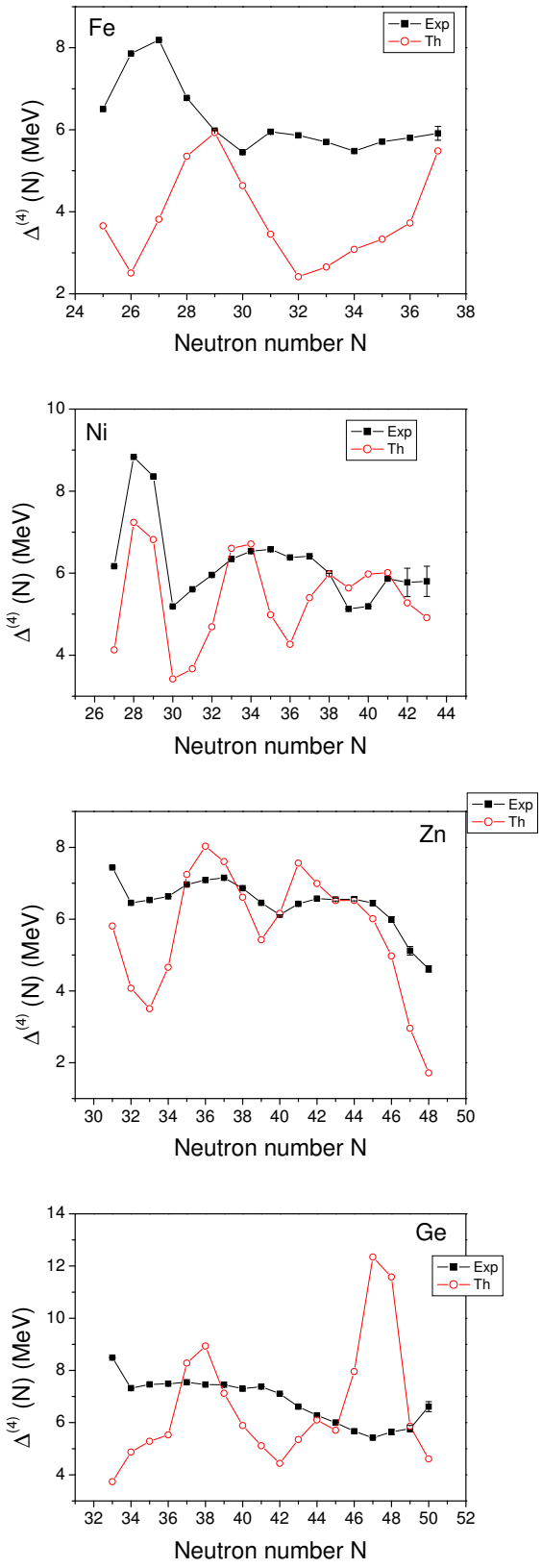

Figure 8.9: *Pairing gap $\Delta_4(N)$, defined in equation (8.8), for theoretical predictions from HFB-D1S calculations (empty circles), and experimental measurements represented by dashed lines and full squares . The trend is respected for Zn and Ni: only few deviations are observed.*

8.4.2 RMS deviation

The root-mean-square (rms)[5] deviation [2], which characterizes the predictive power of a model, is defined by

$$\sigma_{rms} = \sqrt{\sum_{i=1}^{i=N} (m^i_{exp} - m^i_{th})^2}, \tag{8.9}$$

where N is the number of experimental m_{exp} and theoretical m_{th} masses. The required value for σ_{rms} is 0. Table 8.4 shows the standard deviation σ_{rms} between masses measured by ISOLTRAP and predictions from the AME95 table [86] which does not yet include our ISOLTRAP results on Ni, Cu, and Ga, and from AME03 [3], which does include them. For the HFB models our measurements improve this value, but not for the Duflo-Zuker (DZ) mass formula from 1996 [9] while for FDRM there is no change. This is probably due to the fact that the DZ mass formula has been built to fit as much as possible the mass table having a large number of adjusted parameters.

The comparison of the σ_{rms} for different models is a clear demonstration of the improvement of the HFB calculations using a Skyrme force adjusted on the mass table: between HFB-2 and HFB-8. This also may show the power of the microscopic mass formula.

Table 8.4: *The standard deviation σ_{rms} (in MeV) for different models, between the two AME tables of 1995 and 2003 for nickel, copper, and gallium isotopes measured by ISOLTRAP.*

Nuclide	AME Table	DZ	FRDM	HFB-2	HFB-8
Ni,Cu,Ga	AME95	0.434	0.555	0.843	0.550
Ni,Cu,Ga	AME03	0.451	0.555	0.801	0.530
Ni	AME95	0.623	0.445	1.211	0.732
Ni	AME03	0.640	0.476	1.174	0.678
Cu	AME95	0.426	0.471	0.644	0.601
Cu	AME03	0.451	0.530	0.626	0.563
Ga	AME95	0.280	0.644	0.654	0.375
Ga	AME03	0.291	0.614	0.648	0.384

8.4.3 Comparison between experimental mass excess and theoretical predictions

The difference between the ISOLTRAP mass measurements and the mass values predicted by various models are presented in figure 8.10. These comparisons show that none of these models is predicting the mass excess value sufficiently well to achieve the needed accuracy on mass values, so high-precision mass measurements in this region are still needed. It is interesting to note the predictions of the unknown copper isotopes (^{72}Cu,

[5] More detailed explanations including errors can be found in [2].

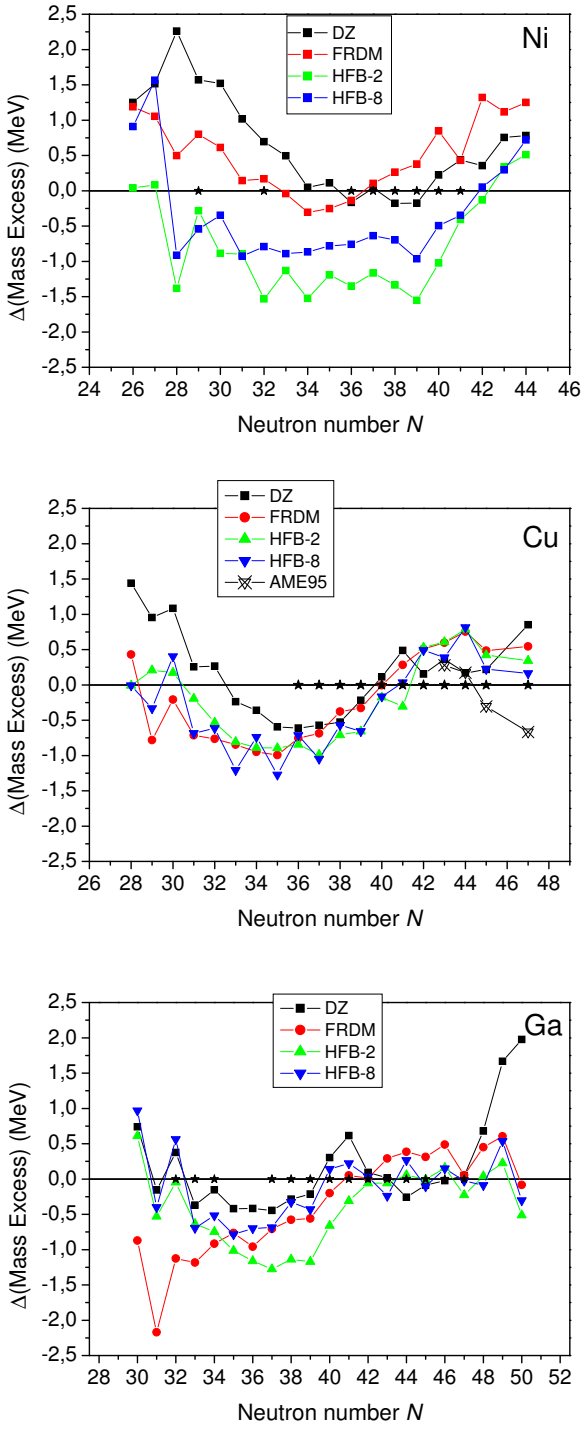

Figure 8.10: *Mass excess difference between different models for Ni, Cu, and Ga and ISOLTRAP measurements, represented by stars. ISOLTRAP measurements are completed with values coming from the AME03 table [3]. Values coming from systematic calculations presented in the AME95 [86] for copper are indicated. None of these models is predicting experimental results within errors.*

^{73}Cu, ^{74}Cu, and ^{76}Cu), estimated from systematic trends in AME95. In the detailed models comparison [2] the AME systematic values proved to be by far the most reliable. Here we see the deviations are comparable with all models.

The largest problem is with ^{56}Ni which is not only doubly magic but also a $N = Z$ nucleus (so-called Wigner nuclide). Here the spread of models exceeds 3.5 MeV. In the case of $N = 40$, the spread is largest for the Ni isotopes: ~ 2 MeV. This is to be compared to less than 1 MeV for Ga and 0.5 MeV for Cu.

8.5 Magic number studies

We analyze the effect of the high-precision mass measurements of ISOLTRAP on the mass surface in order to detect clues of magicity. To this purpose we compared the behavior of N=40 to magic numbers or to numbers located between two shell closures.

8.5.1 Study of the two-neutron separation energy

The two-neutron separation energy (S_{2n})

$$S_{2n}(N) = B(N,Z) - B(N-2,Z), \tag{8.10}$$

where B is the binding energy, is an indicator of shell structure and deformation. For example, in figure 1.1 around $N = 50$ we can clearly see the shell closure for the magic number $N = 50$.

The S_{2n} surface, in general, is remarkable for its regularity between shell closures. Generally, S_{2n} decreases smoothly with N and shell-structure effects appear as discontinuities. In the past, discontinuities of S_{2n} versus N were often traced to inaccurate Q_β endpoint measurements and measurements with more reliable, direct techniques would restore the regularity. This was part of the original intention for the ISOLTRAP mass measurements in the $N = 40$ region. Figure 8.11 presents the S_{2n} status, from $N = 36$ to 50, before and after ISOLTRAP measurements. However, our hypothesis seems not to be supported: most of the irregularities *e.g.* at $N = 41$ for Ga, are real. Moreover, the plot reveals a deviation from the linear trend between $N = 39$ and $N = 41$ for nickel and gallium. Also irregularities for Ga ($N = 46 - 49$) and Cu ($N = 43 - 46$) are visible.

To study the structure more closely we subtract a linear function of N determined by the S_{2n} slope preceding the purported shell closure. Is it presented in figure 8.12 in the region of $N = 82$ (for comparison) and $N = 40$. The $N = 82$ shell closure is clearly visible on this plot: there is a change of slope between $N = 82$ and $N = 84$. From these observations we can analyze the behavior in the $N = 40$ region: there is a similar effect between $N = 39$ and $N = 41$. From this, the trend break could be seen at $N = 39$ and not $N = 40$, which should be surprising for an odd number. The magnitude of this decrease is far smaller (between 500 keV and 1 MeV) than the one for $N = 82$ (around 4 MeV). A structure is seen between $N = 39$ and $N = 41$ but this is not an indication of shell closure, more work with theorists should be performed by using other observables in order to understand this behaviour. Moreover some accurate measurements should be done for Zn and Co isotopes in this region to confirm these observations.

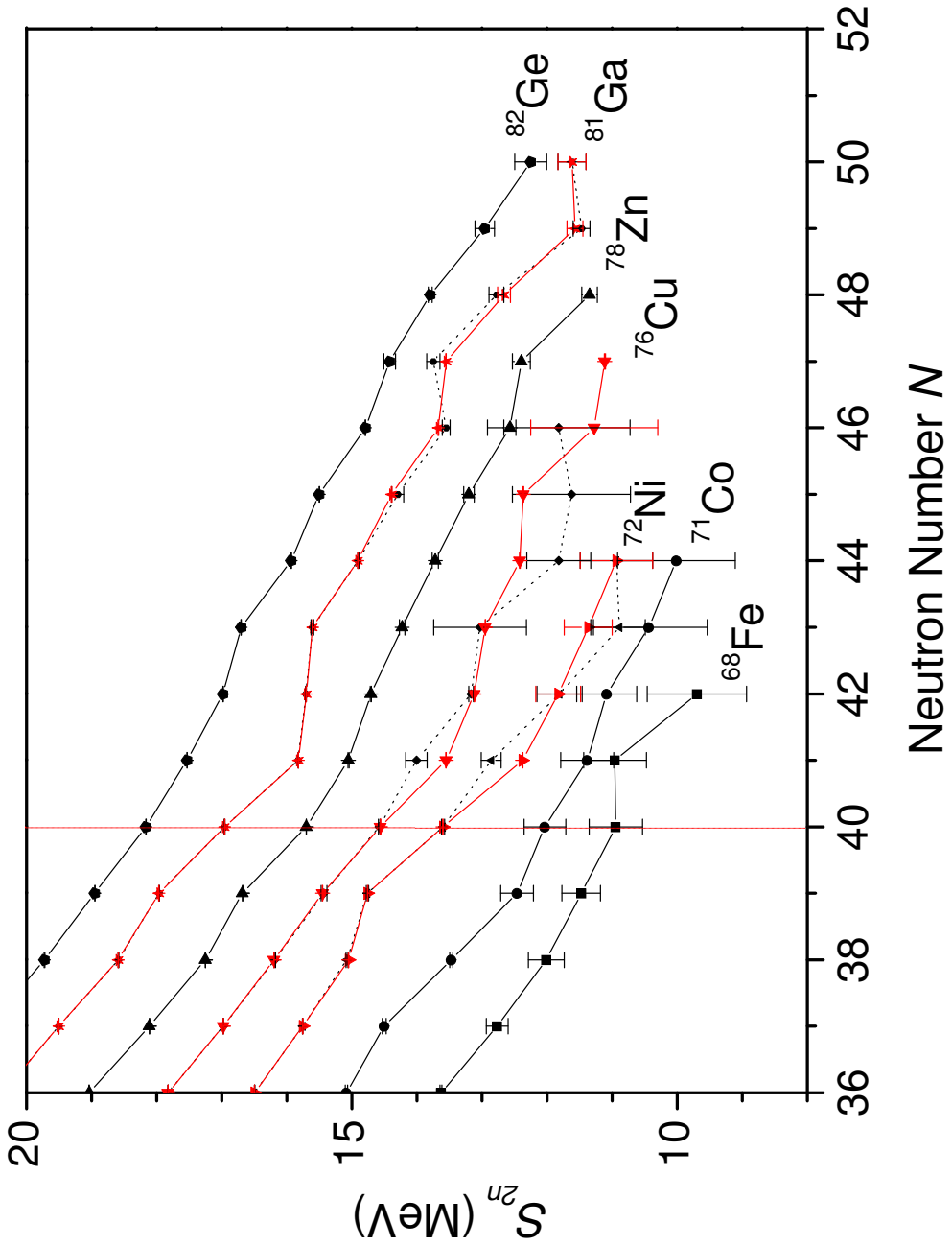

Figure 8.11: *Two-neutron separation energies (S_{2n}) around $N = 40$. Dashed lines correspond to the status of this region before the ISOLTRAP measurements. Points with large error bars were not measured by ISOLTRAP but their value was changed by the link to the measured masses.*

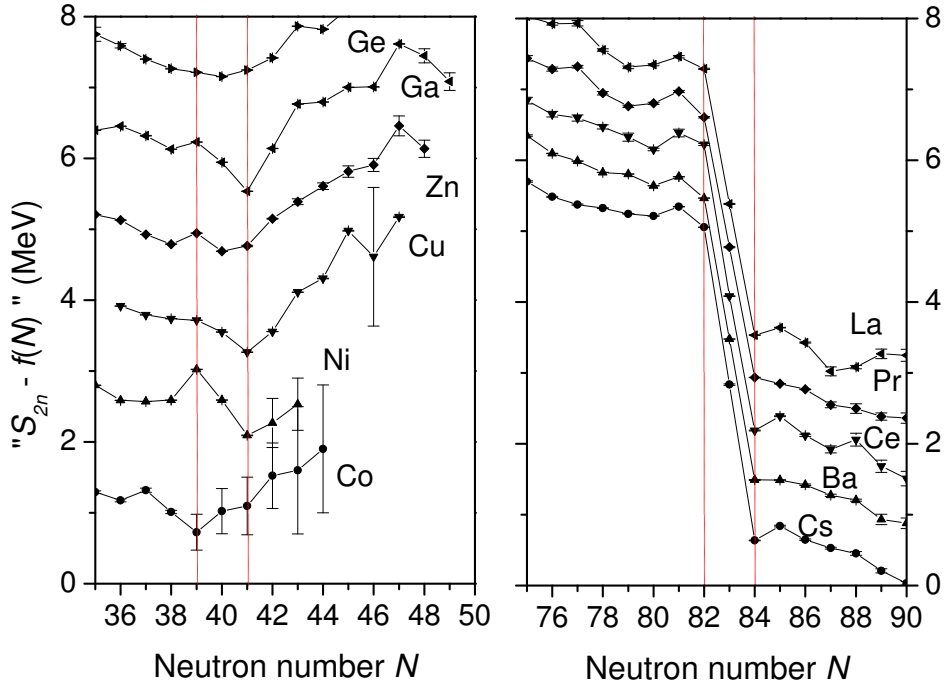

Figure 8.12: *Two-neutron separation energies (S_{2n}) minus a linear function of N around $N = 40$, and $N = 82$. The shell closure at $N = 82$ is clearly visible.*

8.5.2 The shell gap

Studying the neutron shell gap, defined as:

$$\Delta_N(N_0,Z) = S_{2n}(N_0,Z) - S_{2n}(N_0+2,Z), \tag{8.11}$$

is a convincing way to show how strong the shell effect is.

Normally the shell gap is a concept that is supposed to be valid only for spherical nuclides *i.e.* only around magic numbers. We have nonetheless looked to see how mid-shell gaps compare in strength and comportment in order to glean some information. Not surprisingly, the energies are quite small but there does seem to be an indication of the magic proton number $Z = 28$ for the $N = 40$ sub-shell gap (see figure 8.13). It highlights strong shell gap for magic neutron number with peaks at magic Z. It also shows that for $N = 50$ there is a peak at $Z = 39$, and not $Z = 40$, which is known to be semi-magic, this is due to the odd-even effect in the S_{2p} calculations.

In figure 8.14, the behavior of a strong shell closure is shown for $N = 82$ which is a magic number: there is a big difference between $N = 82$ and $N = 81$, 83 and the corresponding enhanced shell gap for the case of magic $Z = 50$. It also shows the behavior of a mid-shell $N = 66$ (exactly in between two shell closures: 50 and 82): the neutron shell gap for $N = 66$ is between the one for $N = 65$ and $N = 67$. For $N = 40$ a strong difference (like for $N = 82$) is not visible. Neither $N = 40$ is distinct from $N = 39$ and 41. A highlight is the fact that the neutron shell gap of $N = 39$ (mid shell of 28 and 50) is

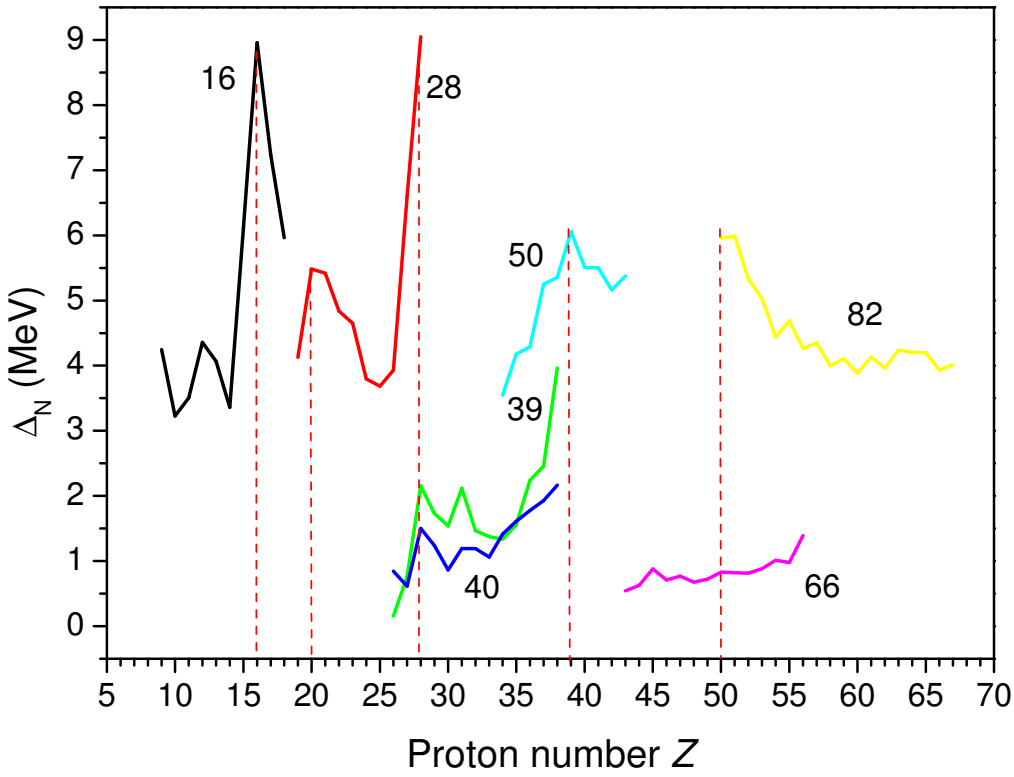

Figure 8.13: *Shell gap as a function of the proton number Z for different magic and mid-shell neutron numbers N. N=16, 28, 50, 82 are shell closures, $N = 39$ and 66 are exactly between two shell closures (called mid-shell), $N = 40$ is under investigation.*

higher than those of $N = 38$ and 40 for several values of Z, specially for $Z = 28$, which is exactly the contrary of a-mid-shell behavior. It highlights that the Δ_N of $N = 40$ has the behavior of a Δ_N of mid-shell like $N = 66$. While the Δ_N of $N = 39$, which is mid-shell has a small kind of behavior of a Δ_N of shell closure like $N = 82$. This shows that $N = 38$, 39, and 40 do not have the behavior we could have expected. This leads to the conclusion that there is no shell closure at $N = 40$, and that more studies should be done in this region to understand what it is happening.

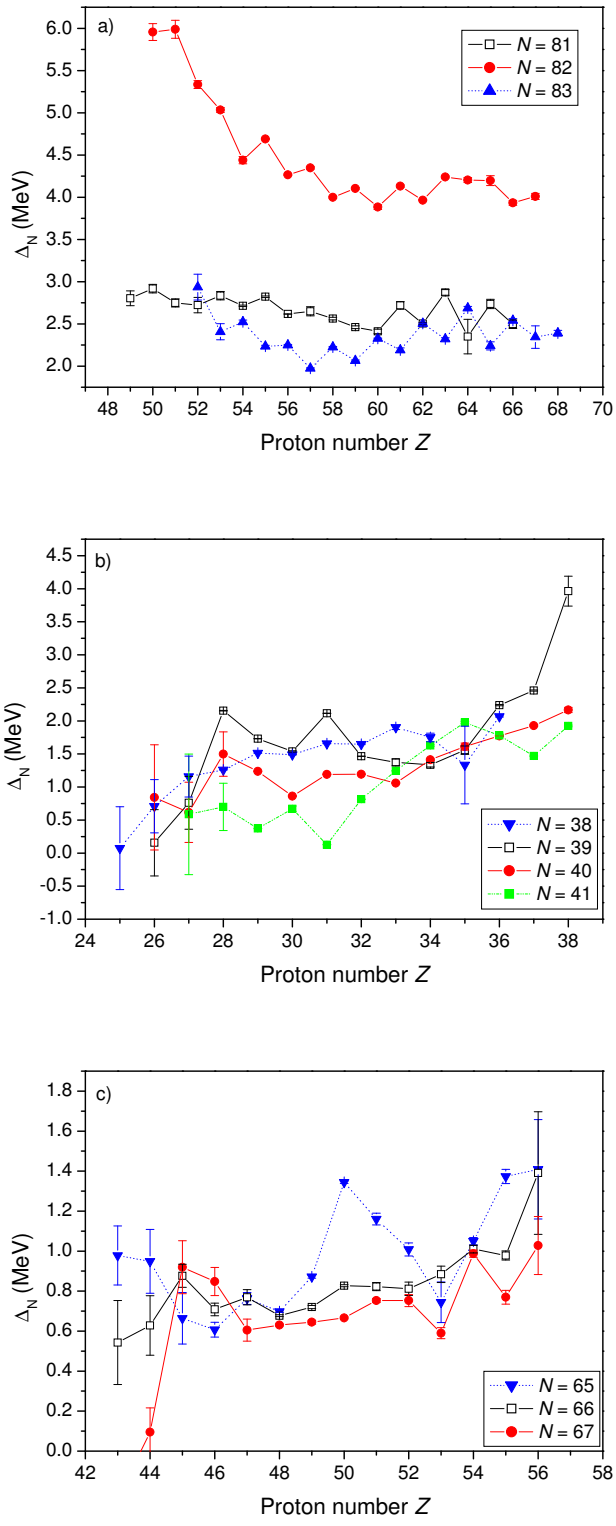

Figure 8.14: *Shell gap as a function of the proton number Z for a) $N = 81 - 83$ with the N=82 magic number well distinguished from N=81 and 83, b) $N = 38 - 41$, and c) $N = 65 - 67$ with N=66 representing a mid-shell number in between N=65 and 67.*

8.5.3 The pairing gap energy

The pairing gap energy from the four-point formula $\Delta_4(N)$, as defined in eq. (8.8), was chosen to study the pairing correlations.

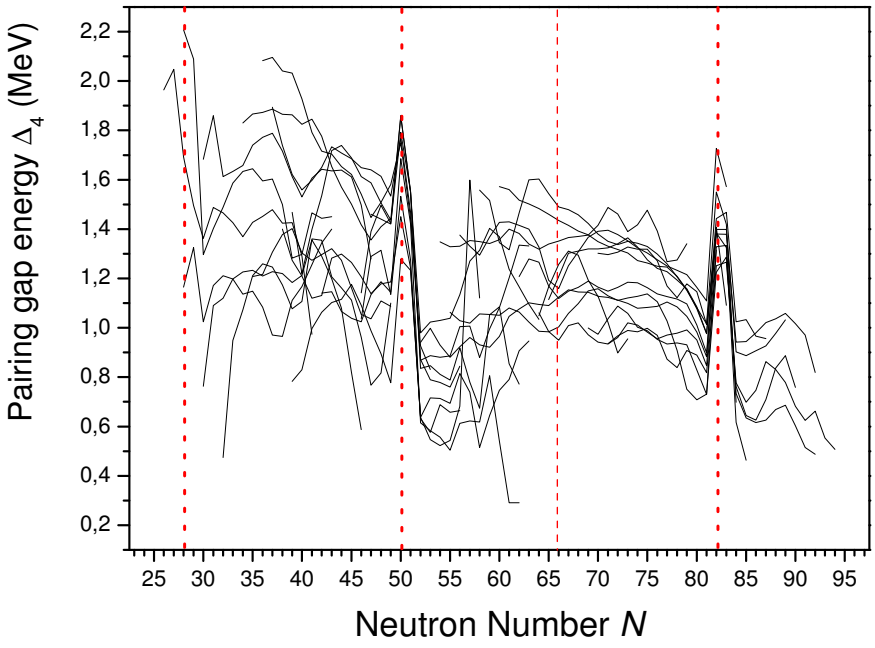

Figure 8.15: *Pairing gap energy as a function of neutron number for $Z = 27 - 59$. Shell closures at N=28, 50, and 82 are clearly visible.*

The pairing gap energy as a function of neutron number is represented in figure 8.15 for $Z = 27$ to 59. Shell closures at 50 and 82 are clearly visible. At $N = 39$ (mid-shell: exactly in between two shell-closures: 28 and 50) there is a slight trough (see figure 8.16) for $Z = 27$ and 31 - but not for $Z = 29$. A similar behavior is seen at $N = 66$ (mid-shell of 50 and 82). Both cases correspond to mid-shells. This figure does not confirm the sub-shell closure around $N = 39$ but more the mid-shell behavior. This raises a question: could we have a competition between sub-shell closures and mid-shell? This question should be discussed with theorists.

8.5.4 Comparison with the "Bethe and Weiszäcker formula"

The idea here is to try to get a "neutral" indication as to any shell effect at $N = 40$. The original Bethe-Weizsäcker mass formula contained no specific term for shell effects since they were unknown at that time. Subtracting the Weiszäcker formula (eq. (8.1)) from known masses reveals this rather dramatically (see figure 8.17).

The difference between the experimental values and the formula, presented in figure 8.17, shows clearly the shell closures: $N = 28$, 50, 82, 126, with especially strong

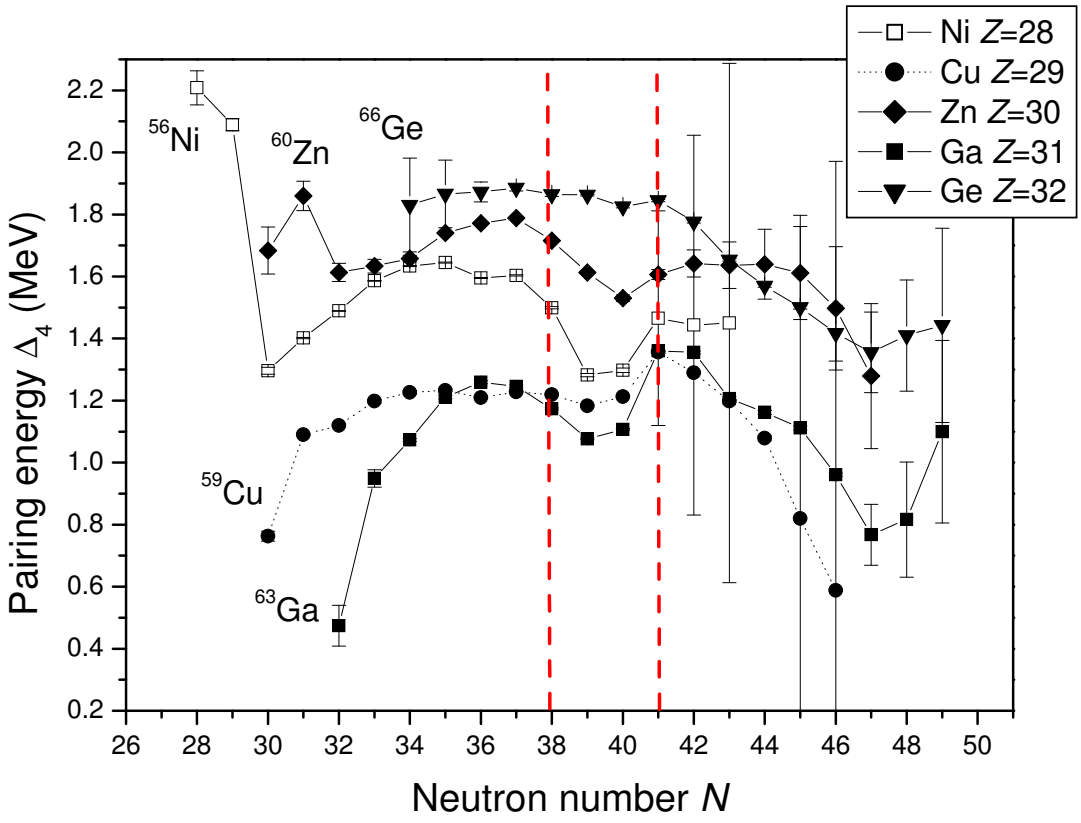

Figure 8.16: *Pairing energy as a function of neutron number for the investigated elements. There is no indication of magicity at N=40.*

effects ($\sim$ 15 MeV) for nuclides with $N = 50$ and $N = 82$. Figure 8.18 is the representation of this difference around $N = 40$, used to see if there is a sign for shell closure for the three isotopic chains of Cu, Ni, and Ga between the known shell closures at $N = 28$ and $N = 50$. The difference is less for $N = 28$ but still above 7 MeV. Between the shell closures the mass differences follow a smooth inverted parabola. However, between $N = 38$ and 41 a small indentation is apparent for Ni and Ga, which should be explained.

In figure 8.19, there is a comparison of the behavior of the magic neutron number and $N = 40$ as a function of proton number. For the magic number $N = 50$, there is a small decrease for $Z = 39$ or 40. The other point is that for $N = 40$ there is a significant dip for the magic $Z = 28$. The conclusion on the Bethe and Weiszäcker study is that there is some structure in this region, especially around $N = 39 - 40$, but no clear conclusions can be drawn.

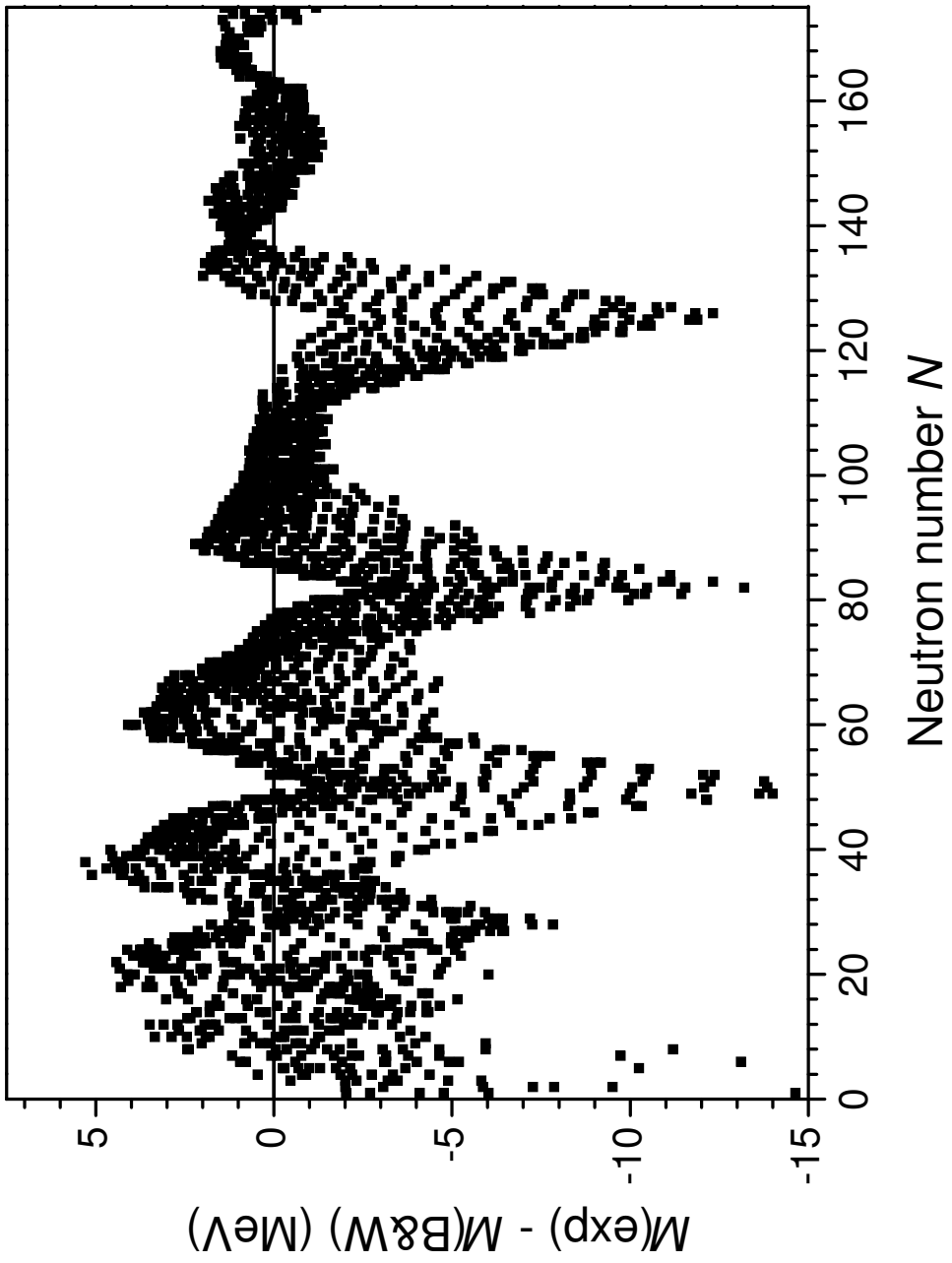

Figure 8.17: *Difference between the predicted masses by the Bethe-Weizsäcker formula (Eq. 8.1) and the experimental values [3].*

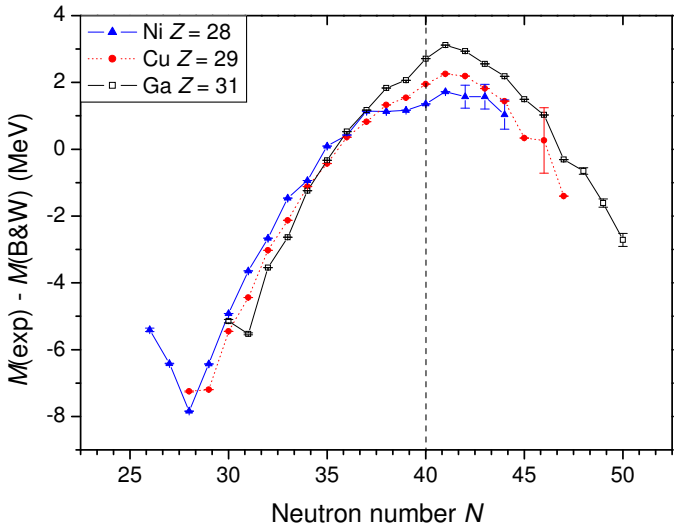

Figure 8.18: *Difference between the masses predicted by the Bethe-Weizsäcker formula (Eq. 8.1) and the experimental values as a function of N for Z = 28, 29, and 31. Data are from this work and complemented by [3].*

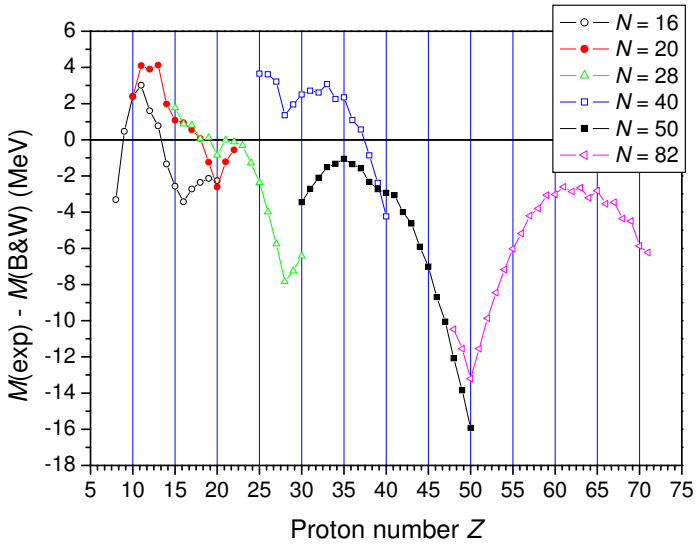

Figure 8.19: *Difference between the experimental mass measurements and theoretical masses from the "Bethe and Weizsäcker formula" as a function of proton number, for magic neutron numbers.*

8.5.5 Isospin

This comparison is done after the fashion of studies by Ozawa *et al.* [159], and Kanugo *et al.* [160] on isospin which is defined by $T_Z = (Z-N)/2$. For the "standard" case of $N = 82$ (figure 8.20a), we can see the behavior of S_n for a magic neutron number: there is a decrease of S_n, for any value of T_Z. For $N = 40$ (figure 8.20b), we do not have a big decrease, but only small structures around $N = 40$. This isospin study shows only small structures: no indication of magicity was found around $N = 40$.

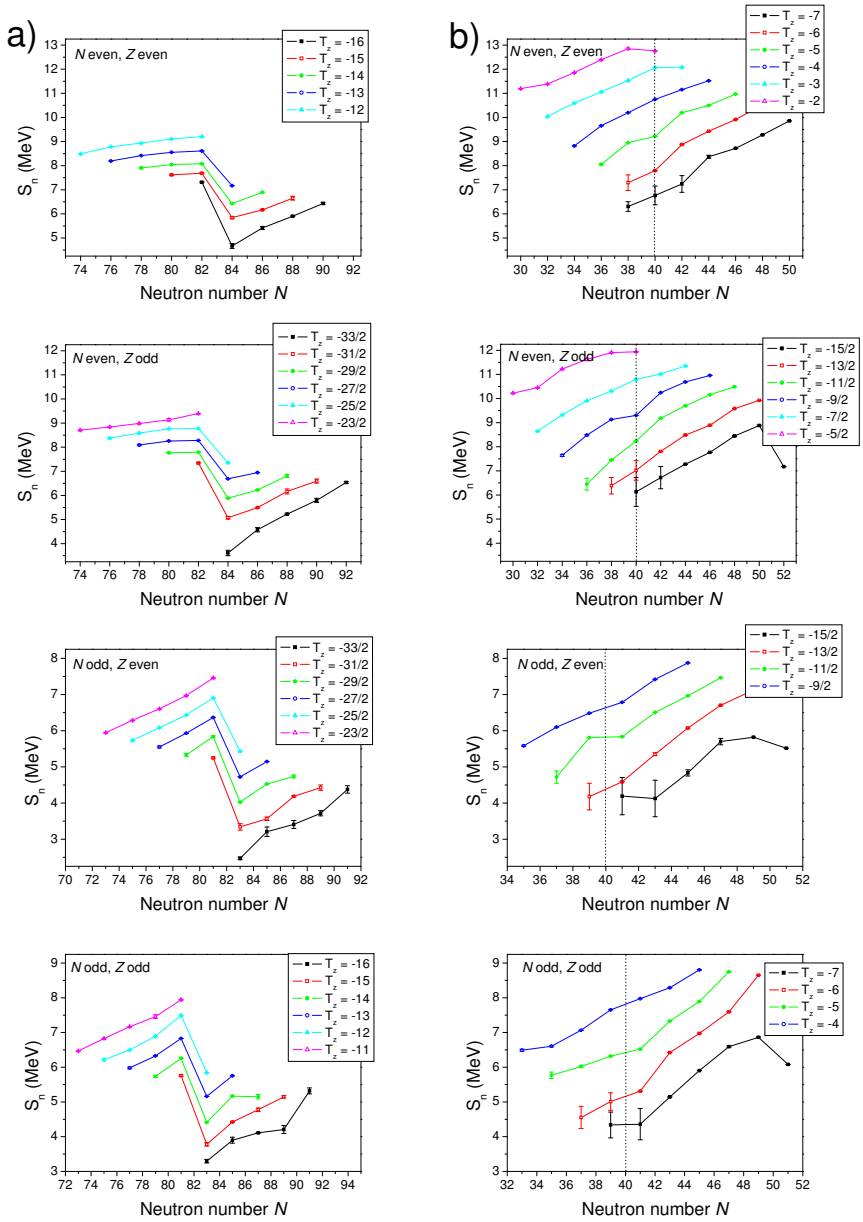

Figure 8.20: *Separation energy of one neutron S_n as a function of the neutron number for different isospin values: a) around $N = 82$, b) around $N = 40$, where there is no evidence for magicity.*

8.5.6 Conclusion regarding N=40

Thanks to the results presented here, the mass surface for neutron-rich nuclides around $N = 40$ has now been finely mapped and the binding energies reflect nothing that could be considered a magic number. In the analog case of $Z = 40$, the $N = 56$ sub-shell closure is visible on the mass surface (see figure 1.1). As much as an $N = 40$ ($d_{5/2}$) sub-shell could exist, there is even no indication for such a sub-shell closure from these measurements. Studies of the new mass surface were performed exploiting its newfound smoothness to look at derivatives.

While the pairing gap energy clearly indicates that there is nothing like a shell closure in this region, it may indicate a competing mid-shell stabilization effect. The study of the isospin as well as the comparison with the Bethe and Weiszäcker formula indicate some fine structure around $N = 39, 40$ but no indication of the presence of a shell closure. The more interesting result is coming from the shell gap which shows astonishing behavior for $N = 39$ as well as for $N = 40$, maybe due to the competition between 38-40 and 39. This result could be a good starting point for theorists to understand what this non-(sub)-shell closure might be.

As stated by Bohr and Mottelson [4], cited at the beginning of this chapter, we should see the effect of a shell closure by using binding energies. However if we continue and cite the totality of their remarks: «... it [is] relatively difficult to discern the nuclear shell structure as long as the main information on nuclei [is] confined to binding energies.» Thus, we are forced to admit that while binding energy is a necessary ingredient, it is far from sufficient for explaining the problem at hand and is in opposition with results on the $B(E2)$ [126].Thus, more detailed spectroscopy measurements, included the $g-$factor, as suggested by Langanke *et al.*, and, of course, more theoretical work, are called for to understand the various phenomena arising from mass surface studies.

Conclusion

ISOLTRAP now provides the most accurate mass measurements of exotic nuclides. Such accuracy allows us to provide smooth mass surface derivatives (*e.g.* shell gaps, pairing gaps) that can be examined in minute detail for deviations caused by nuclear structure effects. But to achieve such accurate and precise measurements, a perfect optimization of the setup was necessary, and especially in the Penning trap used for the measurement. The procedure on this optimization was developed and is now applied systematically every year and can be extended to other setups using traps.

ISOLTRAP also allowed to extend the so-called "backbone" of very well known nuclides in the atomic mass evaluation table. Strengthening the backbone inherently improves accuracy over the entire mass table.

The nature of $N = 32$ was investigated with mass measurements on chromium isotopes and was found to be a non-magic number but a region of deformation. More measurements on most exotic nuclides should be confirmed to definitely conclude on $N = 32$.

The nature of $N = 40$ is still an open question, with conflicting experimental evidence. The high-precision mass measurements performed at ISOLTRAP of over 30 short-lived neutron rich isotopes of Ni, Cu, and Ga presented in this dissertation bring some clarification to the situation in this region: there is some structure on the mass surface around $N = 40$, but our measurements definitively rule out the magicity. The question clearly needs additional input from theorists and physicists, and especially more spectroscopy should be done to understand the level configuration of the nuclides involved in this supposed sub-shell.

ISOLTRAP's limitation is the half-life of the nuclides it can measure. To complement this shortcoming, the MISTRAL mass spectrometer is used to measure very-short lived nuclides, but its transmission was limited to 10^{-4}, insufficient for measuring these nuclides, produced with a very small yield. COLETTE, an ion beam cooler, was developed to solve this problem by decreasing the beam emittance. The performance of COLETTE was demonstrated and it is now installed before the MISTRAL spectrometer in CERN. The first tests are encouraging.

This allows, in the future, the possibility to continue MISTRAL measurements on short lived nuclides like ^{14}Be (4.5 ms), interesting for halos studies. Around $N = 40$ further from the stability, ^{63}V (17 ms) and ^{64}Cr (43 ms) would be very interesting candidates.

ISOLTRAP's accuracy combined with its excellent sensitivity will continue to provide new mass data far from stability, of crucial importance for constraining mass models and predicting limits of bound nuclear systems.

Appendixes

Appendix A

Complementary studies on the optimization

The optimization procedure has been performed since several years, but it has never been reported. Here are presented the complementary studies used to perform this optimization. The first part presents the approximation on which is performed the electric field optimization. Then the influence of the temporal variation of the magnetic field on the optimization measurements is described. Different optimization parameters were tried: another optimization electrode and another frequency measurement, which are the "third correction tube" and the ω_z frequency. Finally the stabilization time needed during the optimization is shown.

A.1 Reduced cyclotron frequency

Here is the demonstration of the approximation: $\nu_+ = \nu_c - \frac{V_0}{4\pi B d^2}$.

$$2\nu_+ = \nu_c + \sqrt{\nu_c^2 - 2\nu_z^2}\,(\text{see eq. (2.26)}) \tag{A.1}$$

$$2\nu_+ = \nu_c + \nu_c \cdot \sqrt{1 - \frac{2\nu_z^2}{\nu_c^2}} \tag{A.2}$$

$$\nu_z \ll \nu_c, \text{ so } \frac{\nu_z}{\nu_c} \ll 1 \text{ and consequently } \sqrt{1 - \frac{2\nu_z^2}{\nu_c^2}} \sim 1 - \frac{1}{2} \cdot \frac{2\nu_z^2}{\nu_c^2} \tag{A.3}$$

$$\text{So } 2\nu_+ \sim \nu_c + \nu_c \cdot (1 - \frac{\nu_z^2}{\nu_c^2}) \tag{A.4}$$

$$\nu_+ \sim \nu_c - \frac{\nu_z^2}{2\nu_c}, \text{ with } \nu_z^2 = \frac{1}{(2\pi)^2}\frac{2qV_0}{m\rho_0^2}, \text{ and } \nu_c = \frac{qB}{2\pi m}, \tag{A.5}$$

$$\text{with } 2d^2 = \rho_0^2,\ \nu_+ \sim \nu_c - \frac{V_0}{4\pi B d^2}. \tag{A.6}$$

A.2 Magnetic field drift

The magnetic field is changing as a function of time. Thus, to perform high precision mass measurements ISOLTRAP is using a reference ion source to calibrate the magnetic field strength, *i.e.* to measure the ratio between the "unknown" mass and a well-known mass.

For the studies presented before, this problem of field drifting had to be avoided. In order to do so we performed reference measurements before and after each measurement, the procedure of which is described in the following.

A.2.1 Influence of the magnetic field drift on the magnetic field measurement

- At t_0, $T_{\text{cap}} = T_{\text{cap},0}$: $\omega_{c,0} = \frac{qB_0}{m}$
- At t_1, $T_{\text{cap}} = T_{\text{cap},1}$: $\omega_{c,1} = \frac{q(B_1+\Delta(B_1))}{m}$
- At t_2, $T_{\text{cap}} = T_{\text{cap},0}$: $\omega_{c,2} = \frac{q(B_0+\Delta(B_2))}{m}$

The difference between B_0 and B_1 is due to the variation of the capture timing from $T_{\text{cap},0}$ and $T_{\text{cap},1}$, while $\Delta(B_1)$ and $\Delta(B_2)$ are due to the drift of the magnetic field. We assume that during a short period (less than 3 hours) the drift is linear (see figure A.1).

Consequently, $\Delta(B_1) = \Delta(B_2)\frac{t_1-t_0}{t_2-t_0}$, with $\Delta(B_2) = \frac{m}{q}(\omega_{c,2} - \omega_{c,0})$.

And $\omega_{c,1}^{True} = \frac{qB_1}{m}$, while $\omega_{c,1}^{Mes.} = \frac{q(B_1+\Delta(B_1))}{m}$, so $\omega_{c,1}^{True} = \omega_{c,1}^{Mes.} - \frac{\Delta(B_1)}{m}$.

All the optimization results are based on $\omega_{c,n}^{True}$, so each measurement should be done in between two measurements of ω_c at a fixed T_{cap} (in general the optimum one).

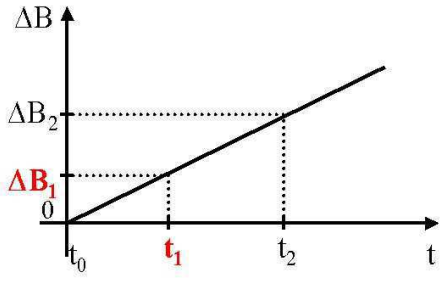

Figure A.1: *Variation of ΔB as a function of time t.*

A.2.2 Influence of the magnetic field drift on the electric field measurement

- At t_0, $T_{\text{cap}=T_{cap,0}}$: $\omega_{+,0} \simeq \frac{qB_0}{m} - \frac{V_0}{2B_0d^2}$

- At t_1, $T_{\text{cap}} = T_{\text{cap},1}$: $\omega_{+,1} \simeq \frac{q(B_0+\Delta(B_1))}{m} - \frac{V_0}{2(B_1+\Delta(B_1))d^2}$
- At t_2, $T_{\text{cap}} = T_{\text{cap},0}$: $\omega_{+,2} \simeq \frac{q(B_0+\Delta(B_2))}{m} - \frac{V_0}{2(B_0+\Delta(B_2))d^2}$

Relation between $\omega_{+,1}^{True}$ and $\omega_{+,1}^{Mes}$:

$$\begin{aligned}
\omega_{+,1}^{True} &\simeq \frac{qB_0}{m} - \frac{V_1}{2B_0d^2} \\
\omega_{+,1}^{Mes} &\simeq \frac{q(B_0+\Delta(B_1))}{m} - \frac{V_0}{2(B_1+\Delta(B_1))d^2} = \frac{qB_0}{m} + \frac{q\Delta B_1}{m} - \frac{V_1}{2B_0d^2}\frac{1}{1+\frac{\Delta B_1}{B_0}} \\
\frac{\Delta B_1}{B_0} &\ll 1 \text{ , so } \frac{1}{1+\frac{\Delta B_1}{B_0}} = 1 - \frac{\Delta B_1}{B_0} + \frac{\Delta B_1}{B_0}\varepsilon(\frac{\Delta B_1}{B_0}), \text{ with } \varepsilon(\frac{\Delta B_1}{B_0}) \ll 1
\end{aligned}$$

$$\begin{aligned}
\omega_{+,1}^{Mes} &= \frac{qB_0}{m} + \frac{q\Delta B_1}{m} - \frac{V_1}{2B_0d^2}(1 - \frac{\Delta B_1}{B_0} + \frac{\Delta B_1}{B_0}\varepsilon(\frac{\Delta B_1}{B_0})) \\
&= \frac{qB_0}{m} - \frac{V_1}{2B_0d^2} + \frac{q\Delta B_1}{m} + \frac{V_1}{2d^2} * [\frac{\Delta B_1}{B_0^2} + \frac{\Delta B_1}{B_0^2}\varepsilon(\frac{\Delta B_1}{B_0})]
\end{aligned}$$

The last term is negligible to first order, and

$$\frac{qB_0}{m} - \frac{V_1}{2B_0d^2} = \omega_{+,1}^{True}.$$

$$\text{So } \omega_{+,1}^{Mes} \simeq \omega_{+,1}^{True} + \frac{q\Delta B_1}{m}$$

$$\text{And } \omega_{+,1}^{True} \simeq \omega_{+,1}^{Mes} - \frac{q\Delta B_1}{m}$$

Remark:
To find ΔB_1, ω_c has to be measured: $\Delta(B_1) = \Delta(B_2)\frac{t_1-t_0}{t_2-t_0}$, with $\Delta(B_2) = \frac{m}{q}(\omega_c^2 - \omega_c^0)$.

So a measurement of ω_+ should be performed between two measurements of ω_c at a fixed T_{cap} (in general the optimum one).

A.3 The influence of the third correction tube

There is another correction electrode, which is a correction tube. It is located after the upper correction tube, and it should also correct the non-quadratic part of the electric field, but since it is far away from the trap the influence is small: more than 60 times less, compared to the correction tubes discussed in Chapter 5.

A.4 Use of ν_z

The electric field optimization is done by using the reduced cyclotron frequency ν_+ , defined by $\nu_+ = \frac{\nu_c}{2} + \sqrt{\frac{\nu_c^2}{4} - \frac{\nu_z^2}{2}}$, with $\nu_c = \frac{qB}{2\pi m}$ and $\nu_z = \sqrt{\frac{qV_0}{md^2}}$.

So ν_+ is related to the electric field and to the magnetic field; consequently the measurement of ν_+ will be dependent on the magnetic field: we should do first the optimization of the magnetic field and one has to use reference measurements to consider the drift of the magnetic field along the time.
A solution to avoid this problem is to use the ν_z frequency for the optimization since it is only related to the electric field, so the influence of the correction tubes will be directly linked to this ν_z . The problem is that the trap is not well suited to perform such a measurement, a resonance is very hard to get. Moreover the value of ν_z is almost 25 smaller than ν_+ , so the corresponding relative precision is smaller.

A.4.1 Stabilization time

Any change on the value of the shim-coil current should be followed by a stabilization time of at least three hours, as shown in figure A.2.

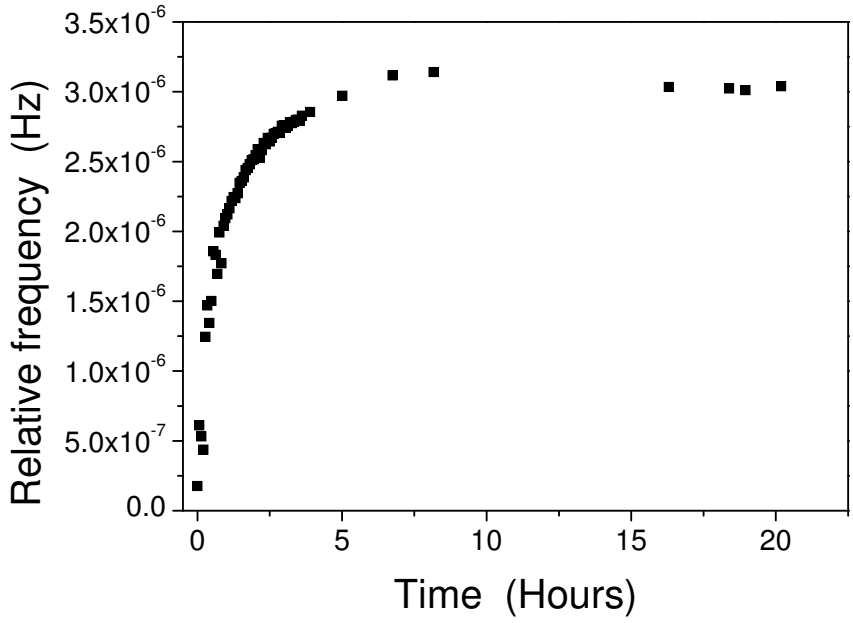

Figure A.2: *Needs of a stabilization time: after more than 5 hours the magnetic field is stabilized, the value of the shim-coil current was changed from 100 mA to 350 mA.*

Appendix B

Systematic measurements on ^{85}Rb

To do a measurement we need a reference file before and after each measurement. During the two beam times, when measurements described in Part III were performed, most of the time ^{85}Rb was taken as reference. So along all these beam times we performed more than eighty measurements of ^{85}Rb. I performed a detailed analysis of all these files and I compare the results.

Moreover a careful check of these reference files was performed in order to determine if they were usable as reference (enough statistics, no external perturbations, ...).

B.1 Frequency variation

Figure B.1 presents the variation of cyclotron frequency of the ^{85}Rb and the corresponding magnetic field during the two beam times.

A linear fit of the variation of the magnetic field B (in Tesla) as a function of the time T (in days) gives:

$$B = -2.68(9) \cdot 10^{-7} * T + 5.92$$

This confirms the value of the magnetic field $B \sim 5.9T$. Then, the relative variation is below $2.7 \cdot 10^{-7}$ T/day. A precedent study of this magnetic field [82] measured a relative variation of $\frac{\delta B}{\delta t}\frac{1}{B} = -2.30(3) \cdot 10^{-8}$/h, here we found $-4.53 \cdot 10^{-8}$/days. The difference is due to the fact that our study was only performed over 13 days, the previous one was done over more than 40 days. More investigations are ongoing to understand this big difference.

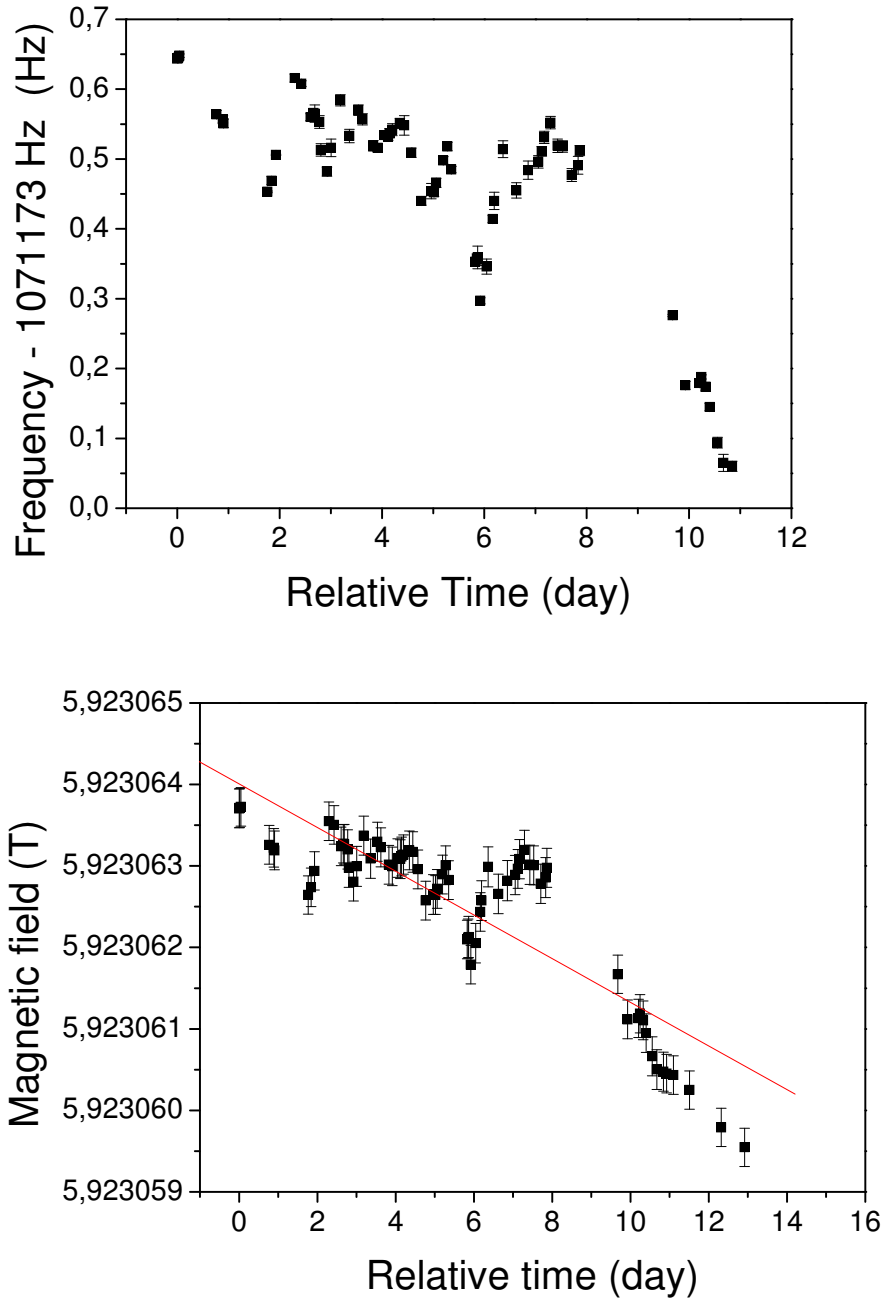

Figure B.1: *Top: Cyclotron frequency of the ^{85}Rb as a function of the recording time. Bottom: Corresponding magnetic field as a function of the recording time.*

B.2 Z-class analysis

The Z-class analysis is a procedure used in the ISOLTRAP analysis to check if some contaminant ions were in the trap during the measurement, and to check their influence on the measurement. A contaminant ion, different from the ion we want to measure, may interact with the ion of interest and change its frequency, and so produce a perturbation in the mass measurement.

Practically, measurements are separated as a function of the number of ions counted in one scan, then are divided in 3 or 4 bins (called "Z-class" in ISOLTRAP analysis) classed as a function of the number of ions, with approximatively the same number of ions in each bin. Then the frequency is calculated for each bin and a linear fit of the frequency as a function of the number of ions is performed, the slope of this fit gives an indication on the contamination.

Indeed, if there are contaminants, the probability of interaction of the ions of interest with the contaminants is bigger when the number of ions in the trap is higher. So for a high number of ions there is an interaction and so a frequency shift, consequently the slope of the linear fit is different from zero.

The ^{85}Rb ions were produced from the ISOLTRAP ion source, so no contaminants should be found. A check was performed that the slope of the linear fit of the frequency as a function of the number of ions is equal to zero. This is presented in figure B.2, the mean value for the slope is $5 \cdot 10^{-4} \pm 2 \cdot 10^{-3}\text{Hz}^{-1}$, which confirms that there is no contamination from our ion source on mass 85. Another confirmation is presented in figure B.3 which shows the difference between the mean frequency calculated by a Z-class analysis and the frequency calculated "normally". The difference is 0.004 ± 0.02Hz, which leads to a relative variation of $\frac{\Delta\nu}{\nu} = (3 \pm 15) \cdot 10^{-9}$. This means that there is no variation, which is another confirmation that there is no contamination from our ion source on mass 85

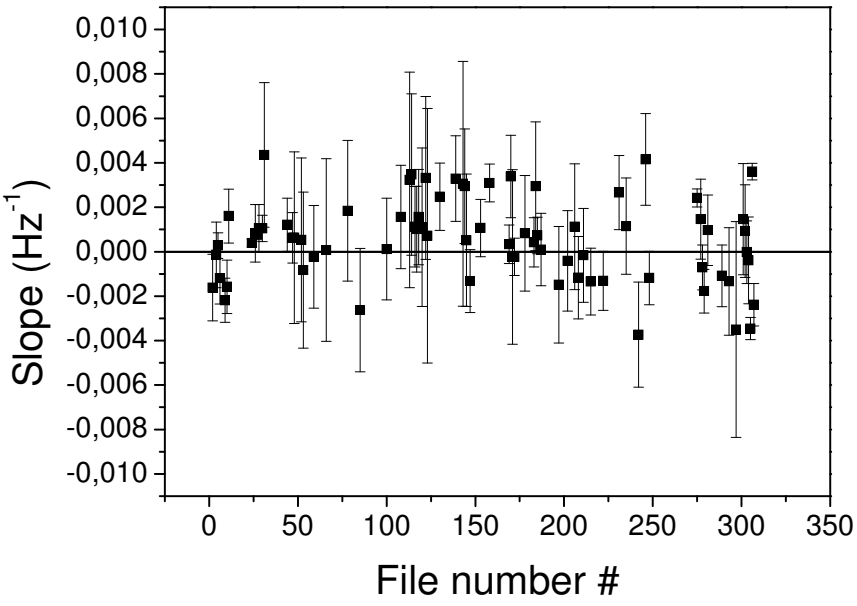

Figure B.2: *Slope coming from the Z-class analysis as a function of the file number. The mean slope is zero.*

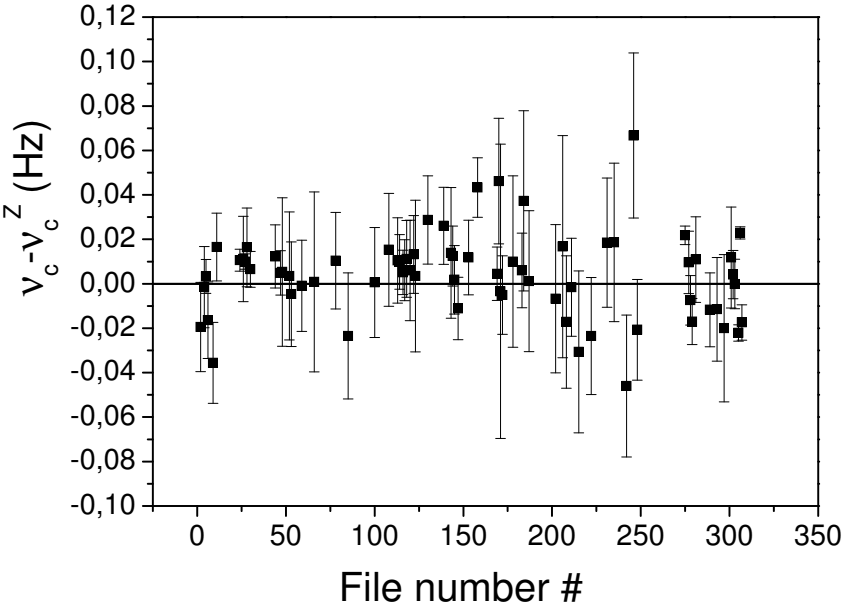

Figure B.3: *Difference between the frequency with and without Z-class analysis. The mean difference is zero.*

B.3 TOF resonance

From the fit performed on each TOF resonance, several trapping parameters are determined. The theoretical function used for the fit is:

$$TOF(\omega_{RF}) = \int_{z=0}^{z_{detector}} \sqrt{\frac{m}{2\Big(E_0 - q\cdot V(z) - \mu(\omega_{RF})\cdot B(z)\Big)}}\,\mathrm{d}z, \tag{B.1}$$

with E_0 the initial energy of the ions when they exit the trap.

We checked the evolution of all these trapping parameters over the total beam time. The influence of these parameters on the fit curve was studied and presented in [64]. The table hereafter presents mean values obtained with our systematic measurements.

Parameter	Mean Value	Deviation
E_z	0.012 eV	0.006 eV
E_{conv}	0.25 eV	0.006 eV
ρ_-	0.62 mm	0.17 mm
Conversion	1.02	0.03
Damping	0.37 s^{-1}	0.22 s^{-1}
χ^2	1.2	0.6

E_z is the initial axial energy of the ions at the upper correction tube, its variation is presented in figure B.4, here we found E_z=12 meV.

E_{conv} is the axial energy of the ion at the entrance of the second drift tube which is located after the first drift tube, which is just after the upper correction tube. It is presented in figure B.5. Points circled represent measurements performed after a change in the extraction upper trap (on the drift tubes). Without these points the mean value is found to be 0.250 eV.

ρ_- is the magnetron radius before the quadrupolar excitation in the precision Penning trap. Its measurement is presented in figure B.6. The mean value is in good agreement with typical values: $0.6 - 0.8$ mm.

The conversion factor is the number of conversions of the two radial motions, and should be equal to unity. This is in good agreement with what we found (see figure B.7).

The Damping factor is the damping due to collisions with the residual gas in the precision trap. Its definition [38] applied for the damping in a buffer gas is

$$\delta = \frac{q}{m}\frac{1}{M_{ion}}\frac{(p/p_N)}{T/T_N},$$

where p is the gas pressure (in fractions of the normal pressure p_N), T the temperature of the gas (in fractions of the normal temperature T_N), and M_{ion} the reduced ion mobility which for low ion velocities depends only on the ion species and the type of buffer gas.

χ^2 here is the reduced χ^2 which is a statistic value giving information on the validity of a fit.

$$\chi^2 = \frac{1}{N}\sum_{i=1}^{N}\Big(\frac{y_i - f(x_i,a,b)}{\sigma_i}\Big)^2,$$

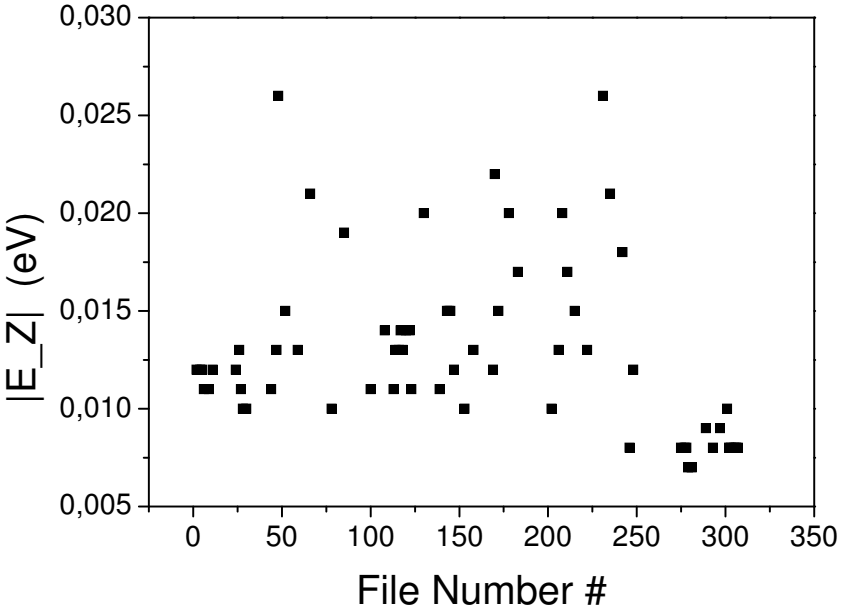

Figure B.4: *Absolute value of E_z as a function of the file number.*

with N measurements given by y_i (the frequency in our case), with an associated σ_i, and $f(x_i, a, b)$ the function represented by the fit. The value for this reduced χ^2 should be unity and values indeed scatter around this value (see figure B.9). When the value is higher than one the systematic uncertainty was underestimated, on the contrary when it is below one the uncertainty was overestimated. Files with high χ^2 were not used as reference.

The TOF effect represents the relative difference between the time of flight of ions located at the resonance (excited with the correct $\nu_{RF} = \nu_c$) and ions plotted in the base line (not excited at the good frequency). Ideally it should be 100%, but practically a value of 50% is considered as good. It is presented in figure B.10. The file 171 was a test of the setup. During this measurement some trapping parameters were changed, so this file was not used as a reference. Its evolution with time is due to the change of trapping parameters along the total beam time.

All these studies show the importance of a carefully checked reference file before to use it.

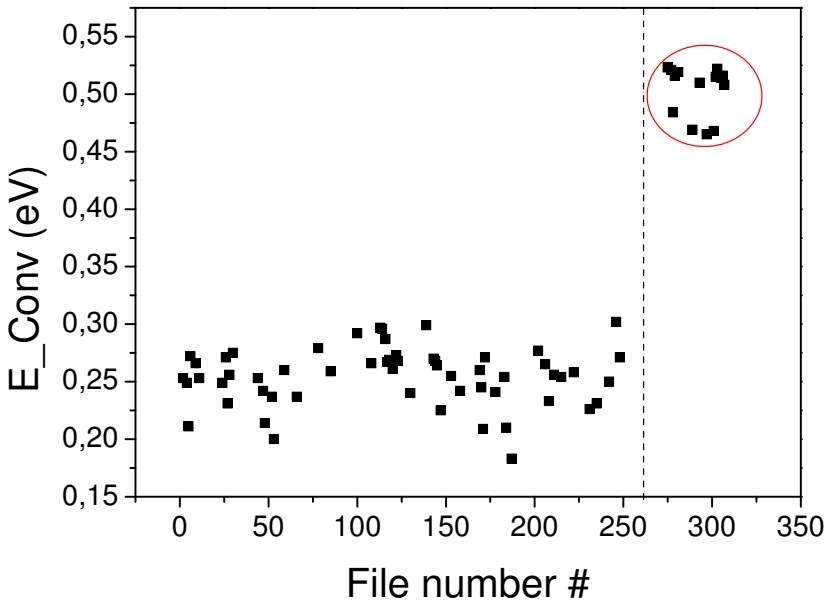

Figure B.5: *Absolute value of the energy of conversion E_{conv} as a function of the file number.*

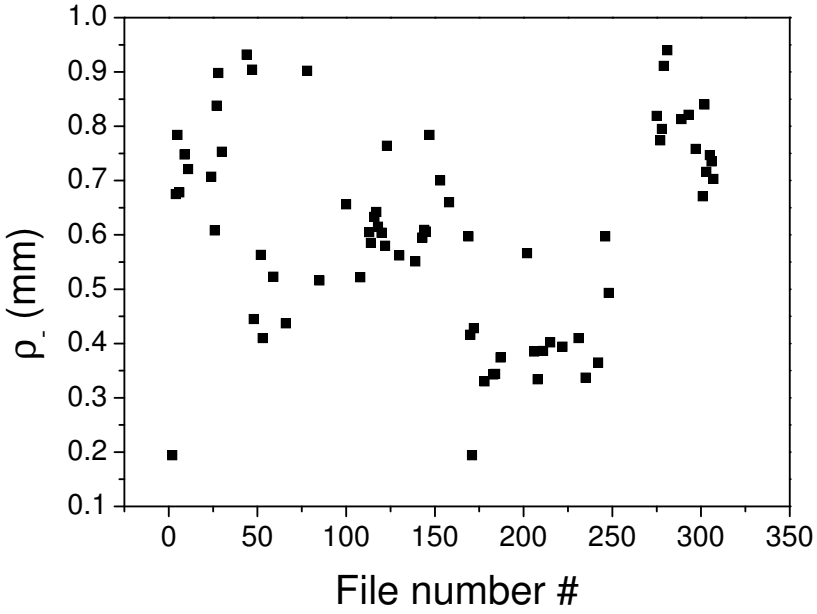

Figure B.6: *Magnetron radius ρ_- as a function of the file number.*

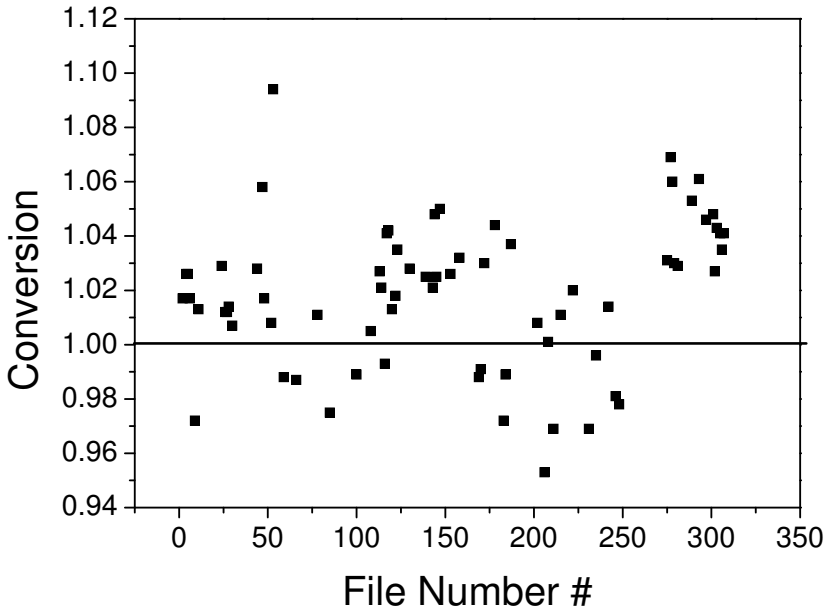

Figure B.7: *Absolute value of the Conversion factor as a function of the file number.*

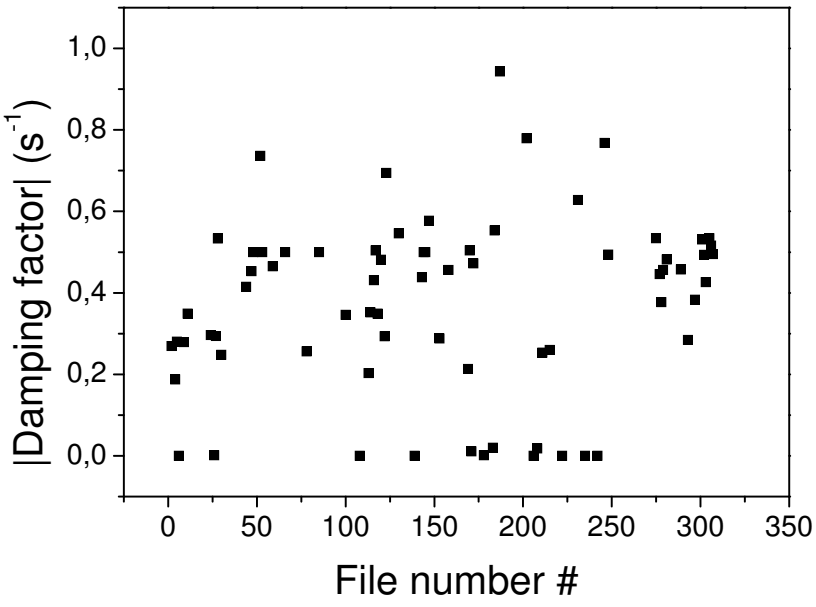

Figure B.8: *Absolute value of the Damping factor as a function of the file number.*

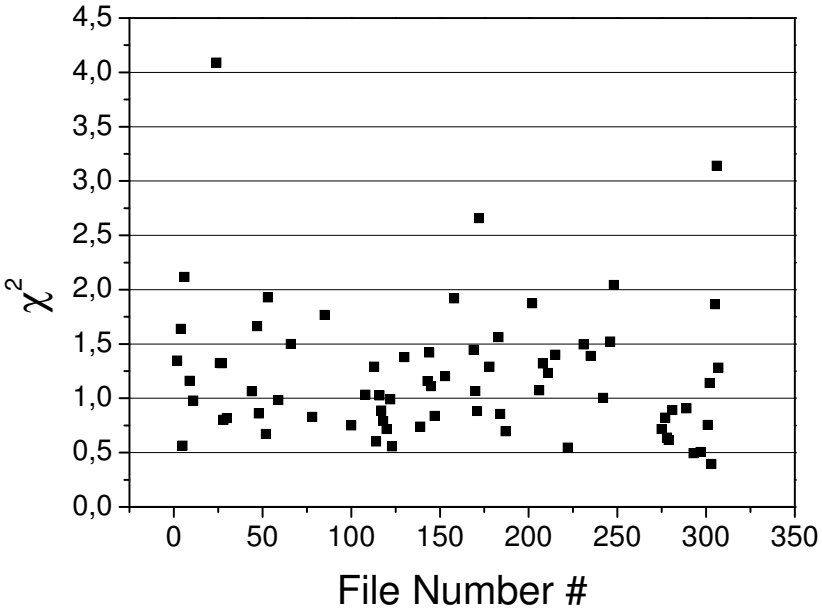

Figure B.9: *Absolute value of the reduced χ^2 as a function of the file number.*

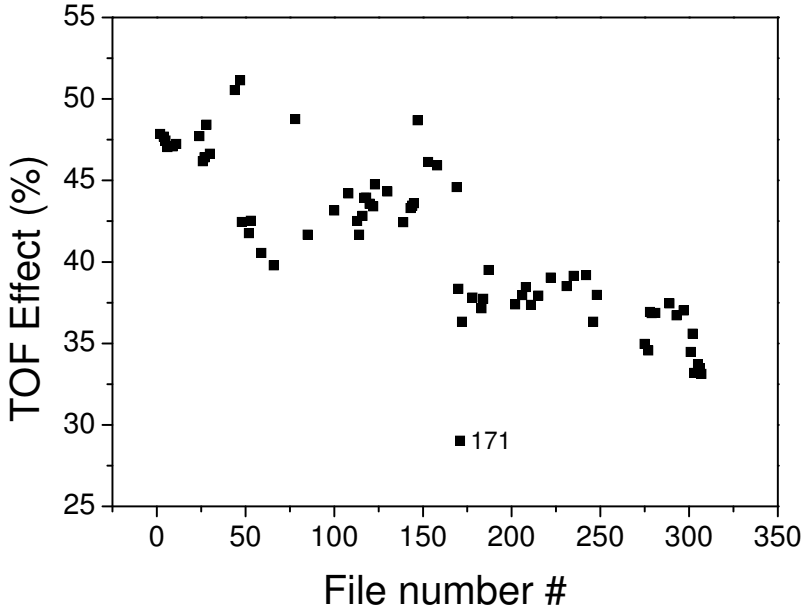

Figure B.10: *TOF effect as a function of the file number.*

Appendix C

On the calculation of the mass value: the excel program

A special analysis program was developed to extract the frequency value from the measurements. The parameters of the fit are discussed in Appendix B.

From this frequency and the frequency of the two references, one can extract the ratio between the mass of interest and the reference mass. This ratio leads to the value of the mass of interest, with its uncertainty.

This determination is performed in an "Excel" program. Hereafter are explained the various formulas used for the calculations.

Since the magnetic field is changing as a function of time, ISOLTRAP is using a reference ion source to calibrate the magnetic field strength, *i.e.* to measure the ratio between the "unknown" mass and a well-known mass.

The reference

Before and after each measurement, such a reference is measured. The magnetic field is estimated to be linear over a measurement time (below 3 hours). So the value of the cyclotron frequency of the mass of reference is calculated from the two measurements performed before and after the measurement of the ion of interest. In the following the measured cyclotron frequency of the reference is indicated by ν^{ref}, and the frequency of the ion of interest by ν_{mes}. Here is the typical schedule:

- t_0 Reference ν_0^{ref} called ν_0 in the following,
- t_1 Ion of interest ν_{mes},
- t_2 Reference ν_2^{ref} called ν_2 in the following.

Since the cyclotron frequency is directly related to the magnetic field (eq.(1.6)) $\nu_0^{ref} \propto B_0$, and $\nu_2^{ref} \propto B_1$. So a linear interpolation $y = a \cdot x + b$ of the variation gives:

$$\nu_0^{ref} = a \cdot t_0 + b \tag{C.1}$$

$$\nu_2^{ref} = a \cdot t_2 + b, \tag{C.2}$$

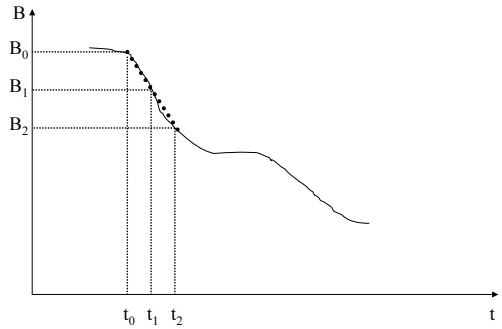

Figure C.1: *Variation of B as a function of time t.*

this leads to $a = \frac{\nu_2 - \nu_0}{t_2 - t_0}$, and $b = \frac{t_2 \cdot \nu_0 - \nu_2 \cdot t_0}{t_2 - t_0}$.

So, the interpolated frequency of the ion of reference during the measurement of the ion of interest is:

$$\nu_{ref} = \frac{\nu_2 - \nu_0}{t_2 - t_0} \cdot t_1 + \frac{t_2 \cdot \nu_0 - \nu_2 \cdot t_0}{t_2 - t_0}. \tag{C.3}$$

The corresponding uncertainty is:

$$\delta\nu_{ref} = \frac{1}{t_2 - t_0}\sqrt{(\delta\nu_0)^2(t_2 - t_1)^2 + (\delta\nu_2)^2(t_1 - t_0)^2}, \tag{C.4}$$

with $\delta\nu_0$ and $\delta\nu_2$ the corresponding uncertainties to ν_0 and ν_2.

The ratio

The ratio between the two frequency at t_1 is r:

$$r = \frac{\nu_{ref}}{\nu_{mes}}, \tag{C.5}$$

and its absolute uncertainty:

$$\delta r = r\sqrt{\left(\frac{\delta\nu_{ref}}{\nu_{ref}}\right)^2 + \left(\frac{\delta\nu_{mes}}{\nu_{mes}}\right)^2}. \tag{C.6}$$

A systematical error from the magnetic field

The magnetic field variation has to be considered. It was measured [82] to be:

$$\frac{\delta B}{\delta t}\frac{1}{B} = -2.30(3) \cdot 10^{-8}/h. \tag{C.7}$$

The corresponding uncertainty which has to be added is: $r \cdot 6.35 \cdot 10^{-11} \cdot (t - 2 - t_0)$, with t_0 and t_2 in minutes.

The corrected absolute uncertainty is δr_{cor}:

$$\delta r_{cor} = \sqrt{(\delta r)^2 + \left(r \cdot 6.35 \cdot 10^{-11} \cdot (t_2 - t_0)\right)^2} \tag{C.8}$$

Mean value of the ratio

The corresponding mean value of r is r_{Mean}:

$$r_{Mean} = \frac{\sum_i \frac{r_i}{(\delta r_{cor} i)^2}}{\sum_i \frac{1}{(\delta r_{cor} i)^2}} \tag{C.9}$$

And its uncertainty:

$$\delta r_{Mean} = \sqrt{\frac{1}{\sum_i \frac{1}{(\delta r_{cor} i)^2}}} \tag{C.10}$$

Systematical errors added to the mean value

- This value has to be corrected because of the mass dependance systematic effect [82]: a mass-dependent frequency ratio shift was observed. A relative standard uncertainty is added to take into account this effect, and the value of r_{Mean} is corrected.
$$\frac{u_m(r)}{r} = 1.6 \cdot 10^{-10} \cdot (m - m_{ref})/u \tag{C.11}$$

- A statistical error has also to be added: $8.0 \cdot 10^{-9}$, due to the limit of precision of ISOLTRAP determined by a systematic study performed on carbon clusters [82].

The final value of r_{Mean} is r_f:

$$r_f = r_{Mean} + r_{Mean} \cdot 1.6 \cdot 10^{-10} \cdot (m - m_{ref})/u. \tag{C.12}$$

And its relative uncertainty is:

$$\delta r_f = \frac{\sqrt{\left(\delta r_{Mean}\right)^2 + \left(r_M ean \cdot 1.6 \cdot 10^{-10} \cdot (m - m_{ref})/u\right)^2 + \left(r_M ean \cdot 8.0 \cdot 10^{-9}\right)^2}}{r} \tag{C.13}$$

Mass value

r is defined (eq.(C.5)) as $r = \frac{\nu_{ref}}{\nu_{mes}}$, with $\nu = \frac{qB}{2\pi m}$, $r = \frac{m_{mes}}{m_{ref}}$.

To obtain atomic masses from m_{mes} and m_{ref}, the mass of one electron m_{e^-} has to be added:

$$M = m_{mes} + m_{e^-} \tag{C.14}$$

$$M_{ref} = m_{ref} + m_{e^-}. \tag{C.15}$$

With M the mass of the ion of interest and M_{ref} the mass of the well-known reference coming from the Atomic Mass Evaluation table (AME).

This leads to

$$M = r_f(M_{ref} - m_{e^-}) + m_{e^-}, \tag{C.16}$$

in atomic units (u). With an uncertainty of:

$$\delta M = \sqrt{\left(M_{ref} - m_{e^-}\right)^2 \left(\delta r_f\right)^2 + \left(r_f\right)^2 \left(\delta M_{ref}\right)^2}. \tag{C.17}$$

Mass excess

The corresponding mass excess D is:

$$D = (M(u) - A) \cdot u \text{ (in keV/c}^2\text{)} \tag{C.18}$$

$$\delta D = u\delta M. \tag{C.19}$$

Bibliography

[1] F.W. ASTON, *Nature* **105**, 617 (1920).

[2] D. LUNNEY, J.M. PEARSON, and C. THIBAULT, *Rev. Mod. Phys.* **75**, 1021 (2003).

[3] G. AUDI, A.H. WAPSTRA, and C. THIBAULT, *Nucl. Phys. A* **729**, 337 (2003).

[4] A. BOHR and B.R. MOTTELSON, *Nuclear structure*, World Scientific (1969).

[5] K. HEYDE, *Basic ideas and concepts in nuclear physics*, Institute of Physics (1994).

[6] *NuPECC Report "NuPECC Long Range Plan 2004: Perspectives for Nuclear Physics Research in Europe in the Coming Decade and Beyond"*, $http://www.nupecc.org/pub/$, 2004.

[7] D. GUILLEMAUD-MUELLER, C. DETRAZ, M. LANGEVIN, F. NAULIN, M. DE SAINT-SIMAON, C. THIBAULT, F. TOUCHARD, and M. EPHERRE, *Nucl. Phys. A* **426**, 37 (1984).

[8] *NUCLEUS*, $http://amdc.in2p3.fr/web/nubdisp_fr.html$, 2005.

[9] J. DUFLO and A.P. ZUKER, *Priv. Comm.* (1996).

[10] E. KUGLER, *Hyp. Int.* **129**, 23 (2000).

[11] D.J. VIEIRA, J.M. WOUTERS, K. VAZIRI, R.H. KRAUS JR., H. WOLLNIK, G.W. BUTLER, F.K. WOHN, and A.H. WAPSTRA, *Phys. Rev. Lett.* **57**, 3253 (1986).

[12] A. GILLIBERT, L. BIANCHI, A. CUNSOLO, B. FERNANDEZ, A. FOTI, J. GASTEBOIS, C. GRÉGOIRE, W. MITTIG, A. PEGHAIRE, Y. SCHUTZ, and C. STEPHAN, *Phys. Lett. B* **176**, 317 (1986).

[13] A. GILLIBERT, W. MITTIG, L. BIANCHI, A. CUNSOLO, B. FERNANDEZ, A. FOTI, J. GASTEBOIS, C. GRÉGOIRE, Y. SCHUTZ, and C. STEPHAN, *Phys. Lett. B* **192**, 39 (1987).

[14] S. ISSMER, M. FRUNEAU, J.A. PINSTON, M. ASGHAR, D. BARNÉOUD, J. GENEVEY, T. KERSCHER, and K.E.G. LÖBNER, *Eur. Phys. J. A* **2**, 173 (1998).

[15] G. AUGER, W. MITTIG, A. LÉPINE-SZILY, L.K. FIFIELD, M. BAJARD, E. BARON, D. BIBET, P. BRICAULT, J.M. CASANDJIAN, M. CHABERT, M. CHARTIER, J. FERMÉ, L. GAUDARD, A. GILLIBERT, M. LEWITOWIC, M.H. MOSCATELLO, N.A. ORR, E. PLAGNOL, C. RICAULT, A.C.C. VILLARI, and YANG YONG FENG, *Inst. and Meth. A* **350**, 235 (1994).

[16] M. CHARTIER, G. AUGER, W. MITTIG, A. LÉPINE-SZILY, L.K. FIFIELD, J.M. CASANDJIAN, M. CHABERT, J. FERMÉ, A. GILLIBERT, M. LEWITOWICZ, M. MAC CORMICK, M.H. MOSCATELLO, O.H. ODLAND, N.A. ORR, G. POLITI, C. SPITAELS, and A.C.C. VILLARI, *Phys. Rev. Lett.* **77**, 2400 (1996).

[17] Y. LITVINOV, *Basic Nuclear Properties of Neutron-Deficient Nuclei Investigated via High Precision Mass Measurements in the Element Range of 36<Z<92* **Ph.D. thesis**, Universität Giessen (2003).

[18] F. ATTALLAH, M. HAUSMANN, Y.A LIVITNOV, T. RADON, J. STADLMANN, K. BECKERT, F. BOSCH, M. FALCH, B. FRANZKE, H. GEISSEL, T. KERSCHER, O. KLEPPER, H-J. KLUGE, C. KOZHUHAROV, K.E.G. LÖBNER, G. MÜNZENBERG, F. NOLDEN, Y.N. NOVIKOV, Z. PATYK, W. QUINT, H. SCHATZ, C. SCHEIDENBERGER, B. SCHLITT, M. STECK, K. SÜMMERER, H. WEICK, and H. WOLLNIK, *Nucl. Phys. A* **701**, 561c (2002).

[19] I. BERGSTRÖM, C. CARLBERG, T. FRITIOFF, G. DOUYSSET, J. SCHÖNFELDER, and R. SCHUCH, *Nucl. Instr. Meth. A* **487**, 618 (2002).

[20] J.C. WANG, G. SAVARD, K.S. SHARMA, J.A. CLARK, Z. ZHOU, A.F. LEVAND, C. BOUDREAU, F. BUCHINGER, J.E. CRAWFORD, J.P. GREENE, S. GULICK, J.K.P. LEE, G.D. SPROUSE, W. TRIMBLE, J. VAZ, and B.Z. ZABRANSKY, *Nucl. Phys. A* **746**, 651c (2004).

[21] J. SZERYPO, A. JOKINEN, V.S. KOLHINEN, A. NIEMINEN, S. RINTA-ANTILA, and J. ÄYSTÖ, *Nucl. Phys. A* **701**, 588c (2002).

[22] J. SCHÖNFELDER, D. ACKERMANN, H. BACKE, G. BOLLEN, J. DILLING, A. DRETZKE, O. ENGELS, J. ESTERMANN, D. HABS, S. HOFMANN, F.P. HESSBERG, H.-J. KLUGE, W. LAUTH, W. LUDOLPHS, M. MAIER, G. MARX, R.B. MOORE, W. QUINT, D. RODRIGUEZ, M. SEWTZ, G. SIKLER, C. TOADER, and C. WEBER, *Nucl. Phys. A* **701**, 579c (2002).

[23] G. BOLLEN, S. SCHWARZ, D. DAVIES, P. LOFY, D.J. MORRISSEY, R. RINGLE, P. SCHURY, T. SUN, and L. WEISSMAN, *Nucl. Phys. A* **746**, 597c (2004).

[24] A. LINDROTH, M. BECK, B. DELAURÉ, V.YU KOZLOV, N. SEVERIJNS, F. AMES, D. BECK, V.V. GOLOVKO, I. KRAEV, T. PHALET, and S. VERSYCK, *Nucl. Phys. A* **721**, 1103c (2003).

[25] J. SZERYPO, D. HABS, S. HEINZ, J. NEUMAYR, P. THIROLF, A. WILFART, and F. VOIT, *Nucl. Instr. Meth. B* **204**, 512 (2003).

[26] J. DILLING, P. BRICAULT, M. SMITH, H.-J. KLUGE, and THE TITAN COLLABORATION, *Nucl. Instr. Meth. B* **204**, 492 (2003).

[27] C. RAUTH, C. GEPPERT, R. HORN, J. LASSEN, P. BRICAULT, and K. WENDT, *Nucl. Instr. Meth. B* **215**, 268 (2004).

[28] C. BACHELET, *Mesure de masse de noyaux à halo et refroidissement de faisceaux avec l'expérience MISTRAL* **Ph.D. thesis**, Université Paris XI (2004).

[29] D.A. CHURCH, *Physics Reports* **228**, 253 (1993).

[30] J.D. JACKSON, *Classical Electrodynamics*, Wiley, New York (1975).

[31] P.K. GHOSH, *Ion traps*, Oxford Science Publication (1995).

[32] P.H. DAWSON, *Quadrupole mass spectrometry and its application*, Elsevier Scientific Publishing Company (1976).

[33] S. HENRY, *Piégeage et refroidissement d'ions exotiques pour la mesure de masse* **Ph.D. thesis**, Université Louis Pasteur (2001).

[34] S. SCHWARZ, *Manipulation radioaktiver Ionenstrahlen mit Hilfe einer Paulfalle und direkte Massenmessungen an neutronenarmen Quecksilberisotopen mit dem ISOLTRAP-Experiment* **Ph.D. thesis**, Universität Mainz (1998).

[35] L.S. BROWN and G. GABRIELSE, *Rev. Mod. Phys.* **58**, 233 (1986).

[36] G. BOLLEN, R.B. MOORE, G. SAVARD, and H. STOLZENBERG, *J. Appl. Phys* **68**, 4355 (1990).

[37] M. KRETZCHMAR, *Phys. Scripta* **46**, 545 and 555 (1992).

[38] M. KÖNIG, G. BOLLEN, H.-J. KLUGE, T. OTTO, and J. SZERYPO, *Int. J. Mass Spectrom. Ion Proc.* **142**, 95 (1995).

[39] C. YAZIDJIAN, Masters thesis, Université de Caen (2003).

[40] B. DIU, C. GUTHMANN, D. LEDERER, and B. ROULET, *Physique Statistique*, Hermann, Editeurs des sciences et des arts (1989).

[41] H. POTH, *Phys. Rep.* **196**, 135 (1990).

[42] S. VAN DER MEER, *Rev. Mod. Phys.* **57**, 689 (1985).

[43] S. CHU, *Rev. Mod. Phys.* **70**, 687 (1998).

[44] C.N. COHEN-TANNOUDJI, *Rev. Mod. Phys.* **70**, 707 (1998).

[45] W.D. PHILLIPS, *Rev. Mod. Phys.* **70**, 721 (1998).

[46] M.D. LUNNEY and R.B MOORE, *Int. J. Mass Spectrom.* **190/191**, 153 (1999).

[47] J. ANDRÉ, *J. Physique* **37**, 719 (1976).

[48] J. ANDRÉ and F. VEDEL, *J. Physique* **38**, 1381 (1977).

[49] A. ALILLI, J. ANDRÉ, and F. VEDEL, *Physica Scripta* **T22**, 325 (1988).

[50] G. SAVARD, S. BECKER, G. BOLLEN, H.-J. KLUGE, R.B. MOORE, T. OTTO, L. SCHWEIKHARD, H. STOLZENBERG, and U. WIESS, *Phys. Lett. A* **158**, 247 (1991).

[51] M. DE SAINT-SIMON, C. THIBAULT, G. AUDI, A. COC, H. DOUBRE, M. JACOTIN, J.-F. KEPINSKI, R. LE GAC, G. LE SCORNET, D. LUNNEY, and F. TOUCHARD, *Phys. Scr. T* **59**, 406 (1995).

[52] D. LUNNEY, G. AUDI, H. DOUBRE, S. HENRY, C. MONSANGLANT, M. DE SAINT SIMON, C. THIBAULT, and C. TOADER, *Phys. Rev. C* **64**, 054311 (2001).

[53] C. MONSANGLANT, *Mesures de masses de haute précision avec MISTRAL au voisinage de* ^{32}Mg **Ph.D. thesis**, Université Paris XI (2000).

[54] N. VIEIRA, *Mesure de la masse atomique du noyau N=Z* ^{74}Rb *avec le spectromètre MISTRAL* **Ph.D. thesis**, Université Paris VI (2002).

[55] L.G. SMITH, in *Proc. Int. Conf. on Nuclidic Masses*, p. 418, Univ of Toronto Press, Canada, 1960.

[56] C. BACHELET, G. AUDI, C. GAULARD, C. GUÉNAUT, F. HERFURTH, D. LUNNEY, M. DE SAINT SIMON, C. THIBAULT, and THE ISOLDE COLLABORATION, *Eur. Phys. J. A Direct* **24** (2005).

[57] F. HERFURTH, J. DILLING, A. KELLERBAUER, G. BOLLEN, S. HENRY, H.-J. KLUGE, E. LAMOUR, D. LUNNEY, R.B. MOORE, C. SCHEIDENBERGER, S. SCHWARZ, G. SIKLER, and J. SZERYPO, *Nucl. Instr. Meth. A* **469**, 254 (2001).

[58] G. BOLLEN, S. BECKER, H.-J. KLUGE, M. KÖNIG, R.B. MOORE, T. OTTO, H. RAIMBAULT-HARTMANN, G. SAVARD, L. SCHWEIKHARD, H. STOLZENBERG, and THE ISOLDE COLLABORATION, *Nucl. Instr. Meth A* **368**, 675 (1996).

[59] H. RAIMBAULT-HARTMANN, D. BECK, G. BOLLEN, M. KÖNIG, H.-J. KLUGE, E. SCHARK, J. STEIN, S.SCHWARZ, and J.SZERYPO, *Nucl. Phys. B* **126**, 378 (1997).

[60] F. HERFURTH, *A new ion beam cooler and buncher for ISOLTRAP and mass measurements of radioactive argon isotopes* **Ph.D. thesis**, University of Heidelberg, Germany (2001).

[61] G. GRÄFF, H. KALINOWSKY, and J. TRAUT, *Z. Phys. A* **297**, 35 (1980).

[62] B. BREHM, J. GROSSER, T. RUSCHEINSKI, and M. ZIMMER, *Meas. Sci. Technol.* **6**, 953 (1995).

[63] J. OBERHEIDE, P. WILLIAMS, and M. ZIMMER, *Meas. Sci. Technol.* **8**, 351 (1997).

[64] C. YAZIDJIAN, **Ph.D. thesis**, Université de Caen (to be published in 2006).

[65] A. HERLERT, D. BECK, K. BLAUM, F. CARREL, P. DELAHAYE, S. GEORGE, C. GUÉNAUT, F. HERFURTH, A. KELLERBAUER, H.-J. KLUGE, D. LUNNEY, M. MUKHERJEE, L. SCHWEIKHARD, and C. YAZIDJIAN, *New. J. of Phys.* **7**, 44 (2005).

[66] A. KELLERBAUER, G. AUDI, D. BECK, K. BLAUM, G. BOLLEN, B.A. BROWN, P. DELAHAYE, C. GUÉNAUT, F. HERFURTH, D. LUNNEY, H.-J. KLUGE, S. SCHWARZ, L. SCHWEIKHARD, and C. YAZIDJIAN, *Nucl. Phys. A* **746**, 635 (2004).

[67] K. BLAUM, D. BECK, G. BOLLEN, F. HERFURTH, A. KELLERBAUER, H.-J. KLUGE, R.B. MOORE, E. SAUVAN, C. SCHEIDENBERGER, S. SCHWARZ, and L. SCHWEIKHARD, *Nucl. Inst. and Meth. B* **204**, 478 (2003).

[68] H. WOLLNIK, *Optics of charged particles*, Academic Press Inc. (London) (1987).

[69] J. LIOUVILLE, *Journ. de Math.* **3**, 349 (1838).

[70] A. COC, R. LE GAC, M. DE SAINT SIMON, C. THIBAULT, and F. TOUCHARD, *Nucl. Inst. and Meth. A* **271**, 512 (1988).

[71] F. WENANDER, J. LETTRY, and M. LINDROOS, *Nucl. Inst. Meth. B* **204**, 261 (2003).

[72] C. KITEGI, Masters thesis, Université Paris XI (2002).

[73] N. CHAUVIN, F. DAYRAS, D. LE DU, and R. MEUNIER, *Nucl. Inst. and Meth. A* **521**, 149 (2004).

[74] C. BACHELET, Masters Thesis, Université Paris XI (2000).

[75] E. LECCIA, Undergraduate project report, Université Paris XI (2004).

[76] M. SEWTZ, C. BACHELET, N. CHAUVIN, C. GUÉNAUT, J.F. KEPINSKI, E. LECCIA, D. LE DU, and D. LUNNEY, *Nucl. Instr. Meth. B* **240**, 55 (2005).

[77] G. HUCHET, Undergraduate project report, Université Paris XI (2002).

[78] B. AYACHE, Undergraduate project report, ESIEE Amiens (2005).

[79] H. RAIMBAULT-HARTMANN, *Präzisionsmassenbestimmung neutronenreicher Rubidium- und Strontiumisotope und Entwicklung und Test eines neuen Konzeptes zur Ionenakkumulation und -kühlung für ISOLTRAP* **Ph.D. thesis**, Universität Mainz (1994).

[80] G. BOLLEN, H. HARTMANN, H.-J. KLUGE, M. KÖNIG, T. OTTO, G. SAVARD, and H. STOLZENBERG, *Phys. Scripta* **46**, 581 (1992).

[81] G. BOLLEN, *Priv. Comm.* (1993).

[82] A. KELLERBAUER, K. BLAUM, G. BOLLEN, F. HERFURTH, H.-J. KLUGE, M. KUCKEIN, E. SAUVAN, C. SCHEIDENBERGER, and L. SCHWEIKHARD, *Eur. Phys. J. D* **22**, 53 (2003).

[83] C. GERZ, D. WILDSORF, and G. WERTH, *Nucl. Instr. Meth. B* **47**, 453 (1990).

[84] U. KÖSTER, *Ausbeuten und Spektroskopie radioaktiver Isotope bei LOHENGRIN und ISOLDE* **Ph.D. thesis**, University of Munich, Germany (2001).

[85] A.H. WAPSTRA, G. AUDI, and C. THIBAULT, *Nucl. Phys.* **A 729**, 129 (2003).

[86] G. AUDI and A.H. WAPSTRA, *Nucl. Phys. A* **595**, 409 (1995).

[87] C. GUÉNAUT, G. AUDI, D. BECK, K. BLAUM, G. BOLLEN, P. DELAHAYE, F. HERFURTH, A. KELLERBAUER, H.-J. KLUGE, D. LUNNEY, S. SCHWARZ, L. SCHWEIKHARD, , and C. YAZIDJIAN, *Eur. Phys. J. A Direct* **25**, s1.35 (2005).

[88] W. KANE, *Private Communication to Audi-Wapstra* (1982).

[89] J.L. BENSON and W.H. JOHNSON,JR., *Phys. Rev.* **141**, 1112 (1966).

[90] R.D. GRIFFIOEN and R.K. SHELINE, *Phys. Rev. C* **10**, 624 (1974).

[91] P. DEBENHAM, W.R. FALK, and M. CANTY, *Canadian Journal of Physics* **52**, 1416 (1974).

[92] H.B. MATHUR and E.K. HYDE, *Physical Review* **95**, 708 (1954).

[93] A. SPALEK, I. REZANKA, J. FRANA, and A. MASTALKA, *Z. Physik* **204**, 129 (1967).

[94] L. WESTGAARD, K. ALEKLETT, G. NYMAN, and E. ROECKL, *Z. Phys.* **A 275**, 127 (1975).

[95] F. AMES, G. AUDI, D. BECK, G. BOLLEN, M. DE SAINT SIMON, R. JERTZ, H.-J. KLUGE, A. KOHL, M. KÖNIG, D. LUNNEY, I. MARTEL, R.B. MOORE, T. OTTO, Z. PATYK, H.RAIMBAULT-HARTMANN, G. ROULEAU, G. SAVARD, E. SCHARK, S. SCHWARZ, L. SCHWEIKHARD, H. STOLZENBERG, J. SZERYPO, and ISOLDE, *Nucl. Phys. A* **651**, 3 (1999).

[96] G. AUDI, *Priv. Comm.* (2002).

[97] H. STOLENBERG, S. BECKER, G. BOLLEN, F. KERN, H.-J. KLUGE, T. OTTO, G. SAVARD, L. SCHWEIKHARD, G. AUDI, and R.B. MOORE, *Phys. Rev. Lett.* **65**, 3104 (1990).

[98] R. IAFIGLIOLA, M. CHATTERJEE, H. DAUTET, and J.K.P. LEE, *Canadian Journal of Chemistry* **61**, 694 (1983).

[99] M. GROSS, P. JÜRGENS, S. KLUGE, M. MEHRTENS, S. MÜLLER, F. MÜNNICH, and J. WULFF, Proceedings of the 9th International Conference Atomic Massses and Fundamental Constants, and 6th International Conference Nuclei far from Stability, in *AMCO-9 and Nufast-6*, p. 77, IOP Publishing, 1992.

[100] M. PRZEWLOKA, A. PRZEWLOKA, P. WÄCHTER, and H. WOLLNIK, *Z. Physik A* **342**, 23 (1992).

[101] F.K. WOHN and W.L. TALBERT,JR, *Phys. Rev. D* **18**, 2328 (1978).

[102] K.-L. KRATZ, A.SCHRÖDER, H. OHM, H. GABELMANN, W. ZIEGERT, B. STEINMÜLLER, and B. PFEIFFER, in *Proc. 7th Int. Conf. Atomic Masses and Fundamental Constants AMCO-7*, p. 127, 1984.

[103] H. RAIMBAULT-HARTMANN, G. AUDI, D. BECK, G. BOLLEN, M. DE SAINT-SIMON, H.-J. KLUGE, M. KÖNIG, R.B. MOORE, S.SCHWARZ, G.SAVARD, J.SZERYPO, and ISOLDE, *Nucl. Phys. A* **706**, 3 (2002).

[104] J.F. MATEJA and C.P. BROWNE, *Phys. Rev. C* **15**, 1708 (1977).

[105] J.F. MATEJA, G.F. NEAL, J.D. GROSS, P.R. CHAGNON, and C.P. BROWNE, *Phys. Rev. C* **13**, 118 (1976).

[106] K.A. ANIOL, D.W. GEBBIE, C.L. HOLLAS, and J. NURZINSKI, *Nucl. Phys. A* **303**, 154 (1978).

[107] M.A. ISLAM, T.J. KENNETT, S.A. KERR, and W.V. PRESTWICH, *Canadian J. of Phys.* **58**, 168 (1980).

[108] R.B. FIRESTONE, R.M. LINDSTROM, G.L. MOLNAR, S.M. MUGHABGHAB, A.V.R REDDY, Z. REVAY, V.H. TAN, C.M. ZHOU, and R. PAVIOTTI-CORCUERA, *International Atomic Energy Agency, Technical report*, to be published (2003).

[109] *ENSDF*, $http : //amdc.in2p3.fr/ens/filel.html$, 2003.

[110] R. CHAPMAN, S. HINDS, and A.E. MACGREGOR, *Nucl. Phys. A* **119**, 305 (1968).

[111] R.F. CASTEN, E.R. FLYNN, O. HANSEN, and T.J. MULLIGAN, *Phys. Rev. C* **4**, 130 (1971).

[112] X.L. TU, X.G. ZHOU, D.J. VIEIRA, J.M. WOUTERS, Z.Y. ZHOU, H.L. SEIFERT, and V.G. LIND, *Z. Phys. A* **337**, 361 (1990).

[113] H.L. SEIFERT, J.M. WOUTERS, D.J. VIEIRA, H. WOLLNIK, X.G. ZHOU, X.L. TU, Z.Y. ZHOU, and G.W. BUTLER, *Z. Phys. A* **349**, 25 (1994).

[114] C.N. DAVIDS, D.F. GEESAMAN, S.L. TABOR, M.J. MURPHY, E.B. NORMAN, and R.C. PARDO, *Phys. Rev. C* **17**, 1815 (1978).

[115] J. LIBERT and M. GIROD, *Priv. Comm.* (2005).

[116] J.I. PRISCIANDARO, P.F. MANTICA, B.A. BROWN, D.W. ANTHONY, M.W. COOPER, A. GARCIA, D.E. GROH, A. KOMIVES, W. KUMARASIRI, P.A. LOFY, A.M. OROS-PEUSQUENS, S.L. TABOR, and M. WIEDEKING, *Phys. Lett. B* **510**, 17 (2001).

[117] O. SORLIN, C. DONZAUD, F. NOWACKI, J.C. ANGÉLIQUE, F. AZAIEZ, C. BOURGEOIS, V. CHISTE, Z. DLOUHY, S. GRÉVY, D. GUILLEMAUD-MUELLER, F. IBRAHIM, K.-L. KRATZ, M. LEWITOWICZ, S.M. LUKYANOV, J. MRASEK, YU.-E. PENIONZHKEVICH, F. DE OLIVEIRA SANTOS, B. PFEIFFER, F. POUGHEON, A. POVES, M.G. SAINT-LAURENT, and M. STANOIU, *Eur. Phys. J. A* **16**, 55 (2003).

[118] S. RAMAN, C.W. NESTOR, and P. TIKKANEN, *At. Data Nucl. Data Tables* **78**, 1 (2001).

[119] P. MÖLLER, J.R. NIX, W.D. MYERS, and W.J. SWIATECKI, *At. Data Nucl. Data Tables* **59**, 185 (1995).

[120] M. BERNAS, P. DESSAGNE, M. LANGEVIN, J. PAYET, F. POUGHEON, and P. ROUSSEL, *Phys. Lett. B* **113**, 279 (1982).

[121] L.P. EKSTROM and J. LYTTKENS-LINDEN, *Nucl. Data Sheets* **67**, 579 (1992).

[122] R. BRODA, B. FORNAL, W. KRÒLAS, T. PAWLAT, D. BAZZACCO, S. LUNARDI, C. ROSSI-ALVAREZ, R. MENEGAZZO, G. DE ANGELIS, P. BEDNARCZYK, J. RICO, D. DE ACUÑA, P.J. DALY, R.H. MAYER, M. SFERRAZZA, H. GRAWE, K.H. MAIER, and R. SCHUBART, *Phys. Rev. Lett.* **74**, 868 (1995).

[123] R. GRZYWACZ, R. BÉRAUD, C. BORCEA, A. EMSALLEM, M. GLOGOWSKI, H. GRAWE, D. GUILLEMAUD-MUELLER, M. HJORTH-JENSEN, M. HOURY, M. LEWITOWICZ, A.C. MUELLER, A. NOWAK, A. PLOCHOCKI, M. PFÜTZNER, K. RYKACZEWSKI, M.G. SAINT-LAURENT, J.E. SAUVESTRE, M. SCHAEFER, O. SORLIN, J. SZERYPO, W. TRINDER, S. VITERITTI, and J. WINFIELD, *Phys. Rev. Lett.* **81**, 766 (1998).

[124] M. HANNAWALD, T. KAUTZSCH, A. WÖHR, W.B. WALTERS, K.-L. KRATZ, V.N. FEDOSEYEV, V.I. MISHIN, W. BÖHMER, B. PFEIFFER, V. SEBASTIAN, Y. JADING, U. KÖSTER, J. LETTRY, H.L. RAVN, and THE ISOLDE COLLABORATION, *Phys. Rev. Lett.* **82**, 1391 (1999).

[125] W.F. MUELLER, B. BRUYNEEL, S. FRANCHOO, H. GRAWE, M. HUYSE, U. KÖSTER, K.-L. KRATZ, K. KRUGLOV, Y. KUDRYAVTSEV, B. PFEIFFER, R. RAABE, I. REUSEN, P. THIROLF, P. VAN DUPPEN, J. VAN ROOSBROECK, L. VERMEEREN, W.B. WALTERS, and L. WEISSMAN, *Phys. Rev. Lett.* **83**, 3613 (1999).

[126] O. SORLIN, S. LEENHARDT, C. DONZAUD, J. DUPRAT, F. AZAIEZ, F. NOWACKI, H. GRAWE, Z. DOMBRÁDI, F. AMORINI, A. ASTIER, D. BAIBORODIN, M. BELLEGUIC, C. BORCEA, C. BOURGEOIS, D. M. CULLEN, Z. DLOUHY, E. DRAGULESCU, M. GÓRSKA, S. GRÉVY, D. GUILLEMAUD-MUELLER, G. HAGEMANN, B. HERSKIND, J. KIENER, R. LEMMON, M. LEWITOWICZ, S.M. LUKYANOV, P. MAYET, F. DE OLIVEIRA SANTOS, D. PANTALICA, YU.-E. PENIONZHKEVICH, F. POUGHEON, A. POVES, N. REDON, M.G. SAINT-LAURENT, J.A. SCARPACI, G. SLETTEN, M. STANOIU, O. TARASOV, and C. THEISEN, *Phys. Rev. Lett.* **88**, 092501 (2002).

[127] K. LANGANKE, *Phys. Rev. C* **67**, 044314 (2003).

[128] P. VAN ISACKER, *C.R. Physique* **4**, 529 (2003).

[129] PH. DESSAGNE, M. BERNAS, M. LANGEVIN, G.C. MORRISON, J. PAYET, F. POUGHEON, and P. ROUSSEL, *Nucl. Phys. A* **426**, 399 (1984).

[130] J. VAN ROOSBROECK, C. GUÉNAUT, G. AUDI, D. BECK, K. BLAUM, G. BOLLEN, J. CEDERKALL, P. DELAHAYE, H. DE WITTE, D. FEDOROV, V.N. FEDOSEYEV, S. FRANCHOO, H. FYNBO, M. GORSKA, F. HERFURTH, K. HEYDE, M. HUYSE, A. KELLERBAUER, H.-J. KLUGE, U. KÖSTER, K. KRUGLOV, D. LUNNEY, A. DE. MAESSCHALCK, V.I. MISHIN, W.F. MÜLLER, S. NAGY, S. SCHWARZ, L. SCHWEIKHARD, N.A. SMIRNOVA, K. VAN DE VEL, P. VAN DUPPEN, A. VAN DYCK, W.B. WALTERS, L. WEISSMAN, C. YAZIDJIAN, and THE ISOLDE COLLABORATION, *Phys. Rev. Lett.* **92**, 112501 (2004).

[131] K. BLAUM, D. BECK, G. BOLLEN, P. DELAHAYE, C. GUÉNAUT, F. HERFURTH, A. KELLERBAUER, H.-J. KLUGE, D. LUNNEY, S. SCHWARZ, L. SCHWEIKHARD, and C. YAZIDJIAN, *Europhys. Lett.* **67**, 586 (2004).

[132] E. CAURIER, G. MARTÍNEZ-PINEDO, F. NOWACKI, A. POVES, and A.P. ZUKER, *Rev. Mod. Phys.* **77**, 427 (2005).

[133] E. CAURIER, G. MARTÍNEZ-PINEDO, F. NOWACKI, A. POVES, J. RETAMOSA, and A.P. ZUKER, *Phys. Rev. C* **459**, 2033 (1999).

[134] C.F. VON WEIZSÄCKER, *Z. Phys.* **96**, 431 (1935).

[135] H.A. BETHE and R.F. BACHER, *Rev. Mod. Phys.* **8**, 82 (1936).

[136] J.M. PEARSON, *Hyp. Int.* **132**, 59 (2001).

[137] J.M. FLETCHER, *Masters thesis*, University of Surrey (2003).

[138] W.D. MYERS and W.J. SWIATECKI, *Nucl. Phys.* **81**, 1 (1966).

[139] J. DUFLO and A.P. ZUKER, *Phys. Rev. C* **59**, R2347 (1999).

[140] M. BEINER, H. FLOCARD, NGUYEN VAN GIAI, and P. QUENTIN, *Nucl. Phys. A* **238**, 29 (1975).

[141] J. DECHARGE and D. GOGNY, *Phys. Rev. C* **21**, 1568 (1980).

[142] P. BONCHE, J. DOBACZEWSKI, H. FLOCARD, P.-H. HEENEN, and J. MEYER, *Nucl. Phys. A* **510**, 466 (1990).

[143] P.-H. HEENEN, P. BONCHE, and H. FLOCARD, *Nucl. Phys. A* **588**, 490 (1995).

[144] H. FLOCARD, S.E. KOONIN, and M.S. WEISS, *Phys. Rev. C* **17**, 1682 (1978).

[145] P. BONCHE, H. FLOCARD, and P.-H. HEENEN, *Comp. Phys. Com.*, In press (2005).

[146] M. BENDER, G.F. BERTSCH, and P.-H. HEENEN, *Phys. Rev. Lett.* **94**, 102503 (2005).

[147] F. TONDEUR, S. GORIELY, J.M. PEARSON, and M. ONSI, *Phys. Rev. C* **62**, 024308 (2000).

[148] S. GORIELY, F. TONDEUR, and J.M. PEARSON, *At. Data Nucl. Data Tables* **77**, 311 (2001).

[149] M. SAMYN, S. GORIELY, P.-H. HEENEN, J.M. PEARSON, and F. TONDEUR, *Nucl. Phys. A* **700**, 142 (2001).

[150] S. GORIELY, M. SAMYN, P.-H. HEENEN, J.M. PEARSON, and F. TONDEUR, *Phys. Rev. C* **66**, 024326 (2002).

[151] M. SAMYN, S. GORIELY, and J.M. PEARSON, *Nucl. Phys. A* **725**, 69 (2003).

[152] S. GORIELY, M. SAMYN, M. BENDER, and J.M. PEARSON, *Phys. Rev. C* **68**, 054325 (2003).

[153] M. SAMYN, S. GORIELY, M. BENDER, and J.M. PEARSON, *Phys. Rev. C* **70**, 044309 (2004).

[154] S. GORIELY, M. SAMYN, J.M. PEARSON, and M. ONSI, *Nucl. Phys. A* **750**, 425 (2005).

[155] M. GIROD, J.-P. DELAROCHE, J. LIBERT, and I. DELONCLE, *Phys. Rev. C* **45**, R1420 (1992).

[156] J.P DELAROCHE, M. GIROD, G. BASTIN, I. DELONCLE, F. HANNACHI, J. LIBERT, M.G. PORQUET, C. BOURGEOIS, D. HOJMAN, P. KILCHER, A. KORICHI, F. LE BLANC, N. PERRIN, B. ROUSSIÈRE, J. SAUVAGE, and H. SERGOLLE, *Phys. Rev. C* **50**, 2332 (1994).

[157] J. LIBERT, M. GIROD, and J.-P. DELAROCHE, *Phys. Rev. C* **60**, 054301 (1999).

[158] J. BARDEEN, L.N. COOPER, and J.R. SCHRIEFFER, *Phys. Rev.* **108**, 1175 (1957).

[159] A. OZAWA, T. KOBAYASHI, T. SUZUKI, K. YOSHIDA, and I. TANIHATA, *Phys. Rev. Lett.* **84**, 5493 (2000).

[160] R. KANUNGO, I. TANIHATA, and A. OZAWA, *Phys. Lett. B* **528**, 58 (2002).

Résumé

Les nombres magiques ou fermetures de couche sont une des caractéristiques importantes de la structure nucléaire, mais qui sont modifiés loin de la vallée de stabilité. La détermination de l'énergie de liaison, via des mesures de masse sur les noyaux exotiques, représente un des plus grands challenge dans l'étude de la structure nucléaire à cause de la précision importante qui est nécessaire, et du faible taux de production, ainsi que les courtes durées de vie. Afin de résoudre le problème, deux spectromètres de masse ISOLTRAP et MISTRAL peuvent être utilisés, tous les deux situés à ISOLDE/CERN (Genève). MISTRAL est un spectromètre de masse à transmission pour les noyaux de courtes durées de vie, et ISOLTRAP est un spectromètre de masse basé sur l'utilisation de pièges de Penning, qui effectue des mesures de masses de haute précision. Cette thèse décrit les techniques pour repousser les limites de ces deux instruments complémentaires: un système de refroidissement de faisceau pour améliorer la sensibilité de MISTRAL et une procédure d'optimisation pour améliorer la définition des champs de piégeage d'ISOLTRAP. Des mesures très précises ont été effectuées avec ISOLTRAP afin d'augmenter le nombre de noyaux très bien connus dans la table de masse, et afin d'examiner le cas de deux nouveaux nombres magiques $N = 32$ et $N = 40$. Les résultats montrent un surplus d'énergie de liaison pour le $^{56}Cr_{32}$ dû à la présence d'une probable déformation. Un faible effet apparait pour le $^{68}Ni_{40}$, peut-être dû à une compétition avec la demi-couche à $N = 39$, la présence d'une fermeture de couche à $N = 40$ est exclue par nos résultats.

Mots-Clés : Nombres magiques - Structure nucléaire - Pièges à ions - Mesure de masse - Optimisation des champs electromagnétiques

Abstract

Magic numbers or shell closures, are an important feature of nuclear structure, but now found to be modified far from stability. Determination of the nuclear binding energy via mass measurements of exotic nuclides represents one of the greatest challenges in the study of nuclear structure due to the high precision required and the low production rates and short half-lives. To solve the problem, the complementary spectrometers MISTRAL and ISOLTRAP may be used, both located at ISOLDE/CERN (Geneva). MISTRAL is a transmission mass spectrometer for very short-lived nuclides, and ISOLTRAP a Penning-trap mass spectrometer providing exceptional precision. This thesis describes improvements in the limitations of these complementary instruments: a beam cooler to increase the sensitivity of MISTRAL and an optimization procedure to improve the definition of the ISOLTRAP trapping fields. High-precision mass measurements were performed at ISOLTRAP to extend the backbone of well-known nuclides in the mass table, and to finely examine the case for new magic numbers $N = 32$ and 40. The results illustrate a subtle effect of extra binding energy for $^{56}Cr_{32}$ in the presence of a probable deformation. A small effect is visible for $^{68}Ni_{40}$, perhaps in conjunction with a competitive mid-shell effect at $N = 39$, the case for a shell or even sub-shell closure at $N = 40$ is excluded by these results.

Keywords : Magic numbers - Nuclear structure - Ion traps - Mass measurement - Field optimization